Master Thesis

Rare, weak J/ψ decays in BESIII
$J/\psi \to D^0\phi$ and $J/\psi \to D^0\omega$

Remco de Boer
MSc student Experimental Physics
Faculty of Science
Utrecht University

October 2019

First examiner: Prof. Dr. R.J.M. Snellings
Second examiner: Dr. A. Grelli
Institute of Subatomic Physics
Utrecht University, The Netherlands

Daily supervisor: Prof. Dr. X.Y. Shen
BESIII Collaboration
Institute of High Energy Physics
Chinese Academy of Science

Abstract

The BESIII collaboration has produced the largest, clean sample of J/ψ mesons through e^+e^- collisions. These collisions are used to performed detailed studies of decays involving charmed mesons. In this study, a new upper limit has been set on the rare, weak decays $J/\psi \to D^0\phi$ and $J/\psi \to D^0\omega$ using hadronic decay modes $D^0 \to K^+\pi^-$, $\phi \to K^+K^-$, and $\omega \to \pi^+\pi^-\pi^0, \pi^0 \to \gamma\gamma$ using a sample of 10 billion J/ψ events. The upper limits of the branching ratios determined by this study are $\mathcal{B}\left(J/\psi \to D^0\phi\right) < 3.4 \times 10^{-7}$ and $\mathcal{B}\left(J/\psi \to D^0\omega\right) < 2.1 \times 10^{-6}$ with systematic uncertainties of at least 5.8% and 6.1% respectively. These are the first upper limits set on these decay channels, but these results can be quoted only after more systematic uncertainties have been evaluated.

Contents

List of Figures

List of Tables

Chapter 1

Introduction

The field of High Energy Physics (HEP) has seen major upheavals over the past decade. With the discovery of the Higgs boson in 2012 at the Large Hadron Collider (LHC) [1, 2], the Standard Model (SM) of particle physics has been firmly established. The discovery served as a pivotal moment that caused a revision of the field's research programme. The anchors and boundaries of the theory had become clear and there were no other concretely defined particles on the search list.

Today's HEP research can be broadly categorised in two overlapping programmes. First, despite the predictive accuracy of the SM, there are reasons to believe that this model is not the ultimate theory. There are many fundamental phenomena that the SM doesn't address: it doesn't explain the parameter values on which it depends, it doesn't include a description of gravity, it cannot account for the large matter-antimatter asymmetry in the universe, and it doesn't explain dark matter. This has led to a large number of Beyond the Standard Model (BSM) theories the predictions of which are pursued through direct searches in high-energy collider experiments.

Second, the elegance of the SM is deceptive: it is extremely difficult to describe and account for phenomena that we see at a scale just above that of quarks, leptons and bosons, the building blocks of the SM. The *non-perturbative* nature of Quantum Chromo-Dynamics (QCD) in particular leads to many unsolved mysteries. The SM only allows quarks and gluons to exist in composite states: if quarks are separated, the between them becomes so strong that a new quark-antiquark pair is formed. This *confinement* property has led on the one hand to the study of the deconfined state of Quark-Gluon Plasma (QGP) in high-energy colliders, and to the study of these composite objects themselves with the use of low-energy colliders. The latter is the research discipline of *hadron spectroscopy*.

All of these developments have resulted in a remarkable renewal of interest in hadron spectroscopy. The Beijing Electron Spectrometer (BES) in Beijing, with which this master's research was done, is one of the main contributors to this field, particularly when it comes to charmed hadrons (charm and charmonium physics). The renaissance of hadron spectroscopy over the past years has been further driven by to the surprising discovery of a plethora of charmonium like XYZ states [3, 4, 5, 6]. Such regular discoveries of new particles gives us the opportunity to improve our theoretical understanding of QCD by characterise and studying their properties.

Hadron spectroscopy is, however, not mere verification of the SM. A low-every electron–positron collider such as the Beijing Electron–Positron Collider (BEPC) can produces clean collisions at high-intensity, allowing for detailed studies of discoveries made by high-energy hadron colliders, just like Large Electron–Positron Collider (LEP) pinpointed out all the details of the W and Z bosons that were discovered earlier at the Super Proton Synchrotron (SPS). The large data samples accumulated by the BESIII experiment thus enable detailed studies of processes that are forbidden by the SM, while measurements of branching ratios of extremely rare decays allow us to put predictions by BSM to the test. And it is the testing of BSM models that this master's research contributes to.

This thesis is the product of my master's research performed for the Experimental Physics master programme of Utrecht University. The research itself was performed at the Institute of High Energy Physics (IHEP) in Beijing under the supervision of Prof. Dr. Xiaoyan Shen with guidance of Prof. Dr. Beijiang Liu. Utrecht's Experimental Physics programme falls under the Institute for Subatomic

Physics (SAP), which is part of the ALICE experiment at CERN's LHC. My background and training was therefore mainly in the ALICE collaboration,[1] where research procedures and analysis tools are naturally quite different—ALICE specialises in QGP in hadron collisions at much higher collision energies.

Besides presenting obtained research results, this thesis therefore attempts to provide an elementary and practical introduction to the BESIII Collaboration and the types of HEP research performed there. As such, references are provided not only as an academic foundation to statements, but also for further reading and are therefore always provided with external URLs to related articles or web pages (some of which are only available behind IHEP's SSO login). In addition, the many abbreviations used in this field are linked and explained in Appendix C with links to further material if relevant. The document can therefore best be viewed in its original `pdf` format.

In HEP research, physics and terminology always closely goes hand-in-hand with analysis code and documentation. Since the BESIII Collaboration is smaller than the major LHC collaborations, analysis code is not as formalised and documented less extensively. A large part of this master's research project was therefore dedicated to the design of formalised code and in setting up updated, accessible documentation. These 'spin-off projects' are described in Appendices A and B.

Finally, this thesis attempts to provide a comprehensive overview of studies of $J/\psi \to DM$ decays (see Section 4.1 in particular). As such, the target audience also comprises those who wish to pursue this type of analysis, now that BESIIII's unique J/ψ data samples have reached numbers that could result in the observation of a first $J/\psi \to DM$ signal.

[1] See bachelor thesis and CERN Summer Student report.

Chapter 2

Current state of knowledge

This chapter provides a general introduction to the current state of knowledge in High Energy Physics (HEP). We start with an introduction of the Standard Model (SM) (Section 2.1), highlighting specific features that are of relevance to this research. We then have a short look into the bound states of quarks (Section 2.2), which is of importance to the type of hadron spectrometry research performed by the BESIII Collaboration. We finish with an introduction to quarkonium states (Section 2.3. The specifics of weak $J/\psi \to DM$ decays are visited in Chapter 4, because this requires some background information about the BES detector and the BEPC collider (Chapter 3).

2.1 The Standard Model

The Standard Model (SM) of particle physics is a theory that describes the most fundamental constituents of matter and the interactions between these constituents. It is a Quantum Field Theory (QFT) that is symmetric under certain gauge transformations. These symmetries help to describe fundamental forces, while fluctuations in the quantum fields lead to the 'particles' that we observe in particle collider experiments.

Four fundamental forces are observed in nature: the electromagnetic force, the weak force, the strong force, and gravity. The SM accounts for the first three of these fundamental forces. Quantum Electrodynamics (QED) is a component of the SM that describes the weak force and the electromagnetic force (also called the electroweak force), while Quantum Chromo-Dynamics (QCD) accounts for the strong force.

It is beyond the scope of this thesis to elucidate the mathematical formalism of the SM. However, the fundamental particles and forces that the SM predicts can be summarised in a simple table form, see Figure 2.1a. The model contains three types of particles: quarks, leptons, and bosons. Quark and leptons form up the matter particles and are shown shown in the left three columns of Figure 2.1a. Bosons are the force caries and are shown in the right two columns.

Leptons and quarks each come in 6 flavours. In Figure 2.1a they are organised in three generations (the columns) and two types (the rows). In the quark sector, we have the up (u), down (d), charm (c), strange (s), top (t), and bottom (b) quark. In the lepton sector, there are the electron (e), muon (μ), and tau (τ), all of which are negatively charged, and three corresponding neutrinos (ν_e, ν_μ, and ν_τ) that don't carry charge. The SM also predicts an anti-particle (anti-matter) for each of these 12 matter particles.

The SM contains five *force carriers*: four vector gauge bosons (γ, $W^\pm$, Z, and g) and one scalar Higgs boson H. These force mediators are associated with the fundamental forces: the gluon g with the strong force, the Z and $W^\pm$ bosons with the weak force, and the photon γ with the electromagnetic force. The Higgs boson generates masses by symmetry breaking and forms the crown on SM.

As can be seen in Figure 2.1b, both quarks and leptons can interact through the electroweak force. Electromagnetism operates through charge and dominates at large distances. The weak force bosons Z and $W^\pm$ are massive and is effective over shorter distances. These bosons are responsible for flavour changes: transitions between one quark into another such as $u \to d$, or one lepton into another, like $e \to \nu_e$. Transitions in the quark sector are characterised by the Cabibbo-Kobayashi-Maskawa quark

mixing matrix (CKM-matrix).

Strong force gluons interact with quarks only, because quarks and gluons the only particles that carry *colour charge*. The underlying theory of the strong force, QCD, has the unique property that its force mediator, the gluon, also carries its own characteristic (colour) charge. The coupling constant of the strong force (its 'strength') therefore displays completely different behaviour than those of the electroweak force: it increases over distance. On the one hand, this causes an effect known as *confinement*, which prohibits the existence of free (anti)quarks: if quarks move away from each other, the energy in the strong force becomes so large that a new quark-antiquark pair is formed. On the other hand, it causes *charge screening*: once a quark 'group' is held together by the strong force (a *bound state*), the gluons within that group cannot interact with other quark groups around it.

The confinement property of the strong force is an essential ingredient in explaining hadronic matter. It enables the Constituent Quark Model (CQM), which states that quarks can only exist in colourless bound states.The strong force is characterised by three colours—red, blue, and green–plus their anti-colours for anti-matter. Quark groups therefore mostly exist as either a quark-antiquark pair or in a pair of three quarks. Such groups constitute the matter that we observe and are called *hadrons*.

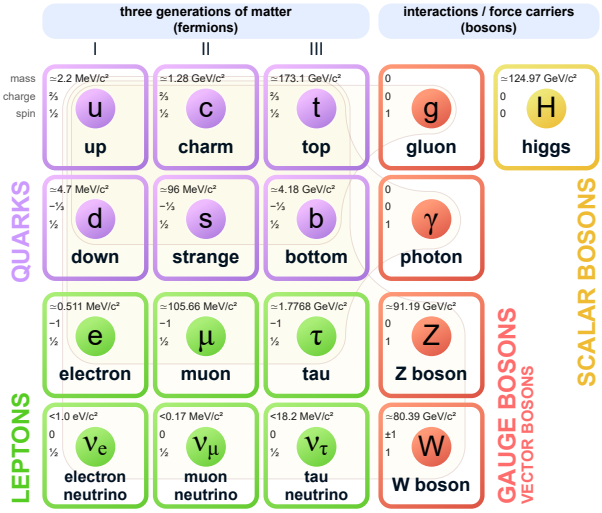

(a) Schematic overview [7].

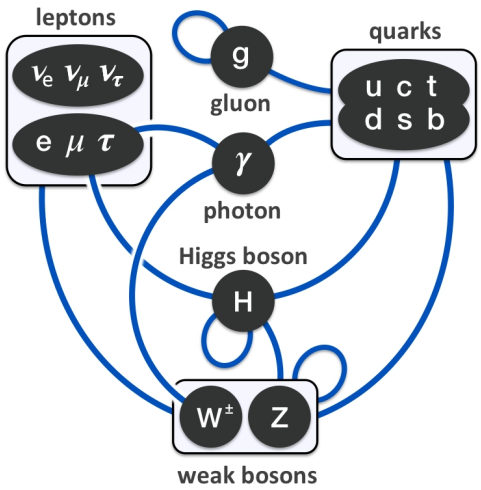

(b) Interactions between the components [8].

Figure 2.1: Constituents of the Standard Model of particle physics.

2.2 The Hadron Zoo

Prior to the formulation of the SM and the postulation of quarks and leptons, several symmetries and patterns that we can now explain in terms of the CQM had already been identified. A growing number of particles, such as the pion (initially predicted as a force carrier by Yukawa [9]) and the kaon [10], were observed in cosmic rays and in particle collider experiments. In an effort to understand this spectrum of particles, a phenomenological model was developed to characterise them. Combined with QCD, this developed into the CQM [11].

Bound states of quarks are called hadrons and the sum of their colours is colourless. For instance, a group of three quarks with colour red, green, and blue, can be in a bound state. Such a combination is called a *baryon*. A bound state of a quark and an antiquark is also colourless and is called a *meson*.

Each particle in the SM is characterised by a set of *additive quantum numbers*. Leptons and quarks for instance carry spin number $s = 1/2$, making them *fermions*. Apart from the way in which quarks and leptons interact (see Figure 2.1b), their charge Q also makes them very different: leptons have a charge or either 0 or -1, while quarks have fractional charge of either $-1/3$ (down, strange, bottom) or $2/3$ (up, charm, top). Quantum numbers of antiparticles have opposite sign.

Quarks carry several other quantum numbers that enable us to characterise their bound states. The two lightest quarks, u and d, are characterised by isospin I and the z-component of the isospin, I_z.

Heaver quarks have $I = 0$ and $I_z = 0$, but carry either strangeness ($S = -1$ for strange, rest is zero), charmness (charm has $C = +1$, other zero), bottomness ($B = -1$ for bottom, rest zero), and topness ($T = +1$ for top, rest zero). Apart from the weak force, all fundamental forces conserve these numbers.

Two other quantum numbers that are important for quarks are the baryon number $\mathcal{B}$ and hypercharge Y. The baryon number is 1/3 for all quarks, meaning that a baryon has baryon number $\mathcal{B} = +1$ and a meson has $\mathcal{B} = 0$. Hypercharge 1/3 is for the up and down quarks, $-2/3$ for the strange quark and 0 for all other quarks. Charge and hypercharge can be related to the other additive quantum numbers as follows [11]:

$$Q = I_z + \frac{\mathcal{B} + S + C + B + T}{2} \tag{2.1}$$

$$Y = \mathcal{B} + S - \frac{C - B + T}{3} \tag{2.2}$$

Quantum numbers help to characterise bound states and explain their interactions through the strong force on a phenomenological level. A nice representation of such a characterisation is given in Figure 2.2. The middle layer of each structure ($C = 0$) show an `octet`, the 8 *light meson* combinations possible with the light (anti)quarks, u, $\bar{u}$, d, $\bar{d}$, s, and $\bar{s}$. Adding the charm c, one can form a *16-plet* with a SU(4) symmetry (the $C = \pm 1$ layers and one $c\bar{c}$ *singlet* with $C = 0$). These additional mesons are the charmed D mesons plus one *charmonium* state. Similar SU(4) structures can be formed for baryons, see [11, p. 291], but we will restrict ourselves to mesons in this study.

Mesons can be further classified using J^{CP} nomenclature, which takes account of their *orbital angular momentum* L (one could imagine the quark-antiquark pair spinning around each other). Here, J is the total spin, P is the parity and C is the charge parity. On a fundamental level, P and C parity describe the behaviour of the quantum mechanical state under the symmetry operation of point reflection and charge conjugation respectively. However, these numbers can again be related to quantum numbers: $P = (-1)^{L+1}$ and $C = (-1)^{L+s}$, where s is the spin that we encountered before. There is also a *general parity* G defined as $G = (-1)^{I+L+s}$, with I the isospin. The general parity number is sometimes used in the extended label $I^G(J^{CP})$. Further distinctions can be made with *principal quantum number* n, which denotes a radial excitation, much like that of the hydrogen atom.

The above definitions allow us to classify mesons in J^{CP} *multiplets*. Mesons with $J = 1$ are either *pseudoscalars* (0^{-+}, $l = 0$) or *scalars* (0^{++}, $l = 1$), while mesons with $J = 1$ are either *vectors* (1^{-+}, $l = 0$) or *axial vectors* (1^{++}, $l = 1$), with another variant being the *tensor* (2^{++}, $l = 1$). Figure 2.2a shows a 16-plet of pseudoscalar mesons, and Figure 2.2b shows one of vector mesons.

Finally, the principal quantum number is often used in the classification label $n^{2s+1}L_J$, where L is denoted in orbital letters P, S, D, F, G, etc. For instance, the pion, kaon and eta meson are all pseudoscalar mesons in the ground state with label 1^1S_0.

While the formulation of QCD is well-established, the effects of its asymptotic freedom are extremely hard to predict, making confinement one of the outstanding problems in physics [12]. Studying the wide variety of mesons is the best way to approach this problem and the above nomenclature helps us to categorise the growing number of mesons in the hadron zoo.

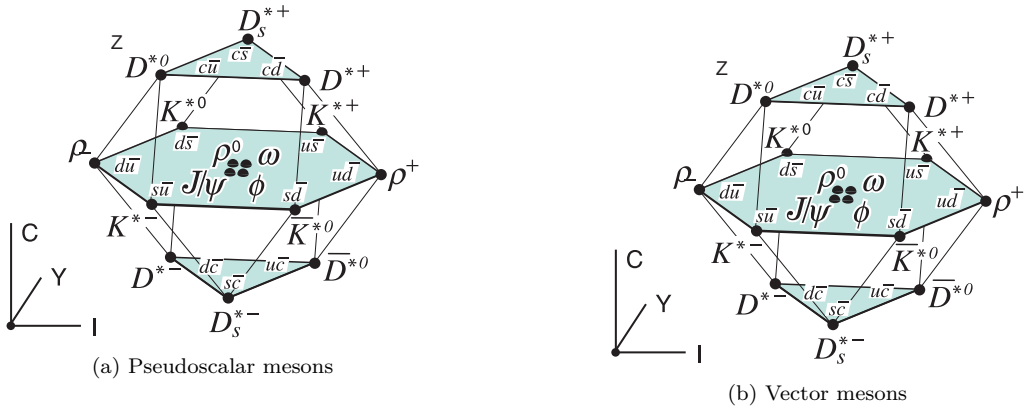

(a) Pseudoscalar mesons

(b) Vector mesons

Figure 2.2: 16-plets of mesons containing the up, down, strange, or charm [11, p. 287].

2.3 Quarkonium and charmonium

A good illustration of the use of J^{CP} can be found if we zoom in on the special case of mesons of the form $c\bar{c}$. We already encountered this meson type as the singlet in the 16-plet. This meson was initially encountered as the J/ψ meson in 1974 [13, 14], which solidified our belief in the existence of quarks [12].

Mesons that consist of a heavy quark (charm, bottom, top) and its own anti-quark, such as $c\bar{c}$, are called *quarkonium*. There are two of forms of quarkonium—the charmonium $c\bar{c}$ and bottomonium $b\bar{b}$—because the top quark decays before it can form a bound state. The configuration of quark and anti-quark has a few interesting properties. First, quarkonium states have a QCD behaviour that is fully non-perturbative and requires computations using Lattice Quantum Chromo-Dynamics (LQCD). In addition, the heavy quark pair in quarkonium moves at non-relativistic velocities, as opposed to relativistic quark pair in lighter $q\bar{q}$ mesons, which allows for a particularly rich spectrum.

Quarkonium states seem simple in the constituency, but exist in a large variety of excited states, with each state having different quantum numbers. This is where the categorisation labels that we studied before come in. The $n^{2s+1}L_J$ label in particular reminds of the excitation level scheme of the hydrogen nucleus, which is why quarkonium states are sometimes referred to as the 'positronium of QCD' [15].

In the charmonium spectrum, the $\eta_c(1S)$ pseudoscalar meson is the ground state. Next comes the $J/\psi(1S)$ vector meson. Higher excitations can decay back to these two mesons. A common way to decay is as $\psi(nS) \to \gamma\eta_c(mP)$ and $X_cJ(1P) \to \gamma J/\psi$. Some experimentally established charmonium states are given in Figure 2.3, along with some common transitions. A complete overview of all charmonium 'suspects' as of this year (2019) is given in Figure 2.1.

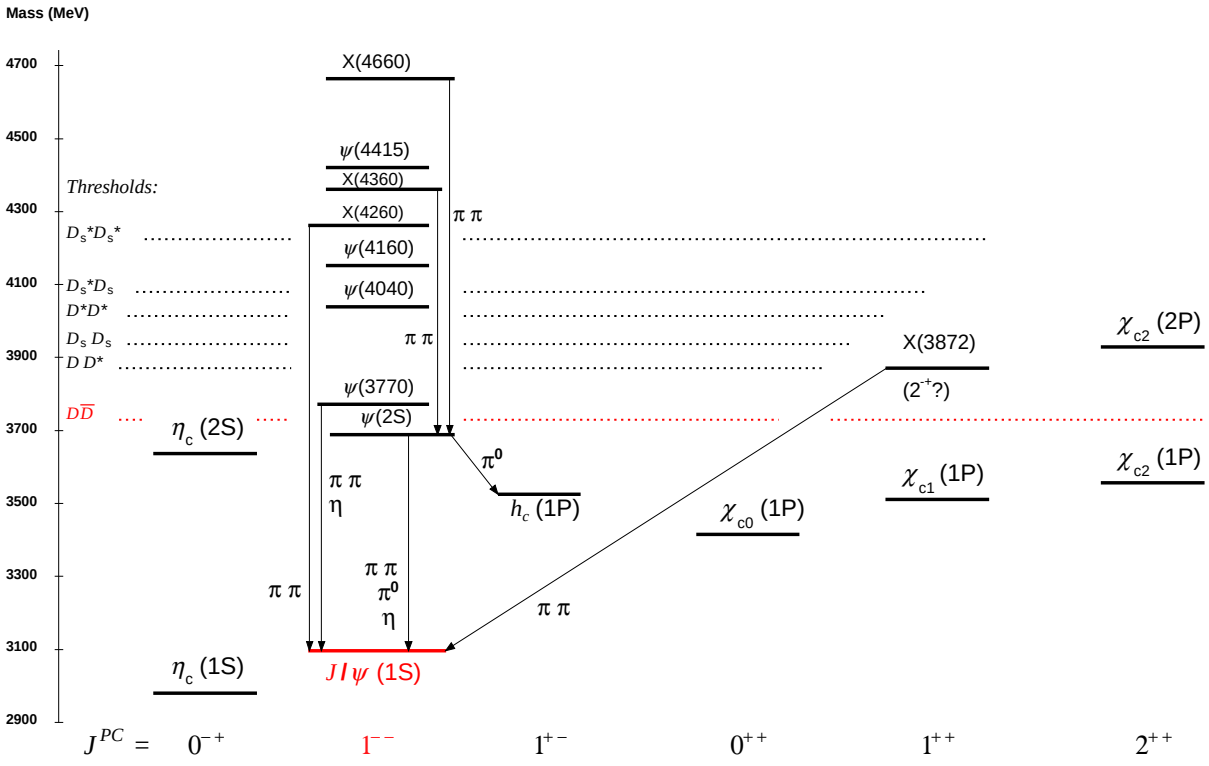

Figure 2.3: Schematic overview of charmonium states, adapted from [16]. Indicated in red is the J/ψ state and $D\bar{D}$ that form the motivation for this study. The figure also shows several decay processes.

$I^G(J^{PC})$	Meson	Previously	Mass (MeV/c^2)	PDG
$0^+(0^{-+})$	$\eta_c(1S)$		$2\,983.4 \pm 0.5$	[link]
$0^-(1^{--})$	$J/\psi(1S)$		$3\,096.900 \pm 0.006$	[link]
$0^+(0^{++})$	$\chi_{c0}(1P)$		$3\,414.75 \pm 0.30$	[link]
$0^+(1^{++})$	$\chi_{c1}(1P)$		$3\,510.66 \pm 0.07$	[link]
$0^-(1^{+-})$	$h_c(1P)$		$3\,525.38 \pm 0.11$	[link]
$0^+(2^{++})$	$\chi_{c2}(1P)$		$3\,556.20 \pm 0.09$	[link]
$0^+(0^{-+})$	$\eta_c(2S)$	η_c'	$3\,639.2 \pm 1.2$	[link]
$0^-(1^{--})$	$\psi(2S)$	$\psi(3686) = \psi'$	$3\,686.097 \pm 0.025$	[link]
$0^-(1^{--})$	$\psi(3770)$	ψ''	$3\,773.13 \pm 0.35$	[link]
$0^+(1^{--})$	$\psi_2(3823)$		$3\,822.2 \pm 1.2$	[link]
$0^+(0^{++})$	$\chi_{c0}(3860)$		$3\,862 \pm 10^{+26+40}_{-32-13}$	[link]
$0^+(1^{++})$	$\chi_{c1}(3872)$	$X(3872)$	$3\,871.69 \pm 0.17$	[link]
$1^+(1^{+-})$	$Z_c(3900)$		$3\,887 \pm 2.3$	[link]
$0^+(0 \text{ or } 2^{++})$	$X(3915)$	$\chi_{c0}(3915)$	$3\,918 \pm 1.9$	[link]
$0^+(2^{++})$	$\chi_{c2}(3930)$		$3\,927 \pm 2.6$	[link]
$?^?(?^{??})$	$X(3940)$		$3\,942^{+7}_{-6} \pm 6$	[link]
$1^+(?^{?-})$	$X(4020)$		$4\,024.1 \pm 1.9$	[link]
$0^-(1^{--})$	$\psi(4040)$		$4\,039 \pm 1$	[link]
$1^-(?^{?+})$	$X(4050)^{\pm}$		$4\,051 \pm 14^{+20}_{-41}$	[link]
$1^+(?^{?-})$	$X(4055)^{\pm}$		$4\,051 \pm 14^{+20}_{-41}$	[link]
$0^+(1^{++})$	$\chi_{c1}(4140)$		$4\,146.8 \pm 2.4$	[link]
$1^-(1^{--})$	$\psi(4160)$		$4\,191 \pm 5$	[link]
$?^?(?^{??})$	$X(4160)$		$4\,156^{+25}_{-20} \pm 15$	[link]
$1^+(1^{+-})$	$Z_c(4200)$		$4\,196^{+31+17}_{-29-13}$	[link]
$0^-(1^{--})$	$\psi(4230)$		$4\,218^{+5}_{-4}$	[link]
$1^+(0^{--})$	$R_{c0}(4240)$		$4\,239 \pm 18^{+45}_{-10}$	[link]
$1^-(?^{?+})$	$X(4250)^{\pm}$		$4\,248^{+44+180}_{-19-35}$	[link]
$0^-(1^{--})$	$\psi(4260)$	$\Upsilon(4260)$, $X(4260)$	$4\,230 \pm 8$	[link]
$0^+(1^{++})$	$\chi_{c1}(4274)$	$X(4274)$	$4\,274^{+8}_{-6}$	[link]
$?^?(?^{??})$	$X(4350)$		$4\,156^{+25}_{-20} \pm 15$	[link]
$0^-(1^{--})$	$\psi(4360)$	$\Upsilon(4360)$, $X(4360)$	$4\,368 \pm 13$	[link]
$0^-(1^{--})$	$\psi(4390)$	$X(4390)$	$4\,391.5^{+6.3}_{-6.8} \pm 1.0$	[link]
$0^-(1^{--})$	$\psi(4415)$		$4\,421 \pm 4$	[link]
$1^+(1^{+-})$	$Z_c(4430)$		$4\,478^{+15}_{-18}$	[link]
$0^+(0^{++})$	$\chi_{c0}(4500)$	$X(4500)$	$4\,506 \pm 11^{+12}_{-15}$	[link]
$0^-(1^{--})$	$\psi(4660)$	$\Upsilon(4660)$, $X(4660)$	$4\,643 \pm 9$	[link]
$0^+(0^{++})$	$\chi_{c0}(4700)$	$X(4700)$	$4\,704 \pm 10^{+14}_{-24}$	[link]

Table 2.1: Charmonium states and their properties as of 2019.
See also http://pdglive.lbl.gov/ParticleGroup.action?node=MXXX025.

Chapter 3

Experimental set-up

The Beijing Electron–Positron Collider (BEPC) with its Beijing Electron Spectrometer (BES) has been set up as the centrepiece of high-energy physics in China. We will therefore shortly investigate the history of the overarching Institute of High Energy Physics (IHEP) of China (Section 3.1) before considering the technical aspects of the accelerator and the detector (Sections 3.2 and 3.3). In the final section (Section 3.4) we will see the different types of research that have been performed by the BES Collaborations and localise the type of research that this thesis presents.

3.1 A short history of particle physics in China

In China, high energy physics research is coordinated by the Institute of High Energy Physics (IHEP), which is part of the Chinese Academy of Sciences (CAS). As in most countries, however, high energy physics was initially accommodated under more general institutes—first, in 1950 around the beginning of the People's Republic of China, as part of the Institute of Modern Physics, and later as Division One of the Institute of Atomic Energy. The study of particle physics was therefore initially considered more of a technical field with practical applications for the nation.

With U.S. President Richard Nixon's visit to China in 1972, China was set to open up to the world. The worst days of the Cultural Revolution (1966–1976) were over and Premier Zhou Enlai regained a more prominent role in forming policy. As such, he instigated China's leading high-energy physicist Zhang Wenyu to make the study of high energy physics and the research and development of accelerators to be one of the main priorities of the CAS and soon after, in 1973, approved the establishment of IHEP with Zhang as the first director [17].

Zhang Wenyu had a background in the United States and was in close touch with the American physicist Wolfgang Panofsky. After a group visit to the U.S., in 1977, China decided to build a 50 GeV proton synchrotron. Panofsky, however, was critical of this proposal: Europe and the U.S. already had similar facilities, operating at even higher energies. It would be better to invest in building an electron–positron collider, an accelerator type of which there were fewer in the West. If such a collider were

History of the BESIII Collaboration	
1973	Founding of IHEP
1977	China considers building a 50 GeV proton synchrotron
1979	First meeting of the JCCHEP
1982	Deng Xiaoping endorses e^+e^- collider
1984	BEPC officially approved; building starts
1988	First collisions in BEPC
BESI	
1989	First J/ψ peak observed
1990	J/ψ data taking begins
1991	10 million J/ψ events accumulated
1992	τ mass measurements
1995	4 million $\psi(2S)$ events accumulated
BESII	
1998	R-scan from 2 to 5 GeV
2001	51 million J/ψ events accumulated
2002	14 million $\psi(2S)$ events accumulated
2003	BEPCII approved
2004	BEPC shut-down and upgrade
BESIII	
2005	First BESIII Collaboration Meeting
2008	BESIII moves to interaction region
	First hadron events recorded
2009	106 million $\psi(2S)$ events accumulated
	225 million J/ψ events accumulated
2010	0.975 fb^{-1} accumulated at $\psi(3770)$
2011	2.9 fb^{-1} accumulated at $\psi(3770)$
2012	0.45 billion $\psi(2S)$ events accumulated
	1.3 billion J/ψ events accumulated
	XYZ data taking
2014	R-scan from 2 to 3 GeV
2019	10 billion J/ψ events accumulated

Table 3.1: The BES Collaboration year-by-year. Adapted from [15].

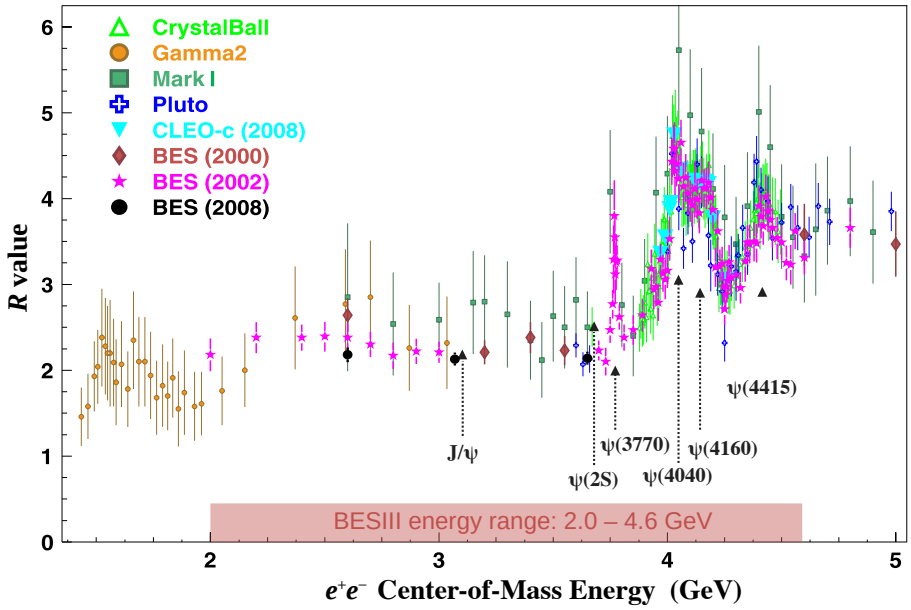

Figure 3.1: R scan values in the BESIII energy region [15].

to operate at an energy scale that had hardly been probed in other experiments, China could make significant contributions to the field of high-energy physics, despite having entering "rather late into this field" [18]. An electron-positron collider could additionally "serve the economy" by being a facility for synchrotron radiation.

It took some time before further steps were taken, since there was no immediate agreement on the best path forward, and the plans for the 50 GeV proton synchrotron were abandoned in 1980 due to changing economical perspectives [18]. Contact with the U.S. remained warm, however, with Fang Yi, vice premier of the Chinese State Council, visiting several U.S. laboratories in 1979. It was in that year that President Jimmy Carter and Vice-Chairman Deng Xiaoping signed the United States–China Agreement on Cooperation in Science and Technology, the first protocol of which—remarkably—was in high-energy physics. Under this protocol it was agreed that a Joint Committee on Cooperation in High Energy Physics (JCCHEP) was to meet on a yearly basis [19, Ch. 15] It was following the consultations of the JCCHEP that the Chinese government agreed to construct the BEPC.

In 1982, a Chinese delegation of engineers and physicists was sent to the Stanford Linear Accelerator Center (SLAC) to work out a design for the BEPC. They decided to design an accelerator with a collision energy in the range where the R value displayed peculiar behaviour (see Figure 3.1) and where the $J\psi$ meson had recently been discovered. The preliminary version of the accelerator was finalised by the summer of that year, but an intensive collaboration with SLAC continued, with a continuous presence of BEPC engineers at SLAC to buy equipment if necessary. The project even enjoyed interest from the highest levels of the government with Deng Xiaoping personally wielding the shovel at the ground-breaking ceremony on October 7th, 1984 and revisiting IHEP on October 24th, 1988 for the opening ceremony of BEPC [15].

The construction of the BEPC, with its BES detector experiment, marked the beginning of high energy physics research projects in China. Initially, IHEP continued its international collaboration mainly with the U.S., but soon received interest from other countries as well, because of the unique energy scale and luminosity reached by the BEPC—BES is the only experiment in the world to focus on charm and τ physics only [20]. By this year (2019), the BESIII collaboration reached around 500 members from 14 countries [21] and has published around 270 papers.[1]

Soon, IHEP expanded its research beyond collider physics, with the Yangbajing International Cosmic Ray Observatory in Tibet (1990), the Daya Bay Neutrino Experiment (2008)[2], and the Yutu Moon Rover (2013) [22]. Many new IHEP facilities are under construction—China Spallation Neutron Source

[1] See http://inspirehep.net/search?p=ablikim+besiii for an overview.
[2] To be succeeded by the Jiangmen Underground Neutrino Observatory (JUNO) in Kaiping in 2020

(CSNS), the Large High Altitude Air Shower Observatory (LHAASO), and the High Energy Photon Source (HEPS)—while the international community is paying close attention to the decision making around the proposed Circular Electron-Positron Collider (CEPC), the proposed successor of IHEP's current flagship [23, 24, 25].

3.2 The Beijing Electron–Positron Collider

As discussed in Section 3.1, China decided to build an accelerator that would be low on cost, but was able to probe a low energy scale that was hardly being researched by existing collaborations. It was therefore decided to have the BEPC operate at an energy of 2.2–2.8 GeV per beam, with one interaction point monitored by the Beijing Electron Spectrometer (BES). The resulting Centre-of-Mass (CM) energy region of 3–5.6 GeV had been explored before by DORIS and by SPEAR, where the J/ψ meson had been (co-)discovered in 1974 [13, 14] and promised to be a treasure trove of unexplored physics phenomena.

As can be seen in Figure 3.1, this CM energy region indeed exhibited many charmonium resonances beside the J/ψ meson. In addition, the region displays interesting behaviour of the R value defined as

$$R = \frac{\sigma(e^+e^- \to \text{hadrons})}{\sigma(e^+e^- \to \mu^+\mu^-)}, \quad (3.1)$$

which can be seen as an indication of the number of kinematically accessible quark flavours. The fluctuations of the R value below 5 GeV were not well understood, while it was important parameter in the determination of the Higgs mass [27].

Parameter	BEPC	Upgrade	BEPCII
In operation	1988–1995	1998–2004	2008–present
Detector	BESI	BESII	BESIII
Obtained luminosity ($\text{cm}^{-2}\text{s}^{-1}$)	0.7×10^{31}	4.9×10^{31}	0.853×10^{33}
at beam energy (GeV)	2.2	1.55	1.89
Beam current (A)	0.03	0.045	0.91 (nominal)
at beam energy (GeV)	2.2	1.55	
Beam energy range (GeV)	1.1 – 2.7	1.0 – 2.8	1.0 – 2.3
Circumference (m)	240.4		237.5
CM energy range (GeV)	2 – 5		2 – 4.6
Design luminosity ($\text{cm}^{-2}\text{s}^{-1}$)	0.0065		1
at beam energy (GeV)	2.2		1.89
Number of rings	1		2
Number of bunches	2×1		2×93
Crossing angle (mrad)	0		± 11

Table 3.2: Parameter comparison for the different generations of the BEPC. Sources: [15] and [26].

The BEPC and BES started operation in 1988. Since then, both accelerator and detector underwent a few upgrades in order to widen the CM energy, increase the collision luminosity, and improve the measurement precision. The original BEPC operated until 1995 and its upgrade ran between 1998 and 2004. BEPC was then upgraded to BEPCII with a much higher luminosity. This accelerator has been in use since 2008. See Table 3.2 for a comparison of the technical parameters for the different BEPC generations.

3.3 The Beijing Electron Spectrometer and its geometry

The BEPC has always had one Interaction Point (IP). As opposed to for instance proton-proton collisions at the LHC, which essentially collide 'bags' of quarks that can be in any configuration at the moment of collision, BEPC only collides electrons and positrons—elementary particles with no further decomposition—at a relatively low and specific, resonating energy. This means that the decay products of each collision can be exactly traced back to the point where the electron and positron annihilated, giving us a clear picture of the physical processes that took place during the collision. This is why the detector experiment that monitors the IP is called a *spectrometer*: the Beijing Electron Spectrometer (BES).

	Parameter	BESIII	BESII
MDC	Single wire $\sigma_{r\phi}$ (μm)	130	250
	σ_p/p (%)	0.5	2.4
	$\sigma_{dE/dx}$ (%)	6	8.5
EMC	σ_E/E (%)	2.5	22
	σ_{pos} at 1 GeV (cm)	0.6	3
TOF	σ_T (ps) barrel	100	180
	σ_T (ps) end cap	110	350
MUC	Number of layers barrel	9	3
	Number of layers end cap	8	3
	Cut-ff momentum (MeV/c)	0.4	0.5

Table 3.3: BES performance parameters[26].

Just like the BEPC, BES went through three generations, each of which was similar in design. As can be seen in Table 3.2, BESIII had to be able to process an unprecedented luminosity, so the subsystems

underwent a major upgrade. A dissection of BESIII can be seen in Figure 3.2 and some of the major resolution parameters of each of the subsystems is given in Table 3.3. The following sub-section gives an idea of the geometry and also defines some geometrical parameters. We will then investigate the technical parameters of the main sub-detectors of the current BES experiment. These sections rely mostly on [26].

3.3.1 Detector geometry

Right around the interaction point is a drift chamber. The drift chamber of BESI consisted of a Central Drift Chamber (CDC) surrounded by a Main Drift Chamber (MDC) [28]. Surrounding the drift chamber is a Time-Of-Flight (TOF) subsystem, used to identify charged particles, and around that is a Barrel Shower Counter (BSC), a calorimeter used to measure photon and particle energies. The outermost detector subsystem is the Muon Chamber (MUC) System—at the time, three layers of absorber. A conventional Solenoid Coil (SC) magnet between the MUC and TOF provided a uniform axial magnetic field over the drift chambers. In BESII, the CDC was replaced by a MarkIII vertex detector and the Multilayer Drift Chamber (MDC) and TOF were upgraded as well to be able to process the higher luminosity [29].

A similar structure of subsystems exists in the beam direction. These components are denoted "end cap" to distinguish them from the axial "barrel" components (e.g. ESC vs BSC). The beam direction is denoted as the z-direction and the axial plane is called the xy-plane, or r-direction. Since spaces between end-cap barrel subsystems create a circular 'blind spot', the *azimuthal angle* θ is an important parameter for cuts (see next sub-sections and Section 4.3). We define $\theta = 0$ to be the *z-direction*. The *polar angle* ϕ lies in the *xy-plane*, with $\phi = 0$ in the *x-direction*, but is not used for cuts in this study.

	Barrel	End cap
MDC	$\lvert\cos\theta\rvert < 0.93$	
TOF	$\lvert\cos\theta\rvert < 0.83$	$0.85 < \lvert\cos\theta\rvert < 0.95$
EMC	$\lvert\cos\theta\rvert < 0.82$	$0.83 < \lvert\cos\theta\rvert < 0.93$
MUC	$\lvert\cos\theta\rvert < 0.75$	$0.75 < \lvert\cos\theta\rvert < 0.89$

Table 3.4: Solid angular coverage of the main sub-detectors in BESIII.

Since the detector has full polar angular coverage, the value α in $|\cos\theta| < \alpha$ is equal to the *solid angle* $\Delta\Omega/4\pi$ and is therefore used as a measure for *solid angle coverage*, see Table 3.4. The angular coverage of BESIII is usually considered to be $\Delta\Omega/4\pi = 0.93$, though it is 0.89 where it considers studies that involve muons.

3.3.2 Superconducting Solenoid Magnet

The latest and third generation of BES had its conventional SC replaced by a superconducting magnet to create a 1.0 Tesla axial magnetic field in the drift chamber. This is the Superconducting Solenoid Magnet (SSM). In addition, at the end caps, as close as possible to the IP, a Solenoid Coil Quadrupole (SCQ) provides the final focusing of the beam. In Figure 3.2, both have been indicated in yellow.

As opposed to the previous two generations, BEPCII is a double ring machine with positrons stored in one beam and electrons in the other. To create the interaction point, the bundles have to be crossed inside the BESIII detector. This results in a crossing angle of 11 mrad in the xz-plane, which means the CM frame is not the same as the lab frame: seen from the lab frame, there is a momentum component in the x-direction. A positive aspect of this relatively large crossing angle is that bunches can be closely packed without resulting in unforeseen collisions. BEPCII can therefore store 93 bunches stored per ring and increase its luminosity by two orders of magnitude.

The iron barrel yoke surrounding it both enforces the magnetic field and separates muons from hadrons (pions in particular) based on their hit pattern in the instrumented flux return yoke. This allows the measurement of low-energy muons as well.

3.3.3 Multilayer Drift Chamber

The inner core of the detector is the Multilayer Drift Chamber (MDC). It is used to reconstruct tracks of charged particles in three dimensions. Since there is a strong magnetic field, charged particle are curved. Their curvature is an indication of their *specific energy loss* profile—dE/dx, which can be used for Particle Identification (PID)—and momentum p. MDC tracks are also extended by the software in an attempt to link them to tracks recorded in the TOF and MUC sub-detectors. The inner radius of the

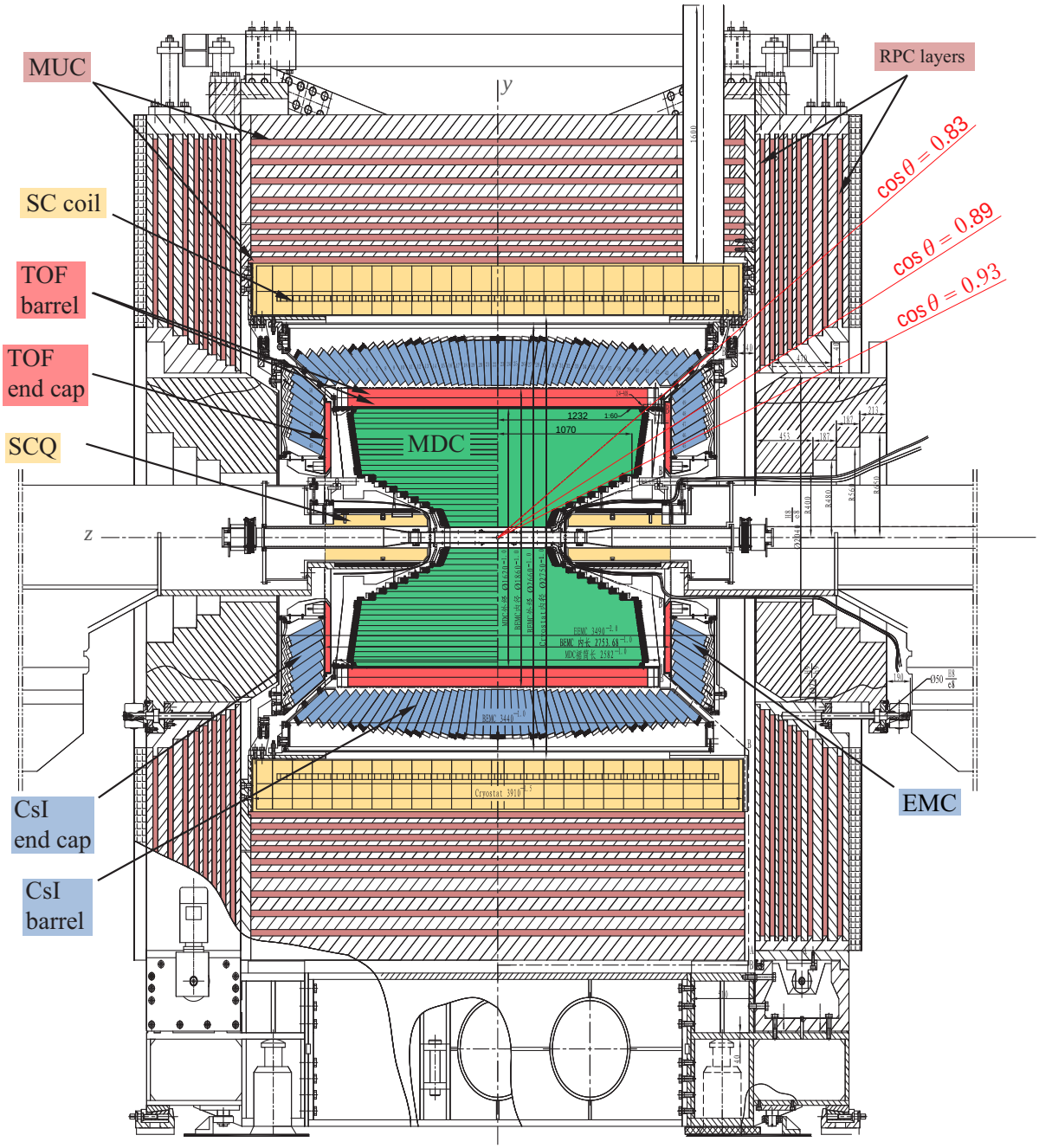

Figure 3.2: Schematic drawing of the BESIII detector and its subsystems [26, p. 348].

MDC is 59 mm and the outer radius is 810 mm. Tracks lying within the 59 mm radius can therefore only be reconstructed if they or their decay products continue into the MDC.

As opposed to the *Main* Drift Chamber of BESI and BESII, the *Multilayer* Drift Chamber of BESIII adopts a multilayer small drift cell design similar to that of CLEO-III [30]. One drift cell consists of a gold plated tungsten *sense wire* of 25 μm diameter surrounded by 8 gold plated aluminium *field wires* of 110 μm in diameter. Together, these drift cells are arranged in layers between 12–16.2 mm thick and those are arranged in 11 super layers.

By ionisation, charged particles leave a track in the He:C_3H_8 60:40 gas mixture of the MDC. This mixture is chosen to minimise multiple Coulomb scattering and obtain a good dE/dx and momentum resolution. Ionisation results in a signal in the drift cells, the profile of which can be used to determine the radial distance between the wires and the track in the $r\phi$ plane and the z-coordinates of segments

on the track. The expected position resolution in the $r\phi$ is around 130 μm and 2 mm in the z-direction.

Due to the high luminosity that was reached in the past years, the radiation dose to which the MDC has been exposed has caused ageing problems in the innermost 10 layers [31]. The current plan, however, is to have the BESIII experiment run until 2022 and beyond. An Italian group of the BESIII Collaboration is therefore working on a replacement of the inner part by a Cylindrical Gas Electron-Multiplier Inner Tracker (CGEM-IT). This is a three-layer gas tracker with a better performance than the traditional gas detector due to its multiplication stage, which can make CGEM-IT operate at a lower voltage. The resolution in the $r\phi$ plane is comparable, but the resolution in the z-direction becomes around 1 mm, which means that the vertex resolution of the fast decaying K^0_S and Λ particles becomes a factor of two to three [32]. CGEM-IT is planned to be implemented in 2020.

3.3.4 Time-Of-Flight counter

Surrounding the MDC are the Time-Of-Flight (TOF) barrel and end cap. The barrel contains of two layers of 88 scintillating bars, each 5 cm thick and located at a 81 and 86 cm radius from the z-axis. The end cap also consists of two layers of scintillating bars, 48 each and located at around 1.4 m from the IP. The solid angle coverage of the TOF barrel is $|\cos\theta| < 0.83$, while that of the end cap is $0.85 < |\cos\theta| < 0.95$. The blind spot in between is caused by the support structure of both subsystems.

Despite the compact design of BESIII, the TOF system allows for a time resolution of around 100 ps. PID is performed by combining the TOF data and dE/dx recorded by the MDC. In the final reconstructed data, 5 particles charged particles are identified: electrons (e), muons (μ), pions (π), kaons (K), and protons (p). The time resolution of the TOF system allows for a 3σ π/K separation up to around 700 MeV/c in the xy-plane.

3.3.5 Electromagnetic Calorimeter

The 25 ton Electromagnetic Calorimeter (EMC) immediately surrounding the TOF at around 94 cm from the beam measures photons and electromagnetic showers from charged particles. This is achieved with CsI(Tl) crystals, which are sensitive to low energies as well. There are 6240 of these crystals, arranged in 56 disks that are centred towards the IP.

Because of the relatively low collision energy of 2–4.6 GeV, the performance requirements of the EMC are rather specific. First of all, the energy range that the EMC should be able to detect is very wide: photons can have an energy in the range between 20 MeV and 2 GeV (from $e^+e^- \to \gamma\gamma$ processes). In addition, a common process $\pi^0 \to \gamma\gamma$ at this collision energy results in a relatively large minimum opening angle between the two γ's: for a π^0 with a momentum of 1.5 GeV it is about 10°. This means that a good position resolution is required as well to be able to perform angle cuts on photons.

The EMC is also sensitive to charged particles, in particular to pions and electrons. These particles interact with the CsI(Tl) crystals and cause photon showers. At lower energies this is a problem, because it becomes difficult to distinguish electrons from pions. Charged particles therefore need to have a momentum of at least 200 MeV/c for a reliable e/π discrimination.

3.3.6 Muon Chamber System

Wrapped around the EMC, SC, and iron yoke, between 170 and 262 cm from the beam, is the outermost sub-detector of BESIII: the 500 ton Muon Chamber (MUC) System, a muon identifier. The MUC can be used to determine whether tracks reaching this far were muons and not charged pions or other hadrons. The identification of muons is important for BESIII, because many semi-leptonic decays of charmonium states such as J/ψ involve muons. Muons are particularly important when performing R scans, but are also studied in a number of rare leptonic decays of charmed mesons.

As opposed to the 3-layer MUCs of previous BES generations, the barrel MUC consists of 9 layers of Resistive Plate Chambers (RPCs), while the end caps consist of 8 layers due to space limitations. These RPC layers are separated by 4 cm thick steel layers that further lower the momentum of the (mostly) muons. Just like in the MDC, charged particles ionise the gas in the RPC layers and create tracks that are curved by the magnetic field existing in the MUC. These tracks are then associated with tracks detected by the MDC.

Muons lose around 160 MeV of their energy in the CsI(Tl) crystals of the EMC, so muons with a momentum lower than 0.4 GeV/c are not reliably identified.

3.3.7 Trigger systems

BESIII has two types of triggers: a Level 1 (L1) *hardware* trigger and a Level 3 (L3) *software* trigger, which serves as an additional event filter before data storage. The L1 trigger is generated by the TOF, MDC, and EMC subsystems, while the L3 software trigger is mainly based on data provided by the end cap EMC.

For J/ψ events, events occur at around 2 kHz ($e^-e^+ \to J/\psi$ has a relatively large cross-section), while for ψ', they occur at around 600 Hz. The BESII detector is not located deep underground, so receives a non-trivial flux of cosmic rays. L1 triggers from the TOF and MDC reduce this from 2 kHz to around 200 Hz.

3.3.8 Beam Energy Measurement System

Clean e^+e^- collisions have a CM frame that can be measured relatively well. This is particularly important when determining the mass the τ lepton, but also allows for clean kinematic fits (used in this study). To precisely measure the energy and energy spread of the beam, BESIII makes use of the Beam Energy Measurement System (BEMS). BEMS collides photons from a CO_2 laser with the electrons or positrons from both beams. Compton scattering then causes some of these photons to be scattered back. A germanium detector then creates a profile of energy versus scattering angle of these photons. Knowing the kinematics of Compton scattering, we can then determine the energy of the beam. In this way, BEMS determines the energy spread with an accuracy of around 10^{-5} [33].

3.4 Types of research

There are several types of analysis done in the BESIII Collaboration. These analyses are categorized under five groups, with each group led by a group convener. The following exposition of these five categories is to give context to the analysis done for this thesis.

3.4.1 Charmonium physics

BESIII is often called a "τ-charm factory", because the BEPCII operates around the energy threshold of a large number of *charmonium states* (we'll come back to τ in Section 3.4.3). As discussed in Section 2.2, charmonium is any quarkonium state of a charm and an anti-charm quark. With 10 years of data taking, BESIII has the largest charmonium data sets.

The charmonium physics group not only attempts to explore the wide variety of charmonium states (or XYZ states), but also goes into the transitions between these states. As can be seen in Figure 2.3, the $\psi(2S)$ state lies just *below* the $D\bar{D}$ threshold, but above many other charmonium states, making $\psi(2S)$ a perfect state for studying transitions to charmonium states with a lower mass. These transitions are accompanied by particular decay mesons and form an additional probe to test QCD models in a regime that is somewhat perturbative [34]. In addition, reconstruction of the charmonium decay products allows for precise measurements of their masses.

Decays of ψ' should result in decays comparable to those of J/ψ, as ψ' also cannot decay to D meson pairs. Different behaviour can usually be attributed to their 12% difference in mass. There are, however, some unsolved mysteries, such as the $\rho\pi$ *puzzle*: it was found that $\mathcal{B}(J/\psi \to \rho\pi) = (2.10\pm0.12)\times10^{-2}$ [35], while $\mathcal{B}(\psi(2S) \to \rho\pi) = (5.1 \pm 1.3) \times 10^{-5}$ [36].

As for XYZ states, while BESIII is known for its surprising discovery of the tetraquark $Z_c(3900)$ [3], BESIII also studies some bottomonium states: the energy range of BEPCII just covers $\Upsilon(4260)$, $\Upsilon(4360)$, and $\Upsilon(4660)$. More detailed studies of these states are done by B-factories such as Belle II [37].

3.4.2 Charm physics

Just above the ψ' that is used for charmonium studies, lies the ψ'' meson. This charmonium state results in high, clean statistics for (charmed) D mesons, because it lies just *above* the open charm threshold,

meaning that it predominantly decays to $D\bar{D}$ pairs. BESIII therefore has one of the cleanest samples of D mesons. These samples allow for detailed studies of the CKM-matrix, three-body decays of D mesons, and searches for CP-violation ($D^0\bar{D}^0$ tagging) [38]. Some rare ψ'' decays not involving two D mesons have also been observed, with the sum of their BRs being merely 0.5% [11]. BESIII is also planning to operate at 4170 GeV to produce $D_s^{*\pm}D_s^{*\mp}$ pairs, which would highly improve our knowledge of D_s physics (charmed mesons with a strange quark).

3.4.3 R values, τ and QCD physics

Physics performed in this group are related to (1) tests of QCD through inclusive and exclusive measurements of hadronic cross sections and form and transition factors, (2) improved measurements of the mass of the τ lepton, and (3) R values scans (see Section 3.1). Precise measurements of the R value improve our knowledge of the parameters of the SM and therefore of e.g. running coupling constants in QED. Eventually, these parameters also affect theoretical studies of the mass of the Higgs boson.

3.4.4 Light hadron physics

The theory for the strong interaction of the SM is described by Quantum Chromo-Dynamics (QCD). It remains difficult to use its theoretical underpinnings for predicting behaviour of the strong force in the low-energy regime. In the high energy regime, asymptotic freedom allows theorists to apply perturbation theory. At low energies, however, non-Abelian characteristics of QCD become apparent, which means that one must resort to e.g. LQCD in order to understand the confinement properties at this energy scale [39].

The study of *light hadrons*—that is, mesons and baryons containing the light quarks up, down, and/or strange—is central to studying energy scales where perturbation theory fails and is therefore the core of hadron spectroscopy [40]. The largest data set of BESIII is that of J/ψ mesons, the lightest of the excited charmonium states with a large cross section. Since J/ψ decays almost only to light hadrons (see Section 4.1), the study of J/ψ and light hadron physics has therefore always been one of the most important features of each BES generation.

In light hadron physics, the main mode of operation is to consider final states such as $J/\psi \to \gamma\eta\eta$ and search for intermediate resonances, such as $f_0(1710) \to \eta\eta$ [41]. There can be several intermediate resonances, which results in overlapping resonance peaks, making these kinds of researches particularly difficult.

A technique to deal with this challenge is Partial Wave Analysis (PWA). PWA attempts to characterise the shapes of the peaks and relate their amplitudes. These characterisations of the distributions can then be compared with theoretical models. This *amplitude analysis* in turn allows us to extract quantum numbers and understand more about the decay process and the nature of the intermediate resonances. PWA can be applied reliably well to BESIII data because of its high statistics.

Another aspect of light hadron physics is the search for *glueballs*. Glueballs are formally no hadrons, as they are composed of gluons only, without any valence quarks [42]. Glueball production is expected to be accompanied by a photon: the J/ψ meson radiates a photon (a *radiative decay*) after which the remaining $c\bar{c}$ pair annihilates into two gluons. The gluons become a glueball state after which they hadronise. This means that glueball events are characterised by one photon, as opposed to e.g. $\gamma\gamma$ collisions. Glueballs are expected to have either quantum numbers $J^{CP} = 0^{++}$ (mass 1.5–1.7 GeV), 0^{-+} (2.3–2.6 GeV), or 2^{++} (2.3–2.4 GeV) with expected Branching Ratios (BRs) of around 10^{-4}, which means that they will be hidden from ordinary hadron resonances. Glueballs have not yet been observed, but the expectation is that, like with PWA, the newest data sets of BESIII allow to distinguish glueballs from regular meson resonances [39].

Baryons are another sector being researched at BESIII. Recent findings include the first observation of spin polarisation of Λ and $\bar{\Lambda}$ hyperons in $J/\psi \to \Lambda\bar{\Lambda}$ decays. The obtained polarisation value $\alpha_- = 0.750 \pm 0.009 \pm 0.004$ turned out to $17 \pm 3\%$ higher than the previous world average, which means that all measurements of $\Lambda/\bar{\Lambda}$ polarisation determined from α_- are too large and have to be re-evaluated [43].

Although this study investigates J/ψ decaying to a heavy meson (D^0), it falls under the the study of light hadron physics. There is, of course, also a component of New Physics (NP).

3.4.5 Exotic decays and new physics

The high statistics offered by BESIII allow to probe decays with small predicted branching ratios. In many cases, the BR predicted by the SM is too low to observe, or not even allowed, but NP models predict higher BRs, like in the case of $J/\psi \to DM$ for this study.

3.5 BESIII Offline Software System

Signals detected by the BESIII subsystems are filtered through the L3 software trigger and recorded in `raw` format on an *online* computer farm (see Section 4.4.1) [26]. Reconstruction and corrections are then performed *offline* using the BESIII Offline Software System (BOSS). This is a framework written in C++ and compiled on a Scientific Linux CERN (SLC) farm [44, 45].

BOSS has been built on code that was developed for BaBar and CLEO. The latest release is version 7.0.4, which is based on CLHEP v2.0.4.5, Gaudi v23r9., CERN's ROOT v5.34, and GEANT4 v9.3 [46, p. 26]. The framework is maintained through the Configuration Management Tool (CMT), which is based on the package based principle. BOSS is therefore continuously expanded with additional analysis packages that can be useful for other analyses.

Detector response is simulated with the BESIII Object Oriented Simulation Tool (BOOST), which is based on GEANT4. Initial event selections, such as the ones for this study, are written as Gaudi algorithms and implemented in BOSS through CMT. Guadi algorithms loop over the DST files that were generated by BOSS reconstruction algorithms.

Chapter 4

Method & Theory

4.1 The relevance of weak $J/\psi \to DM$ decays

The J/ψ meson is the lightest form of charmonium, a bound state $c\bar{c}$ of a charm and an anti-charm quark. Charmonium decays through annihilation of the $c\bar{c}$ pair, which produces intermediate gluons and virtual photons. This means that decays of the J/ψ meson are dominated by strong and electromagnetic interactions. Weak force J/ψ decays are also possible through virtual W bosons, but are rare and have therefore not been studied in detail.

A more specific form of weak J/ψ decays are those that have a single charmed D meson as decay product. Since the mass of J/ψ lies below the $D\bar{D}$ threshold, decays to $D\bar{D}$, which would conserve charmness, are kinematically forbidden. The more general decay *flavour changing* $J/\psi \to DM$, where M denotes any non-charm meson used as *tag meson* is still allowed by the SM. Such a decay involves either a transition $c \to s$ or $c \to d$, where the latter is further suppressed by the CKM-matrix. The predicted *inclusive* branching ratio is at most $\sim 10^{-8}$ [47], which has so far not been observable in recorded data sets.

Certain NP extensions to the SM do, however, result in higher branching ratios of around 10^{-6} [48]. This is a branching ratio that might be observable by the latest data of BESIII [49]. Setting an *upper limit* on the branching ratio decays of the form $J/\psi \to DM$ can therefore help us to exclude certain NP models. An upper limit tells us that the *confidence level* actual branching ratio (if non-zero at all) has to be lower than this value, thus further constraining parameters of BSM models. NP models that that would be affected by an improved upper limit are the Top Colour models [50, 51], the Minimal Super-symmetric Standard Model (MSSM) [52], the Two-Higgs-Doublet Model (2HDM) [53], and QCD factorisation [54, 55].

The LHCb Collaboration recently confirmed the first case of charge-parity (CP) violation in D^0 decays of more than five standard deviations (5σ) [56], confirming an earlier observation in 2011 of 3.5σ [57]. The CP asymmetry in the charm sector should, however, be less than 0.1% according to the SM, which means that there is indeed an indication of NP in in the 'heavy up quark' sector (charm and top) [58]. The recent finding by LHCb therefore forms an additional incentive to investigate weak charmonium decays.

The first $J/\psi \to DM$ was performed at BESII, in 2008 [59]. This fist study investigated the decays $J/\psi \to D_s^- \pi^+ + \text{c.c}$, $J/\psi \to D^- \pi^+ + \text{c.c}$, and $J/\psi \to \bar{D}^0 \bar{K}^0 + \text{c.c}$ and resulted in branching ratio upper limits of 1.3×10^{-4}, 7.5×10^{-5}, and 1.7×10^{-4} respectively at 90% CL. These decays are actually of a form $J/\psi \to DP$, where P represents a pseudoscalar meson.

With the prospect of larger data samples offered by BESIII, theoretical computations were performed to predict branching ratios according to the SM [60, 61, 58, 62]. It turned out that decays of the form $J/\psi \to DV$, where V is a vector meson, are relatively higher: around a factor of 4, which "can be expected to be measured soon" [63, p. 942]. In addition, vector meson have a polarisation, the effect of which may help in understanding the underlying dynamics of the hadron [62]. This led to the study of the decay channels $J/\psi \to D_s^- \rho^+$ and $J/\psi \to D^0 K^{*0}$ in 2014,[1] with branching ratio upper limits of 1.3×10^{-5} and 2.5×10^{-6} respectively [64].

[1] The vector mesons ρ^+ and K^{*0} are the excited states of pseudoscalar mesons π^+ and K^0 respectively.

Finally, another $J/\psi \to DV$ study is being performed using the larger 2012 BESIII data sample [65]. This study focuses on both $J/\psi \to DP/V$ decays: (1) $J/\psi \to \bar{D}^0\pi^0$ with its vector form $J/\psi \to \bar{D}^0\rho^0$ and $J/\psi \to \bar{D}^0\eta$ and (2) $J/\psi \to D^-\pi^+$ with its vector form $J/\psi \to D^-\rho^+$. The results have not yet been published, but an indication is given in Table 4.1. An overview of all relevant $J/\psi \to DP/V$ decays with their predicted BRs and BR upper limits determined by BESII/BESIII is given in Table 4.1.

As a side note, two other types of charmonium to single D meson decays are also of interest: *semileptonic* $\psi(n\mathrm{S}) \to D_{(s)}^{(*)}l^+\nu$ decays, which involve $c \to s$ or $c \to d$ transitions through a virtual W bosons (BR at most 10^{-9}), *radiative* $\psi(n\mathrm{S}) \to D^{(*)0}\gamma$ decays, and decays of the form $J/\psi \to D^{(*)0}l^+l^-$. Semi-leptonic decays have been studied in two separate BES studies [66, 67]. Radiative decays and $J/\psi \to D^{(*)0}l^+l^-$ decays have a tiny BR and have not yet been studied. The aim of this study and the three BESIII studies that preceded this study is to set an *upper limit* on the branching fraction of certain $J/\psi \to DP, DV$ decays.

	Decay type	Channel	Predicted $\mathcal{B}\left(10^{-10}\right)$				BESII/BESIII			
			[62]	[61]	[60]	[63]	E.S. (10^{-6})	UL	$N_{J/\psi}$	
c → s	$\psi(nS) \to D_{(s)}P$	$J/\psi \to D_s^-\pi^+$	7.36	2.5	2.0	8.74	9.9	1.3×10^{-4}	5.8×10^7	[59]
		$J/\psi \to D^0K^0$	1.39	0.5	0.36	2.80	13.0	1.7×10^{-4}	5.8×10^7	[59]
	$\psi(nS) \to D_{(s)}V$	$J/\psi \to D_s^-\rho^+$	50.5	28.0	12.6	36.30	2.0	1.3×10^{-5}	2.25×10^8	[64]
		$J/\psi \to D^0K^{*0}$	8.12	5.5	1.54	10.27	0.38	2.5×10^{-6}	2.25×10^8	[64]
	$\psi(nS) \to D_{(s)}^*V$	$J/\psi \to D_s^{*-}\rho^+$			52.6		1.7			
c → d	$\psi(nS) \to D_{(s)}P$	$J/\psi \to D_s^-K^+$	0.53		0.16	0.55	9.8			
		$J/\psi \to D^-\pi^+$	0.29		0.08	0.55	0.21	7.5×10^{-5}	5.8×10^7	[59]
								1.1×10^{-6}	2.25×10^8	[65]
		$J/\psi \to D^0\eta$	0.070			0.016	0.72	5.0×10^{-6}	2.25×10^8	[65]
		$J/\psi \to D^0\eta'$	0.004			0.003	0.25			
		$J/\psi \to D^0\pi^0$	0.024			0.055	0.48	3.1×10^{-6}	2.25×10^8	[65]
	$\psi(nS) \to D_{(s)}V$	$J/\psi \to D_s^-K^{*+}$	2.79		0.82	2.12	5.4			
		$J/\psi \to D^-\rho^+$	2.13		0.42	2.20	0.35	2.2×10^{-6}	2.25×10^8	[65]
		$J/\psi \to D^0\rho^0$	0.18			0.22	0.77	4.8×10^{-6}	2.25×10^8	[65]
		$J/\psi \to D^0\omega$	0.16			0.18	0.35	2.1×10^{-6}	1.00×10^{10}	
		$J/\psi \to D^0\phi$	0.41			0.65	0.22	3.4×10^{-7}	1.00×10^{10}	
	$\psi(nS) \to D_{(s)}^*V$	$J/\psi \to D_s^{*-}K^{*+}$			2.6		4.5			
		$J/\psi \to D^{*-}\rho^+$			2.8		0.083			
		$J/\psi \to D^{*-}K^{*+}$			9.6		0.027			

Table 4.1: Overview of predicted $J/\psi \to DP/V$ branching ratios and current upper limits. Indicated in red are the two decay channels investigated for this study. E.S. stands for estimated sensitivity for a sample of 10^{10} events and has been estimated from existing analyses [40].

4.2 Decay channels

As can be seen in Table 4.1, this fourth study into weak $J/\psi \to DM$ decays in BES investigates the last $J/\psi \to DV$ decays that had not been measured yet (excluding those that do not involve an excited D meson): $J/\psi \to D^0\omega$ and $J/\psi \to D^0\phi$.[2] Both $\phi(1020)$ and $\omega(782)$ are vector mesons with $I^G\left(J^{PC}\right) = 0^-(1^{--})$. Their predicted branching ratios are rather small—between 10^{-11} and 10^{-10}—and it should be noted that these branching ratios are *inclusive*, that is to say, summing all different branching ratios of D^0, ϕ, and ω [62, 63].

Figure 4.1 shows the Feynman diagrams of both weak J/ψ decays. It can be seen that we are dealing with a $c \to s$ (Cabibbo-allowed) and $c \to d$ (Cabibbo-suppressed) transition respectively. Note that ω is suppressed more strongly, because it is only created in its $d\bar{d}$ projection, while

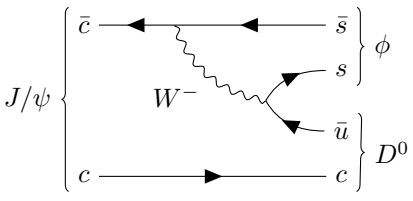

(a) $J/\psi \to D^0\phi$

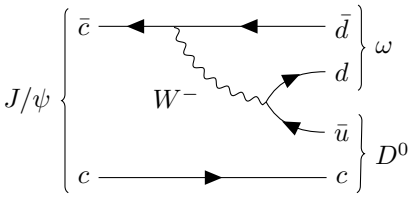

(b) $J/\psi \to D^0\omega$

Figure 4.1: Feynman diagrams of investigated weak $J/\psi \to DV$ decay channels.

[2] Excited D mesons are even rarer and therefore harder to study.

$\omega = \frac{1}{\sqrt{2}}\left(u\bar{u} + d\bar{d}\right)$. It should also be noted that ϕ and ω are mesons that occur in many J/ψ decays, which means we can expect a lot of background noise.

Choosing a suitable reconstruction method for ω and ϕ is straightforward. For ϕ, the decay channel with the largest BR is $\phi \to K^+K^-$ with a BR of $(49.2 \pm 0.5)\%$. Smaller, non-negligible decay channels ($K^0_S K^0_S$, $\pi^+\pi^-\pi^0$, $\eta\gamma$, ...) are harder to reconstruct. The ω meson decays predominantly to $\pi^+\pi^-\pi^0$ with a BR of $(89.3 \pm 0.6)\%$. Here, we reconstruct π^0 through $\pi^0\gamma\gamma$ with a BR of $(98.823 \pm 0.034)\%$. Other properties are listed in Table 4.3.

Choosing a reconstruction method for D^0 is difficult: the D^0 meson has around 340 known decay channels [11]. For this study, it was decided early on to use a simple reconstruction method, using the *hadronic* decay channel $D^0 \to K^-\pi^+$, which has a BR of $(3.89 \pm 0.04)\%$. This decay channel allows for a straightforward PID selection (e.g. no complications from electrons and Bremsstrahlung) and enables direct reconstruction of the D^0 mesons through invariant mass of the charged decay products (see Kinematic fit). All in all, the final states we are dealing with are:

$$J/\psi \to D^0\omega \to K^-\pi^+\pi^+\pi^-\gamma\gamma \qquad (4.1)$$

$$J/\psi \to D^0\phi \to K^-\pi^+K^+K^- \qquad (4.2)$$

	Decay mode	Branching fraction
Γ_{19}	$D^0 \to K^-e^+\nu_e$	$(3.530 \pm 0.028)\%$
Γ_{20}	$D^0 \to K^-\mu^+\nu_\mu$	$(3.31 \pm 0.13)\%$
Γ_{29}	$D^0 \to \pi^-e^+\nu_e$	$(2.91 \pm 0.04)\% \times 10^{-3}$
Γ_{30}	$D^0 \to \pi^-\mu^+\nu_\mu$	$(2.37 \pm 0.24)\% \times 10^{-3}$
Γ_{32}	$D^0 \to K^-\pi^+$	$(3.89 \pm 0.04)\%$
Γ_{33}	$D^0 \to K^0_S\pi^0$	$(1.19 \pm 0.04)\%$
Γ_{35}	$D^0 \to K^0_S\pi^+\pi^-$	$(2.75 \pm 0.18)\%$
Γ_{50}	$D^0 \to K^-\pi^+\pi^0$	$(14.2 \pm 0.5)\%$
Γ_{67}	$D^0 \to K^-\pi^+\pi^+\pi^-$	$(8.11 \pm 0.15)\%$
Γ_{86}	$D^0 \to K^0_S\pi^+\pi^-\pi^0$	$(5.1 \pm 0.6)\%$
Γ_{129}	$D^0 \to \pi^+\pi^-\pi^0$	$(1.47 \pm 0.06)\%$

Table 4.2: Important D^0 decay channels, from PDG 2019.

In all previous studies, however, the D^0 is reconstructed through the *semileptonic* decay channel $K^-e^+\bar{\nu}_e$ with branching ratio $(3.530 \pm 0.028)\%$. Although the invisible anti-neutrino $\bar{\nu}_e$ makes it impossible to directly identify the D meson by its invariant mass of the decay channel, this semileptonic decay channel is expected to result in smaller combinatorial background than when using a hadronic decay channel. This is not only because BESIII registers a relatively large amount of hadron tracks from conventional hadronic J/ψ decays, but also because the reconstruction method of the tag mesons ϕ and ω also makes use of hadronic decay channels, which results in K^-/π^+ combinations respectively (see Section 4.3).

Table 4.2 gives an overview of the D^0 decay channels with the largest branching ratios. As can be seen, hadronic decay channels with more pions have a larger branching ratio, but they result in even more combinations. In follow-up studies, these channels can be investigated too, because they may slightly increase the eventual upper limit (see Chapter 6).

Meson	Content	Mass (MeV/c^2)	Width (MeV/c^2)	$I^G\left(J^{PC}\right)$	PDG
$J/\psi(1S)$	$c\bar{c}$	3096.900 ± 0.006	92.9 ± 2.8	$I^G\left(J^{PC}\right) = 0^-\,(1^{--})$	[link]
D^0	$c\bar{u}$	1864.84 ± 0.05		$I\left(J^P\right) = \frac{1}{2}\,(0^-)$	[link]
$\phi(1020)$	$s\bar{s}$	1019.461 ± 0.016	4.249 ± 0.013	$I^G\left(J^{PC}\right) = 0^-\,(1^{--})$	[link]
$\omega(782)$	$\frac{1}{\sqrt{2}}\left(u\bar{u} + d\bar{d}\right)$	782.65 ± 0.12	8.49 ± 0.08	$I^G\left(J^{PC}\right) = 0^-\,(1^{--})$	[link]
π^0	$u\bar{d}$	134.9770 ± 0.0005	4.5936 ± 0.0005	$I^G\left(J^{PC}\right) = 1^-\,(0^{-+})$	[link]
$\rho^0(770)$	$\frac{1}{\sqrt{2}}\left(u\bar{u} + d\bar{d}\right)$	775.26 ± 0.25	147.8 ± 0.9	$I^G\left(J^{PC}\right) = 0^+\,(1^{--})$	[link][3]
$K^\pm$	$u\bar{s}/s\bar{u}$	493.677 ± 0.013		$I\left(J^P\right) = \frac{1}{2}\,(0^-)$	[link]
K^0_S	$\frac{d\bar{s}-s\bar{d}}{\sqrt{2}}$	497.611 ± 0.013		$I\left(J^P\right) = \frac{1}{2}\,(0^-)$	[link]

Table 4.3: Properties of mesons that are appear in this study.

4.3 Event selection

This section goes through the event selection process and lists the cuts that were applied to tracks and reconstructed candidates. For this study, we applied cuts that are commonly used in BESIII studies. An

overview of all cuts on tracks can be found in Table 4.4. In the following, *initial event selection* refers to cuts applied when running BOSS analysis code on the `lxslc` server over reconstructed data sets (DST files). *Final event selection* are cuts that are applied when running an analysis locally over the output of BOSS (ROOT files). These are mainly invariant mass cuts and cuts on the χ^2 of the kinematic fits, which have to be optimised, so they are treated in Chapter 5.

4.3.1 Charged track selection

As discussed in Section 3.3, charged tracks are reconstructed from hits in the MDC. The IP is reconstructed from the selected charged tracks using least-square and Kalman methods in the `VertexFit` package of BOSS [68]. We call the smallest distance between a track and the IP the Distance of Closest Approach (DCA). With this definition, we want the DCA to be less than 1.0 cm in the xy-plane and less than 5.0 cm in the z-direction. The azimuthal angle θ has to suffice $|\cos\theta| < 0.93$ (see Figure 3.2). Finally, the number of charged tracks is required to be four in total and events in which the sum of charges of all tracks is non-zero are rejected (only *zero net charge events*).

Charged tracks	
DCA in xy plane	< 1.0 cm
DCA in z direction	< 5.0 cm
maximal azimuthal angle	$\lvert\cos\theta\rvert < 0.93$
Particle Identification	
kaon: Prob(K) > Prob(π) and Prob(K) > 0.1%	
pion: Prob(π) > Prob(K) and Prob(π) > 0.1%	
Neutral tracks	
Photon candidate energy	
barrel ($0.8 < \lvert\cos\theta\rvert < 0.93$)	> 25 MeV/c^2
end cap ($\lvert\cos\theta\rvert < 0.8$)	> 50 MeV/c^2
angle with nearest charged track	$> 20^\circ$
EMC time requirement	$0 \leq T \leq 14$ (50 ns)

Table 4.4: Overview of cuts

4.3.2 Particle Identification

The BOSS package `ParticleID` combines information from the TOF and from dE/dx as determined by the MDC resulting in *PID probability* Prob(i), where i is the particle type (i.e., any of five most common charged particles: pion, kaon, electron, proton, and muon). In this study, we identify Prob(π) > Prob(K) with Prob(π) > 0.1% as a pion and Prob(K) > Prob(π) with Prob(K) > 0.1% as a kaon. K versus π mis-identification is expected to be around 1% [69].

4.3.3 Photon selection

The $J/\psi \to D^0\omega$ decay has a final state with two photons. Photon candidates are reconstructed by clustering energies from the EMC (see Section 3.3.5). We require photons registered by the barrel ($|\cos\theta| < 0.80$) to be at least 25 MeV and 50 MeV if detected in the end caps ($0.86 < |\cos\theta| < 0.92$). We also require a Time-to-Digital Converter (TDC) time requirement of $0 \leq T \leq 14$ (50 ns). Events with fewer than two photons are rejected.

4.3.4 Kinematic fit

The fact that the CM system in BESIII collisions is precisely known allows us to perform a so-called *Kalman kinematic fit*. This is a kinematic fit that makes use of a Kalman filter algorithm. A *kinematic fit* can be used to improve parameter resolutions of the selected tracks by comparing them to certain kinematic constraints. Such a fit applies the least-square method to obtain a χ^2 *value*.

In decays where all tracks of the final state are known (as opposed to decays involving e.g. neutrinos) it is common to apply a *four-constraint fit* (4C-fit). This means that we constrain the total 4-momentum of the selected tracks to be $(\vec{p}, E) = (0.034, 0, 0, 3.097)$, where E is the collision energy (tuned to the mass of J/ψ) and $\vec{p}$ is the 3-momentum of the CM system (remember from Section 3.3.2 that the crossing angle of the beams results in a momentum in the x-direction). The quality of such a fit is characterised by the resulting χ^2_{4C} value and is used to reject events in the final event selection.

The photon candidates are used in $J/\psi \to D^0\omega$ to reconstruct the neutral pion π^0 coming from $\omega \to \pi^+\pi^-\pi^0$. This is done by applying an additional *resonance constraint* to the kinematic fit: the invariant mass of two photons is constrained to be $m_{\pi^0} = 0.134977$ GeV/c^2. In this case, the resulting

χ^2 is labelled χ^2_{5C} (5C-fit). During the initial event selection, a kinematic Kalman fit is performed for all photon combinations and the combination with the lowest χ^2_{5C} is selected.

4.3.5 Neutral candidate reconstruction

Say a neutral candidate decays as $M \to X_1 X_2 \cdots X_n$, then the *invariant mass* $M(X_1 X_2 \cdots X_n)$ of the decay products $X_1, X_2, \cdots, X_n$ is defined as:

$$M(X_1 X_2 \cdots X_n) = \sqrt{\left(\sum_{i=0}^{n} E_i\right)^2 + \left|\sum_{i=0}^{n} \vec{p}_i\right|^2} \qquad (4.3)$$
$$\text{with} \quad |\vec{v}|^2 := v_x^2 + v_y^2 + v_z^2$$

During the initial event selection, the invariant mass of the candidate decay products of the D^0 meson and the tag meson are computed and stored for further analysis during the final event selection. In $J/\psi \to D^0\phi$, there are two combinations to consider because of the double K^-, see Equation (4.1) and Figure 4.2b. We choose the combination for which $|M(K^+K^-) - m_\phi|$ is smallest. As can be seen in Equation (4.2) and Figure 4.2a, the double π^+ results in two combinations for $J/\psi \to D^0\omega$. Here, we choose the combination for which $\left|M(\pi^+\pi^-\pi^0) - m_\omega\right|$ is smallest. We store the invariant masses $M(K^+K^-)$ resp. $M(\pi^+\pi^-\pi^0)$ of the best combination (as well as some other invariant masses, see Section 5.2) so that we can apply cuts on them in the final event selection.

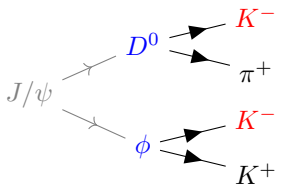

(a) $J/\psi \to D^0\phi$

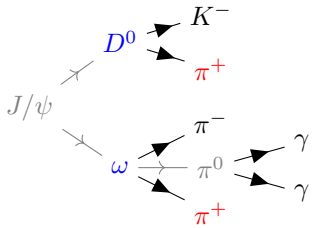

(b) $J/\psi \to D^0\omega$

Figure 4.2: Decay chains, with combinatorial mesons in red and reconstructions in blue.

4.4 Data samples

4.4.1 Measured data sample

BEPCII operates in so-called *rounds*. A round is a period of a few months during which the BEPC operates at certain beam energies. These energies are agreed upon in advance by the collaboration through proposals, while maintenance is performed during the shut-down between the rounds. An overview of the eleven rounds recorded up to this year is given in Table 4.5.

Data-taking takes place during *runs*. A run lasts around 45 minutes (in the case of J/ψ). This is the time in which both the positron and electron beam have sufficient luminosity. After one run, BESIII stops most of its subsystems so that BEPC has a few minutes to inject new bunches of electrons and positrons ("top-off" injection scheme). In 2019, tests were successfully performed for continuous injection. This will remove the need to operate in 45-minute runs ("top-up" injection scheme) and increase the luminosity by around 30% [21, 40].

Round	Runs	Dates	Types
02	08093–10878	07/03/09 – 28/07/09	ψ', 3.65 GeV, J/ψ
03	11414–14604	18/01/10 – 25/06/10	ψ''
04	20448–24141	12/12/10 – 02/06/11	ψ'', $\psi(4040)$
05	24897–28648	21/12/11 – 16/06/12	τ-scan, ψ', 3.08 GeV, J/ψ, R-scan
06	29677–33772	15/12/12 – 06/06/13	XYZ, 3.65 GeV
07	34011–38140	10/12/13 – 29/05/14	R-scan, XYZ
08	39355–43253	31/12/14 – 18/06/15	R-scan
09	43716–47349	09/01/16 – 26/06/16	4.18 GeV
10	47543–52332	16/12/16 – 13/06/17	XYZ, χ_{c1}, $\chi_{c1}(3872)$
11	52940–56546	08/12/17 – 14/06/18	J/ψ, 3.08 GeV, τ-scan, ψ'-scan, J/ψ
12	56788–62823	18/11/18 – 20/06/19	J/ψ, 3.08 GeV, XYZ

Table 4.5: Data taking rounds with run numbers, dates and research types.

Measurements are written in serialised `raw` format ('online' data). These files are large and too unwieldy for analysis, because they contain information about direct hits in for instance the MDC. These files therefore have to be 'converted' to *reconstructed* data sets (DST files). This offline reconstruction is done whenever a new version of BOSS comes out, because the reconstruction process is sometimes improved in updates.

This analysis makes use of the four rounds of J/ψ data measured at BESIII (rounds `02`, `05`, `11`, and `12`), which amounts to 10.0×10^9 J/ψ events. The analysis was run over data sets that were reconstructed under BOSS version 7.0.3 for events measured in rounds `02` and `05` (2009 and 2012) and BOSS version 7.0.4 for rounds `11` and `12` (2018).

An overview of the included runs and of the number of J/ψ events is given in Table 4.6. The number of J/ψ events for rounds `02` and `05` are accurately determined: 1310.6 ± 7.0 [70]. Note that the statistical uncertainty of the combined rounds is lower, because common uncertainties were added indirectly and the independent ones in quadrature. Numbers for 2018 have been determined only roughly [71] and the statistical uncertainty has not yet been determined. For this research, we therefore use the same statistical uncertainty percentage for rounds `11` and `12` as for that of `02+05` (see Section 5.4).

round	runs	dates	number of events	$N_{J/\psi}$	BOSS version
`02`	08093–10878	2009/03/07 – 2009/07/28	$(223.7 \pm 1.4) \times 10^6$	0.63%	7.0.3
`09`	24897–28648	2011/12/21 – 2012/06/16	$(1086.9 \pm 6.0) \times 10^6$	0.55%	7.0.3
`11`	52940–56546	2017/12/08 – 2018/06/14	4.6×10^9	(0.53%)	7.0.4
`12`	56788–59015	2018/11/18 – 2019/02/06	4.1×10^9	(0.53%)	7.0.4
		total:	10.0×10^9		

Table 4.6: BESIII data samples

4.4.2 Monte Carlo simulations

Monte Carlo (MC) simulations aim to simulate e^+e^- as accurately as possible. A simulation therefore simulates both physics processes and detector effects. Since detector effects are simulated, simulations make use of detector parameters of the real runs, so their output samples correspond to the conditions of actual BEPC rounds. Output from MC simulations is the same as that of BESIII measurements, stored in *raw* format. If we then run the same analysis over the reconstructed MC data, we end up with distributions of which we know the underlying processes.

Simulation types

Generally, there are two types of MC simulation: *inclusive* and *exclusive* simulations. An inclusive simulation is a 'cocktail' of as many decay processes as possible, following the branching ratios listed in the Particle Data Group (PDG) and thus attempting to emulate what happens in real collisions. In an exclusive simulation, the branching ratios of decay channels are overwritten by the user. Usually, this means that the user sets the branching ratios of the decay processes that occur in the studied decay process to 100%. In this case, all events in the simulated sample are the decay process in which we are interested, so we call such an exclusive simulation sample a *signal MC*.

Signal MC samples help us to determine mass resolutions of reconstructed particles (in our case, those of D^0, ϕ, and ω). The mass resolution is characterised by a *signal width* σ. We use this width to apply a 3σ *cut* on the measured data and inclusive MC. Signal MC samples are also used to determine *selection efficiency* ϵ: when we run the initial and final event selection algorithm over the reconstruction of the sample, many events will be rejected, because of (simulated) mis-identifications by the detector. The selection efficiency is defined as $\epsilon = N_{\text{all cuts}}/N_{\text{tot}}$ where N_{tot} is the total number of simulated exclusive events and $N_{\text{all cuts}}$ is the number of events that have passed all the cuts of the event selection (the *yield*).

Inclusive MC samples allow us to study possible background contributions and (in the case of rare decays) to optimise cuts using a so-called Figure-Of-Merit (FOM) (see Section 5.3.1). Background contributions are studied using 'MC truth', that is, by tracing back the decay processes that constitute certain regions of interest in eventual distributions. A listing of all contributions to a certain background region is called a background *topology*.

Event generators

MC simulations make use of so-called *generators* to simulate individual decay processes [44]. In other words, generators simulate the physical distributions of the decay processes, while the rest of the simulation is to simulate the response by the detector (done in GEANT4 [72, 73, 74]). It is therefore important to choose the right MC for each decay process simulated in the *exclusive* MC simulation.

BESIII makes use of two kinds of generators: those that have been developed for BESII, amounting to around 30 models, and those that have been taken over from the `EvtGen` package, which was developed for B physics experiments [75, 37]. The `EvtGen` package developed into the `BesEvtGen` package for τ–charm physics [76].

In this study, we followed the decay sample cards used for the inclusive MC data set (see `DECAY.DEC`). See Table 4.7 for an overview.

Studied samples

For this study, we generated a sample of 1 billion exclusive $J/\psi \to D^0\omega, D^0 \to K^-\pi^+, \omega \to \pi^-\pi^+\pi^0, \pi^0 \to \gamma\gamma$ events and 1 billion exclusive $J/\psi \to D^0\phi, D^0 \to K^-\pi^+, \phi \to K^-K^+$ events, with detector parameters picked from all four BEPC rounds. The events were generated and reconstructed with BOSS version 7.0.4 using the generators listed in Table 4.7 [76].

Decay	**Generator**	**Suitable for** [77]
$D^0 \to K^-\pi^+$	`PHSP`	Any decay, evenly distributed in phase-space
$J/\psi \to D^0\omega$	`VVS_PWAVE`	$V \to VS$, e.g. $a_0^0, J/\psi \to \rho\pi$
$J/\psi \to D^0\phi$	`VVS_PWAVE`	$V \to VS$, e.g. $a_0^0, J/\psi \to \rho\pi$
$\phi \to K^+K^-$	`VSS`	$V \to SS$, e.g. $J/\psi \to K\bar{K}$
$\omega \to \pi^+\pi^-\pi^0$	`OMEGA_DALITZ`	$\omega \to \pi\pi\pi$
$\pi^0 \to \gamma\gamma$	`PHSP`	Any decay, evenly distributed in phase-space

Table 4.7: `BesEvtGen` generators used to generate exclusive MC samples for this study.

The `PHSP` generator generates a homogeneous distribution and is suitable for pseudoscalar decays. The `VSS` generator simulates a vector meson decaying to two pseudoscalar mesons. The `VVS_PWAVE` generator simulates a vector meson decaying to a vector meson and a scalar meson. Such a decay results in an invariant mass distribution that has a tail in the higher end of the spectrum. Finally, `OMEGA_DALITZ` is a special generator for three-body decays of ω. The same generators are also used for the corresponding processes in the inclusive MC simulations.[76]

The BESIII Collaboration currently has inclusive MC samples available for rounds `02` and `05`. We used all $(0.225 + 1.0) \times 10^9 = 1.2 \times 10^9$ events in these samples. The samples were reconstructed in BOSS version 6.6.4.

Chapter 5

Results & Analysis

In the previous chapters, we set the buildings blocks for this research. This chapter shows the results obtained with the data analysis performed for this study. We first have a look at the Probability Density Function (PDF) models we have used to characterise the signal and background of invariant mass distributions (Section 5.1). These PDFs are then fit to the mass distributions from both MC and from measured data to determine mass window cuts (Section 5.2). This leads us to the final event selection, where we have a look at the resulting cut flow, reconstruction efficiencies, and background topologies (Section 5.3). Finally, this gives us a shot at setting an upper limit on the branching ratios (Section 5.5) and in determining the corresponding systematic uncertainties (Section 5.4).

5.1 Probability Density Functions

As explained in Section 4.4.2, we use exclusive MC samples to determine the mass resolution of the reconstructed particles. We do this by fitting a Probability Density Function (PDF) to their their invariant mass distributions (in the form of a histogram) and extracting relevant fit parameters. A PDF is a mathematical model that can consist of several components and that can be fit to the histogram shape or data point collection.[1]

There are several types of functions that are usually applied in HEP research to characterise invariant mass distributions of resonances. Generally we can categorise them in *background PDFs* and *signal PDFs*. A good understanding of signal PDF models is especially important in the low momentum transfer region, because complicated, non-perturbative effects start to contribute to the resonances and therefore to experimental observables [78]. A short description of some common models relevant for this study are given in the following two sections.

Models can be combined by summing them with a scaling factor or by convoluting them. We call the scaling factor for signal PDFs N_{S}, and N_{B} for the sum of all background PDFs.

5.1.1 Signal PDFs

Gaussian

A Gaussian is a simple normal distribution with the following form:

$$f_{\mathrm{Gauss}}(x) = \frac{1}{\sqrt{2\pi\sigma^2}} e^{-\frac{(x-\mu)^2}{2\sigma^2}} \tag{5.1}$$

where μ is the mean of the peak (mass) and σ is the standard deviation (mass width). The shape of a resonance can be rather specific, because of correlations caused by for instance momentum transfers in the underlying decay process. A Gaussian therefore hardly ever accurately describes the shape of physical resonance. It can, however, be used to reproduce 'smearing' effects caused by the many independent random effects in the detectors: the Central Limit Theorem (CLT) establishes that the sum of such variable distributions converge towards a normal distribution. This 'smearing' is achieved by convoluting

[1] Probability Density Functions should be normalised to 1, because probabilities should add up to 100%. In the following equations, we ignore the normalisation factor.

a PDF of choice with a sum of Gaussians, all of which are centred around $\mu = 0$. The 'detector width' is then the quadratic sum of the σ's of the Gaussian components.

Non-relativistic Breit-Wigner
Abbreviated to BW; also called Lorentz distribution or Cauchy distribution. This model is often used if the width of the resonance structure is narrow and if there are no energy thresholds or other resonances nearby [78]. The formula for a Breit-Wigner PDF is, in simplified form,

$$f_{\mathrm{BW}}(x) = \frac{c}{(x - m_0)^2 + c^2}, \tag{5.2}$$

where m_0 is the *location parameter* indicating the peak (mass) of the resonance. It is incorrect to use the sum Breit-Wigner (BW) functions to describe nearby resonances due to couplings (in such a situation, one should use K-matrix approximations).

Voigtian
One of the most commonly used distributions: simply a BW convoluted with one Gaussian. See Figure 5.1a.

'BW$_l$-wave'
When fitting the ϕ resonance, we followed fit procedures of the analysis that led to [79]. The study attempted to fit an invariant mass distribution from the decay $\phi \to K^+K^-$ using the following form of the *relativistic* BW function:

$$f_l(x) = \frac{F_m(q)}{m_0^2 - x^2 - im_0\Gamma(x,q)} \tag{5.3}$$

$$F_l(q) = \frac{\sqrt{1 + (Rq_0)^2}}{\sqrt{1 + (Rq)^2}} \tag{5.4}$$

$$\Gamma(x,q) = \Gamma(m_0)\left(\frac{q}{q_0}\right)^{2l+1} \tag{5.5}$$

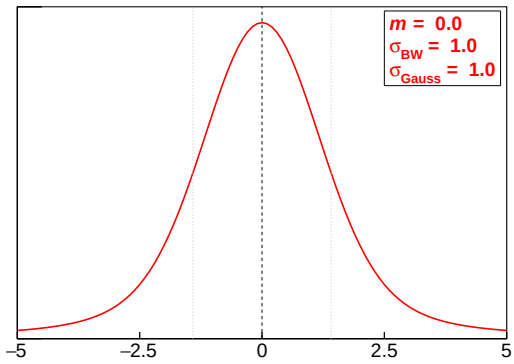

(a) Voigtian: BW$_1$-wave convoluted with Gaussian

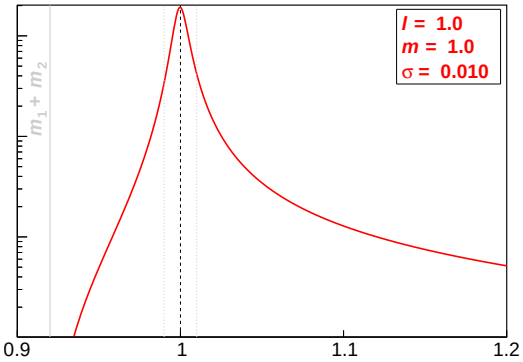

(b) BW$_1$-wave with $m_1 = m_2 = 0.46$ (log scale)

Figure 5.1: Two important signal PDFs used in this study. The lines indicate the mean m with $m \pm \sigma_{\mathrm{tot}}$ values around it.

with $R = 1.5$ GeV^{-1} and l the angular momentum of the mother particle ($l = 1$ in the case of vector meson ϕ). This formula is more complicated than it seems in that q is the momentum of one of the K's in the rest frame of ϕ, while q_0 is q evaluated at $x = m_0$. In the lab frame, this transforms to:

$$f_l(x) = \frac{m_0\sigma C(x)}{\left(x^2 - m_0^2\right)^2 + C(x)^2 m_0^2\sigma^2} \tag{5.6}$$

$$C(x) = \frac{m_0^2}{x^2}\left(\frac{m_0\sqrt{\left(x^2 - m_+^2\right)\left(x^2 - m_-^2\right)}}{x\sqrt{\left(m_0^2 - m_+^2\right)\left(m_0^2 - m_-^2\right)}}\right)^{2l+1} \tag{5.7}$$

$$m_\pm = m_1 \pm m_2. \tag{5.8}$$

Here, m_1 and m_2 are the masses of the two decay products. In the case of $\phi \to K^-K^+$, we have $m_+ = 2m_K = 0.987 \pm 0.026$ GeV/c^2 and $m_- = 0$.

For lack of a better term, we call Equation (5.6) a 'BW$_l$-wave', where l is the angular momentum. An important feature of this distribution is that the distribution goes to 0 at $x = m_1 + m_2$, which represents an energy threshold on the left side, see Figure 5.1b.

'Histogram PDF'
Here, we simply use the shape of the exclusive MC distribution as a 'function' for the signal. This is the easiest type of PDF, as it involves only one fit parameter: a scaling parameter.

5.1.2 Background PDFs

Polynomial
Any shape can be approached by a sum of polynomials (Taylor series), so a polynomial is commonly used to describe backgrounds that we do not understand well. We have to be careful, however, not to make the model fit too perfect (which is always possible at higher degrees), because this could affect the signal strength (and therefore the determined branching ratio). We therefore typically use either 1^{st} or 2^{nd} order polynomials (a line or parabola respectively).

Chebychev polynomial of the first kind
Similarly to an ordinary polynomial, Chebychev polynomials can be used for interpolating between data points, meaning that the higher the polynomial, the better the model approaches the data. A Chebychev polynomial of the first kind is defined by means of the cosine, the second kind by means of the sine [80, Ch. 1]. Chebychev polynomials can be evaluated faster, which makes them ideal for fitting procedures [81, p. 29].

Truncated polynomial
A truncated polynomial is comparable to the BESIII Argus shape (see below) in the sense that it can also be used to describe the energy threshold effect on the low-energy side of the spectrum. It has the following form:

$$f_{\text{tr}}(x) = (x - m_0)^a e^{-bx - cx^2}. \tag{5.9}$$

Initially, this polynomial was considered to be used as an alternative for the 'BESIII Argus' shape.

Argus
This formula models the phase-space of multi-body decays near an energy threshold. For us, the most important feature is that it has a cut-off value m_0 above which the distribution vanishes, because we also see such behaviour in background distributions near the upper energy threshold (right side) at the mass of J/ψ minus the sum of the masses of the decay products. The form of the Argus background shape is:

$$f_{\text{Argus}}(x) = x \left(1 - \frac{x^2}{m_0^2}\right)^p \exp\left[c\left(1 - \frac{x^2}{m_0^2}\right)\right]. \tag{5.10}$$

The Argus PDF shape is shown in Figure 5.2a.

'BESIII Argus shape'
This is a modification of the Argus background function to model the lower energy threshold of a distribution (left side) with the following form:

$$f_{\text{BESIII}}(x) = (x - m_0)^p e^{-c(x - m_0)} \tag{5.11}$$

Here, p and c are some tweaking parameters, and m_0 is the cut-off value (see Figure 5.2b).

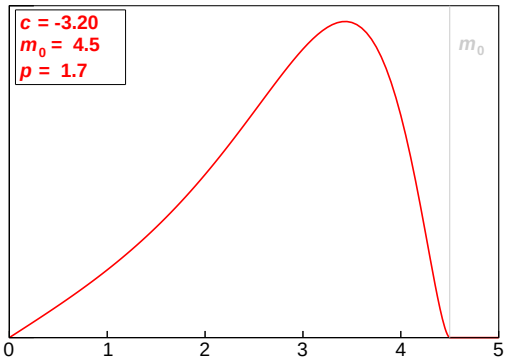

(a) Standard Argus shape from Eq. (5.10)

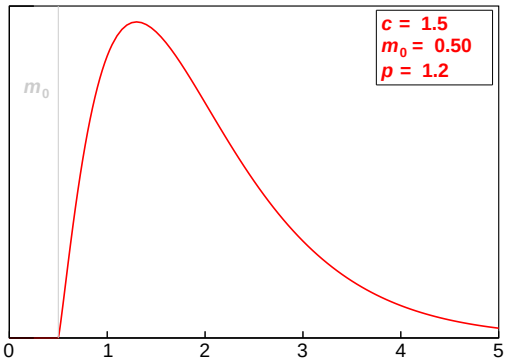

(b) Special 'BESIII Argus' shape from Eq. (5.11)

Figure 5.2: The two Argus background PDF types used in this study.

5.2 Mass window cuts

With these PDF models, we are now ready to fit the exclusive MC distributions (Section 4.4.2) for the particles we are reconstructing. The resulting fits are given in Figure 5.4 and an overview of the chosen PDF models and computed parameters are given in Table 5.1. The selected mass windows correspond roughly with the 3σ *range* defined as $[m_0 - 3\sigma_{\text{tot}}, m_0 + \sigma_{\text{tot}}]$. The fit for π^0 serves more as a test—a $M\gamma\gamma$ mass windows it not applied, because we use an additional resonance constraint on $\gamma\gamma$ in the kinematic fit (5C-fit).

Channel	PDF	$m_0 \pm \sigma_{\text{tot}}$ (GeV/c^2)	Mass window (GeV/c^2)
$D^0 \to K^-\pi^+$	Voigtian	1.8716 ± 0.0040	$1.85 < M(K^-\pi^+) < 1.89$
$\phi \to K^-K^+$	BW-wave $\circledast$ Gauss	1.0191 ± 0.0061	$1.00 < M(K^-K^+) < 1.04$
$D^0 \to K^-\pi^+$	Voigtian	1.8652 ± 0.0040	$1.84 < M(K^-\pi^+) < 1.89$
$\omega \to \pi^+\pi^-\pi^0$	Voigtian	0.7822 ± 0.0128	$0.74 < M(\pi^-\pi^+\pi^0) < 0.82$
$\pi^0 \to \gamma\gamma$	Voigtian	0.1340 ± 0.0065	$0.12 < M(\gamma\gamma) < 0.15$
$K_S^0 \to \pi^-\pi^+$	Voigtian+1$^{\text{st}}$ Chebychev	0.4965 ± 0.0055	$0.46 < M(\pi^-\pi^+) < 0.52$
$K^+ \to \pi^0\pi^+$	Voigtian+1$^{\text{st}}$ Chebychev	0.4915 ± 0.0108	$0.46 < M(\pi^0\pi^+) < 0.52$
$\rho^+ \to \pi^0\pi^+$	Voigtian+1$^{\text{st}}$ Chebychev	0.7525 ± 0.1062	$0.60 < M(\pi^0\pi^+) < 0.90$

Table 5.1: Mass window determination from fit parameters. PDF fits to $\pi\pi$ resonances (last three rows) were determined from BESIII measured data, the rest comes from fits to exclusive MC data. Compare Table 4.3.

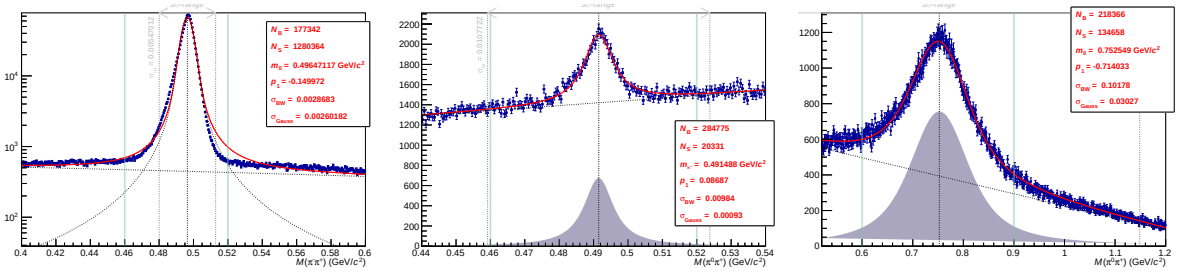

(a) $K_S^0 \to \pi^-\pi^+$ (b) $K^+ \to \pi^0\pi^+$ (c) $\rho^+ \to \pi^0\pi^+$

Figure 5.3: Fits of additional $\pi\pi$ resonances in study of $J/\psi \to D^0\omega$. In each of the above fits, a Voigtian was used as signal PDF and a 2$^{\text{nd}}$ order Chebychev polynomial as background PDF.

5.2.1 Cuts on $\pi\pi$ resonances

The table also lists a few $\pi\pi$ resonances. In an attempt to find a cause for the additional resonance in $M(\pi^+\pi^-\pi^0)$ near m_ω (see Section 5.2.2), we studied the Dalitz plots of the omega decays and found some additional resonances, both in BESIII measured data and in the inclusive MC data set. The distributions and corresponding fits of what looks like resonances of $K_S^0 \to \pi^-\pi^+$, $K^+ \to \pi^0\pi^+$, and $\rho^+ \to \pi^0\pi^+$ for measured data are shown in Figure 5.3.

Since the same resonance appear in inclusive MC, we can also investigate the decay topologies in specific invariant mass windows. In the case of K_S^0, we can investigate the decay topologies for the region $\chi^2_{\text{5C}} < 25$, $0.492 < M(\pi^+\pi^-) < 0.503$, which results in the following list of topologies:

N_i	**Primary decay**	**Secondary decays**
55,206	$J/\psi \to \pi^0 K^- K^{*+}$,	$K^{*+} \to \pi^+ K^0$, $K^0 \to K^0_S$, $K^0_S \to \pi^+\pi^-$
41,596	$J/\psi \to \rho^+ K^0 K^-$,	$\rho^+ \to \pi^0\pi^+$, $K^0 \to K^0_S$, $K^0_S \to \pi^+\pi^-$
33,021	$J/\psi \to \pi^0 K^0 \bar{K}^*$,	$K^0 \to K^0_S$, $\bar{K}^* \to \pi^+ K^-$, $K^0_S \to \pi^+\pi^-$
14,370	$J/\psi \to \pi^+ K^* K^-$,	$K^* \to \pi^0 K^0$, $K^0 \to K^0_S$, $K^0_S \to \pi^+\pi^-$
10,085	$J/\psi \to \pi^+ K^0 K^{*-}$,	$K^0 \to K^0_S$, $K^{*-} \to \pi^0 K^-$, $K^0_S \to \pi^+\pi^-$
9,039	$J/\psi \to K^- K_1^{'+}$,	$K_1^{'+} \to \pi^+ K^*$, $K^* \to \pi^0 K^0$, $K^0 \to K^0_S$, $K^0_S \to \pi^+\pi^-$
8,336	$J/\psi \to \pi^+ K^0 K_2^{*-}$,	$K^0 \to K^0_S$, $K_2^{*-} \to \pi^0 K^-$, $K^0_S \to \pi^+\pi^-$
8,080	$J/\psi \to K^- K_1^{'+}$,	$K_1^{'+} \to \pi^0 K^{*+}$, $K^{*+} \to \pi^+ K^0$, $K^0 \to K^0_S$, $K^0_S \to \pi^+\pi^-$
7,947	$J/\psi \to \pi^+ K_2^{*0} K^-$,	$K_2^{*0} \to \pi^0 K^0$, $K^0 \to K^0_S$, $K^0_S \to \pi^+\pi^-$
...	(154 topologies remaining ...)	

As can be seen by the secondary decays indicated in red, this region indeed mostly contains $K^0_S \to \pi^+\pi^-$. The same is the case for ρ^+ in the $M(\pi^0\pi^+)$ distribution. In the region $\chi^2_{\text{5C}} < 25, 0.72 < M(\pi^+\pi^-) < 0.80$, $M(\pi^+\pi^-) \notin [0.46, 0.52]$(we exclude the $K^0_S \to \pi^-\pi^+$ resonance), we have the following list:

N_i	**Primary decay**	**Secondary decays**
3374	$J/\psi \to \pi^0 K^0 \bar{K}^*$,	$K^0 \to K^0_S$, $\bar{K}^* \to \pi^+ K^-$, $K^0_S \to \pi^+\pi^-$
2526	$J/\psi \to \rho^+ K^0 K^-$,	$\rho^+ \to \pi^0\pi^+$, $K^0 \to K^0_S$, $K^0_S \to \pi^+\pi^-$
385	$J/\psi \to \pi^+ K_2^{*0} K^-$,	$K_2^{*0} \to \pi^0 K^0$, $K^0 \to K^0_S$, $K^0_S \to \pi^+\pi^-$
361	$J/\psi \to \pi^+ K^0 K_2^{*-}$,	$K^0 \to K^0_S$, $K_2^{*-} \to \pi^0 K^-$, $K^0_S \to \pi^+\pi^-$
327	$J/\psi \to \bar{K}^* K_2^{*0}$,	$\bar{K}^* \to \pi^+ K^-$, $K_2^{*0} \to \pi^0 K^0$, $K^0 \to K^0_S$, $K^0_S \to \pi^+\pi^-$
320	$J/\psi \to \pi^0 K^- K^{*+}$,	$K^{*+} \to \pi^+ K^0$, $K^0 \to K^0_S$, $K^0_S \to \pi^+\pi^-$
285	$J/\psi \to \pi^0 K^- K_2^{*+}$,	$K_2^{*+} \to \pi^+ K^0$, $K^0 \to K^0_S$, $K^0_S \to \pi^+\pi^-$
280	$J/\psi \to \rho^+ a_2^-$,	$\rho^+ \to \pi^0\pi^+$, $a_2^- \to \bar{K}^0 K^-$, $\bar{K}^0 \to K^0_S$, $K^0_S \to \pi^+\pi^-$
273	$J/\psi \to K^{*-} K_2^{*+}$,	$K^{*-} \to \pi^0 K^-$, $K_2^{*+} \to \pi^+ K^0$, $K^0 \to K^0_S$, $K^0_S \to \pi^+\pi^-$
...	(117 topologies remaining ...)	

Indeed, it also contains a large contribution of $\rho^+ \to \pi^0\pi^+$ decays. If however, we look in the region $0.488 < M(\pi^+\pi^-) < 0.495$, where we expect to see $K^+ \to \pi^0\pi^+$, we end up with a list that doesn't show any significant $\pi^0\pi^+$ resonances.

N_i	**Primary decay**	**Secondary decays**
305	$J/\psi \to \pi^0 K^- K^{*+}$,	$K^{*+} \to \pi^+ K^0$, $K^0 \to K^0_S$, $K^0_S \to \pi^+\pi^-$
268	$J/\psi \to \pi^0 K^0 \bar{K}^*$,	$K^0 \to K^0_S$, $\bar{K}^* \to \pi^+ K^-$, $K^0_S \to \pi^+\pi^-$
223	$J/\psi \to \pi^+ K^* K^-$,	$K^* \to \pi^- K^+$
132	$J/\psi \to K^- K_1^{'+}$,	$K_1^{'+} \to \pi^+ K^*$, $K^* \to \pi^- K^+$
104	$J/\psi \to K^* K_2^{*0}$,	$K^* \to \pi^- K^+$, $K_2^{*0} \to \pi^+ K^-$
99	$J/\psi \to \rho^0 K^+ K^-$,	$\rho^0 \to \pi^+\pi^-$
90	$J/\psi \to \pi^+ K_2^{*0} K^-$,	$K_2^{*0} \to \pi^- K^+$
83	$J/\psi \to \pi^- \bar{K}^* K^+$,	$\bar{K}^* \to \pi^+ K^-$
81	$J/\psi \to \pi^- K_2^{*0} K^+$,	$K_2^{*0} \to \pi^+ K^-$
80	$J/\psi \to \rho^+ K^0 K^-$,	$\rho^+ \to \pi^0\pi^+$, $K^0 \to K^0_S$, $K^0_S \to \pi^+\pi^-$
67	$J/\psi \to \bar{K}^* K_2^{*0}$,	$\bar{K}^* \to \pi^+ K^-$, $K_2^{*0} \to \pi^- K^+$
...	(113 topologies remaining ...)	

To conclude, it is unclear where the resonance in this region comes from. We do, however, decide to use the cut $M(\pi^0\pi^+) \notin [0.46, 0.52] \cup [0.6, 0.90]$ (see Table 5.1), because it hardly effects the selection efficiency (see Table 5.2b), while this cut does remove the two peaks shown in Figures 5.3b and 5.3c.

5.2.2 Double π^0 peak

As mentioned in Section 5.2.1, a shifted π^0 resonance peak was observed in the $M(\gamma\gamma)$ distribution. The peak can be seen in Figure 5.5. Here, it also becomes clear that the shifted peak comes from around higher values of χ^2_{5C} (Figure 5.5a) and that it is a kinematic fit problem: Figure 5.5a shows that the momenta of the 'shifted π^0 resonance' is shifted to lower values of $M(\gamma\gamma)$, which means that some mass is unaccounted for (either a missing track or a misidentified particle).

Figure 5.6b shows that the shifted π^0 resonance results in a strong resonance near the ω region in which we are interested. Fortunately, as can be seen in Figure 5.6a, the largest part of this 'shifted

ω resonance' is located at $\chi^2_{\text{5C}} > 25$, so the cut $\chi^2_{\text{5C}} < 25$ should suffice in the analysis of $J/\psi \to D^0\omega$. The list below shows the main topologies in the inclusive MC that contribute to the regions indicated in blue in Figure 5.6. As can be seen, most of the 'shifted ω peak' indeed come from $\omega \to \pi^0\pi^-\pi^+$.

N_i	**Primary decay**	**Secondary decays**
7284	$J/\psi \to \pi^+\pi^-\omega$,	$\omega \to \pi^0\pi^+\pi^-$
3613	$J/\psi \to \pi^- b_1^+$,	$b_1^+ \to \pi^+\omega$, $\omega \to \pi^0\pi^+\pi^-$
1872	$J/\psi \to \omega f_2(1270)$,	$\omega \to \pi^0\pi^+\pi^-$, $f_2(1270) \to \pi^+\pi^-$
502	$J/\psi \to \pi^0\pi^+\pi^+\pi^-\pi^-$	
87	$J/\psi \to \omega f_0(1370)$,	$\omega \to \pi^0\pi^+\pi^-$, $f_0(1370) \to \pi^+\pi^-$
72	$J/\psi \to \pi^+ b_1^-$,	$b_1^- \to \pi^-\omega$, $\omega \to \pi^0\pi^+\pi^-$
47	$J/\psi \to \omega f_0(980)$,	$\omega \to \pi^0\pi^+\pi^-$, $f_0(980) \to \pi^+\pi^-$
32	$J/\psi \to \rho^0 a_2^0$,	$\rho^0 \to \pi^+\pi^-$, $a_2^0 \to \pi^-\rho^+$, $\rho^+ \to \pi^0\pi^+$
28	$J/\psi \to \rho^0 a_2^0$,	$\rho^0 \to \pi^+\pi^-$, $a_2^0 \to \pi^+\rho^-$, $\rho^- \to \pi^0\pi^-$
19	$J/\psi \to \pi^0\pi^- a_1^+$,	$a_1^+ \to \rho^0\pi^+$, $\rho^0 \to \pi^+\pi^-$
12	$J/\psi \to \pi^+\pi^- a_1^0$,	$a_1^0 \to \pi^-\rho^+$, $\rho^+ \to \pi^0\pi^+$
...	(59 topologies remaining ...)	

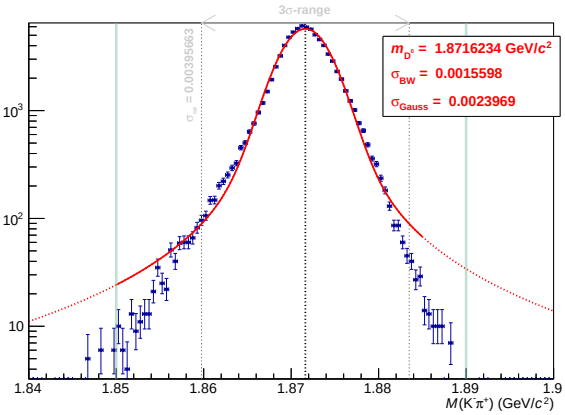

(a) Fit of $D^0 \to K^-\pi^+$ from $J/\psi \to D^0\phi$: Voigtian

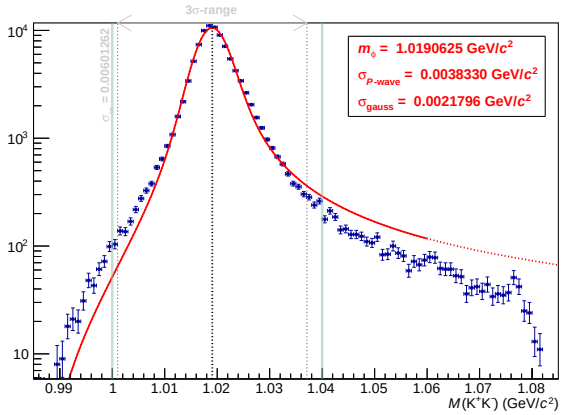

(b) Fit of $\phi \to K^-K^+$ from $J/\psi \to D^0\phi$: BW_1-wave-wave convoluted with one Gaussians

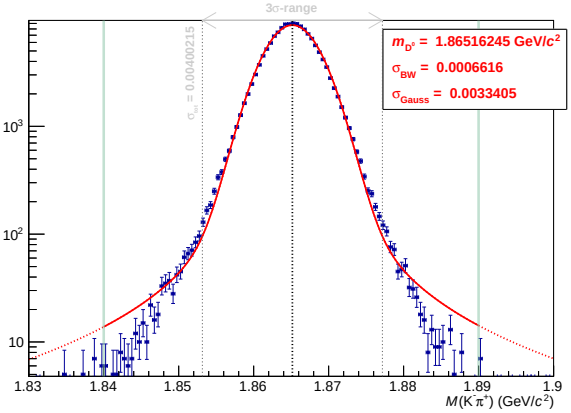

(c) Fit of $D^0 \to K^-\pi^+$ from $J/\psi \to D^0\omega$: Voigtian

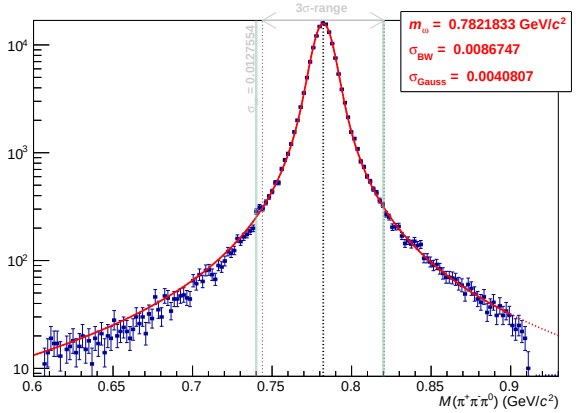

(d) Fit of $\omega \to \pi^-\pi^+\pi^0$ from $J/\psi \to D^0\omega$: Voigtian

Figure 5.4: Different fits of signal Monte Carlo data to determine mass windows. The solid red line indicates the fit of the PDF, where it becomes dashed is an extension outside the fit range. Vertical dashed, gray lines indicate the 3σ range with the determined mass in the middle. Compare Table 4.3.

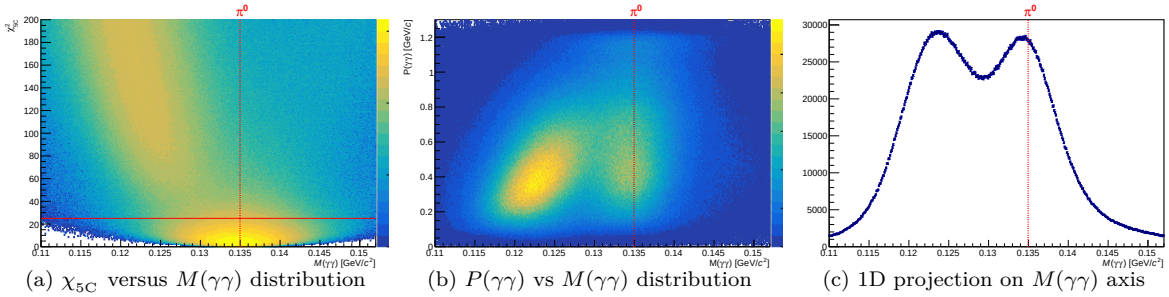

(a) χ_{5C} versus $M(\gamma\gamma)$ distribution (b) $P(\gamma\gamma)$ vs $M(\gamma\gamma)$ distribution (c) 1D projection on $M(\gamma\gamma)$ axis

Figure 5.5: Problematic additional resonance near $M(\gamma\gamma) = m_{\pi^0}$. The red solid line indicates the eventual $\chi < 25$ cut. The red dashed line indicates $M(\gamma\gamma) = m_{\pi^0}$ in GeV/c^2.

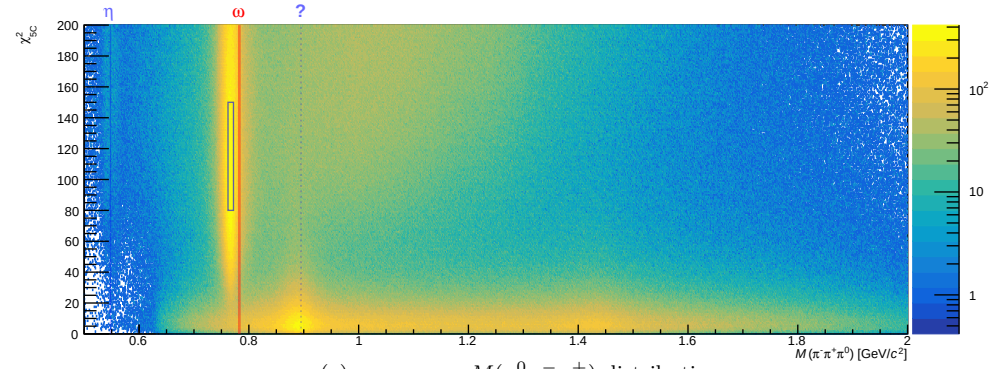

(a) χ_{5C} versus $M(\pi^0\pi^-\pi^+)$ distribution.

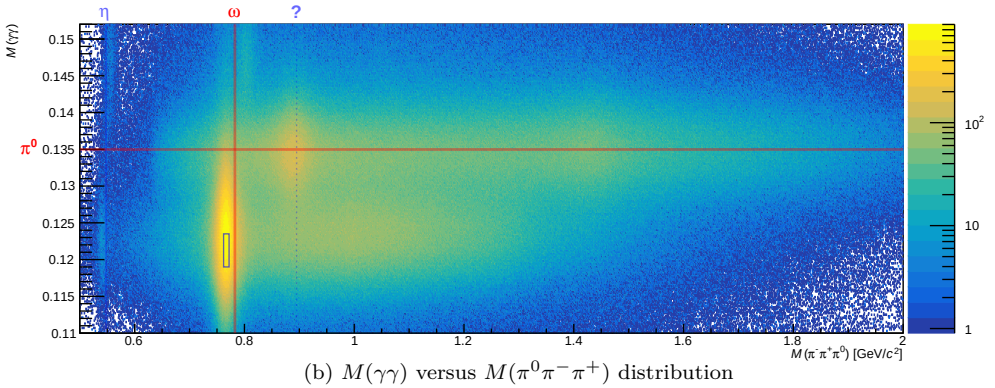

(b) $M(\gamma\gamma)$ versus $M(\pi^0\pi^-\pi^+)$ distribution

Figure 5.6: Effect of the double peak $M(\gamma\gamma)$ on $M(\pi^0\pi^-\pi^+)$ distribution. Indicated in red are $M(\pi^0\pi^-\pi^+)$ where we expect resonances. The shifted ω resonance clearly originates from the shifted π^0 peak in $M(\gamma\gamma) \approx 125$ MeV/c^2 and from higher χ^2_{5C} values. The blue rectangles indicate the topology regions discussed in Section 5.2.2.

5.3 Final event selection

5.3.1 Optimising χ^2 of the kinematic fit

Now that we have determined the mass window cuts, there is one more cut to determine before we can compute the selection efficiency: the cut on the χ^2 values of the kinematic Kalman fit. This cut is optimised by looking at its effect on the selection efficiency.

Cuts are normally optimised by looking at some ratio that takes into account the number of background events N_{B} and number of signal events N_{S}. In our case, however, since the investigated decay channel is a rare decay, we cannot determine N_{S}: both inclusive MC and measurements do not contain $J/\psi \to D^0 V$ contributions. We therefore have to define a particular Figure-Of-Merit (FOM), see [37, pp. 59–60].

In this study, we use the following FOM: $\frac{\epsilon_{\mathrm{sig}}}{\sqrt{\epsilon_{\mathrm{sig}}+\epsilon_{\mathrm{bck}}}}$. Here, ϵ_{sig} is defined as the selection efficiency of the signal MC (that is, the percentage of events that remains after all cuts, including the χ^2 cut) and ϵ_{bck} is the selection efficiency of the inclusive MC. This is a reliable measure of N_{B}, because the inclusive MC data set does not contain $J/\psi \to DM$ decays. For comparison, both ϵ_{sig} and ϵ_{bck} are scaled to 1 at $\chi^2 < 200$.

Figure 5.7 shows the χ^2 distributions for exclusive MC (signal), inclusive MC (background), and BESIII measurements (labelled "data") along with a comparison of ϵ_{bck}, ϵ_{sig}, and the corresponding FOM.

The optimal cut on χ^2 is defined to be the maximum value of the FOM. For $J/\psi \to D^0\phi$, this is $\chi^2_{\mathrm{4C}} < 90$. For $J/\psi \to D^0\omega$, the optimisation procedure is not reliable due to the double π^0 peak discussed in Section 5.2.2. We therefore do not use the cut value of 50, but we stick with $\chi^2_{\mathrm{5C}} < 25$. As can be seen in Table 5.2b, this stricter cut reduces the selection efficiency by 86.5%.

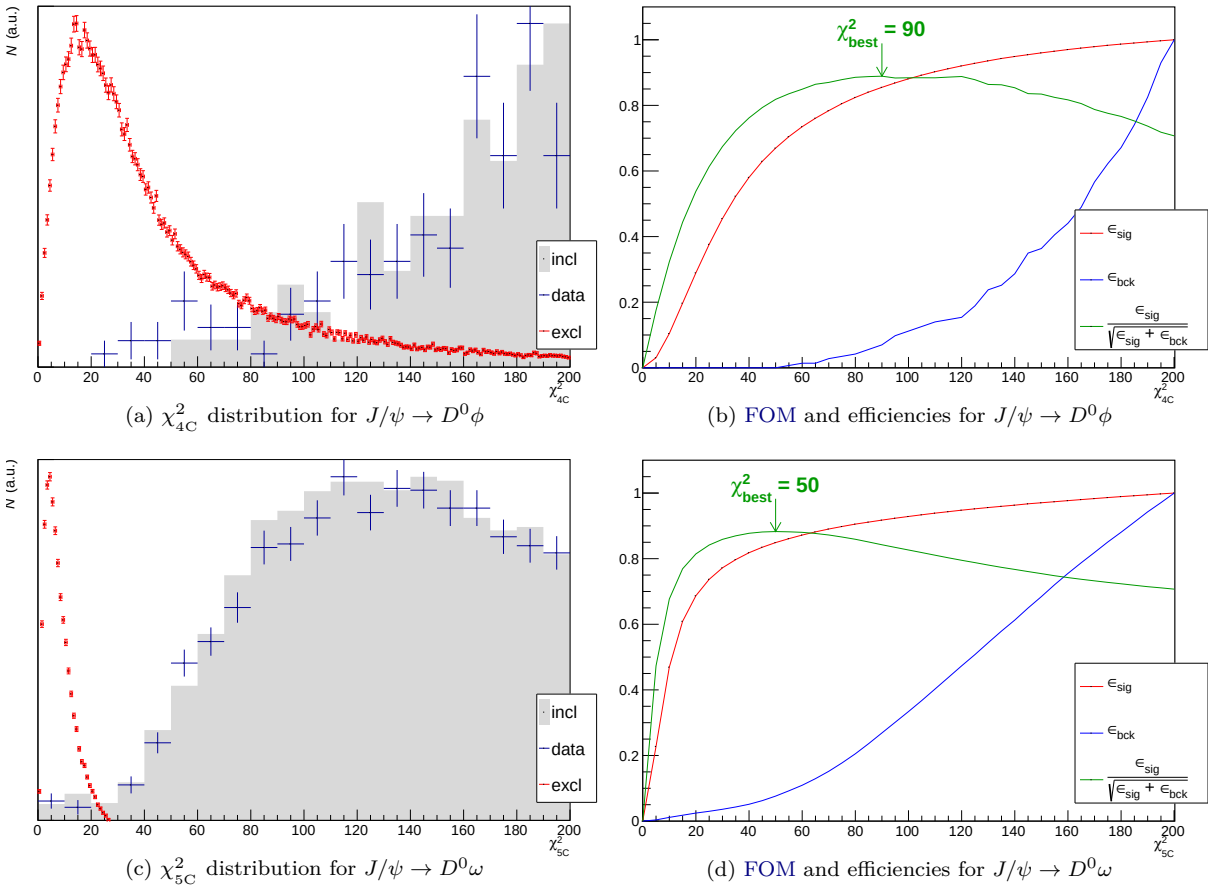

(a) χ^2_{4C} distribution for $J/\psi \to D^0\phi$

(b) FOM and efficiencies for $J/\psi \to D^0\phi$

(c) χ^2_{5C} distribution for $J/\psi \to D^0\omega$

(d) FOM and efficiencies for $J/\psi \to D^0\omega$

Figure 5.7: Optimisation of χ^2_{4C} and χ^2_{5C}.

5.3.2 Final cut flow

The cuts of the initial event selection listed in Table 4.4 with the mass window cuts and χ^2 cuts combined give us a *selection efficiency*. This is defined as the number of events that remain after applying all cuts in the signal MC divided by the number of events generated in the signal MC. A *cut flow* overview is given in Table 5.2. For $J/\psi \to D^0\phi$, the selection efficiency is 8.35% with 10 events remaining in measured data, for $J/\psi \to D^0\omega$ it is 7.48% with 587 events in data.

Cut	Events	Abs %	Rel %
All events	1,000,000	100	
0 net charge	475,390	47.5	47.5
4 charged tracks	346,150	34.6	72.8
2 K^-, K^+, π^-	238,030	23.8	68.8
Passed 4C-fit	100,170	10.0	98.9
Passed fit $\chi^2 < 90$	87,217	8.72	36.6
$1.85 < m_{D^0} < 1.89$ GeV	86,671	8.67	99.4
$1.00 < m_\phi < 1.04$ GeV	83,972	8.4	96.9
Both mass window cuts	83,483	**8.35**	99.4

(a) Final cut flow for $J/\psi \to D^0\phi$.

Cut	Events	Abs %	Rel %
All events	1,000,000	100	
0 net charge	600,250	60	60
4 charged tracks	543,090	54.3	90.5
K^-, π^-, 2 π^+	417,680	41.8	76.9
>2 photons	326,280	32.6	78.1
Passed 4C-fit	288,460	28.8	88.4
Passed 1C-fit	254,140	25.4	88.1
Passed fit $\chi^2 < 50$	182,017	18.2	71.6
Passed fit $\chi^2 < 25$	157,411	15.7	86.5
$M(\pi^-\pi^+) \notin [0.46, 0.52]$	114,224	11.4	72.6
$M(\pi^0\pi^+) \notin [0.46, 0.52]$	83,738	8.37	73.3
$M(\pi^0\pi^+) \notin [0.60, 0.90]$	79,530	7.95	95
$1.84 < m_{D^0} < 1.89$ GeV	78,604	7.86	98.8
$0.74 < m_\omega < 0.82$ GeV	75,619	7.56	96.2
Both mass window cuts	74,783	**7.48**	98.9

(b) Final cut flow for $J/\psi \to D^0\omega$.

Table 5.2: Cut flow tables for signal MC. Final selection efficiency is given in red.

We have also had a look at the topologies in inclusive MC after all cuts. These are given in Table 5.3. As can be seen, there are still many hadronic resonances, but it is almost impossible to cut these away, because most come from mis-identifications: a kaon is mistaken for a pion.

N_i	Decay channel	Decay products
6	$J/\psi \to \phi f_0(1790)$,	$\phi \to K^+K^-$, $f_0(1790) \to \pi^+\pi^-$
3	$J/\psi \to \pi^+\pi^-\phi$,	$\phi \to K^+K^-$
1	$J/\psi \to \phi f_2^{'}$,	$\phi \to K^+K^-$, $f_2^{'} \to K^+K^-$

(a) $J/\psi \to D^0\phi$.

N_i	Decay channel	Decay products
15	$J/\psi \to K^- K_1^{'+}$,	$K_1^{'+} \to \pi^0 K^{*+}$, $K^{*+} \to \pi^+ K^0$, $K^0 \to K_S^0$, $K_S^0 \to \pi^+\pi^-$
13	$J/\psi \to K^- K_1^+$,	$K_1^+ \to \pi^+ K^*$, $K^* \to \pi^0 K^0$, $K^0 \to K_S^0$, $K_S^0 \to \pi^+\pi^-$
10	$J/\psi \to \pi^0 K^- K^{*+}$,	$K^{*+} \to \pi^+ K^0$, $K^0 \to K_S^0$, $K_S^0 \to \pi^+\pi^-$
8	$J/\psi \to \pi^0 K^0 \bar{K}^*$,	$K^0 \to K_S^0$, $\bar{K}^* \to \pi^+ K^-$, $K_S^0 \to \pi^+\pi^-$
7	$J/\psi \to K^* K_2^{*0}$,	$K^* \to \pi^0 K^0$, $K_2^{*0} \to \pi^+ K^-$, $K^0 \to K_S^0$, $K_S^0 \to \pi^+\pi^-$
6	$J/\psi \to \pi^- b_1^+$,	$b_1^+ \to \pi^+\omega$, $\omega \to \pi^0\pi^+\pi^-$
6	$J/\psi \to \rho^+ K^0 K^-$,	$\rho^+ \to \pi^0\pi^+$, $K^0 \to K_S^0$, $K_S^0 \to \pi^+\pi^-$
5	$J/\psi \to \pi^+\pi^-\omega$,	$\omega \to \pi^0\pi^+\pi^-$
4	$J/\psi \to \pi^+ K^* K^-$,	$K^* \to \pi^0 K^0$, $K^0 \to K_S^0$, $K_S^0 \to \pi^+\pi^-$
4	$J/\psi \to K^{*+} K_2^{*-}$,	$K^{*+} \to \pi^+ K^0$, $K_2^{*-} \to \pi^0 K^-$, $K^0 \to K_S^0$, $K_S^0 \to \pi^+\pi^-$
2	$J/\psi \to K^- K_1^+$,	$K_1^+ \to \pi^+ K_0^0$, $K_0^0 \to \pi^0 K^0$, $K^0 \to K_S^0$, $K_S^0 \to \pi^+\pi^-$
...		(19 other decay channels ...)

(b) $J/\psi \to D^0\omega$.

Table 5.3: Topologies in signal region, taken from MC truth in inclusive MC.

5.4 Systematic uncertainties

The systematic uncertainties of this study have not yet been fully evaluated. This section attempts to set a *lower limit* on the systematic uncertainty, because it is required for the determination of the upper limit on the branching ratio, see σ_{sys} in Equation (5.15). In the following sections, we shortly go through the systematic uncertainties that we studied, but the list is still to be expanded in further studies (see Chapter 6). The final systematic uncertainty per channel is listed in Table 6.1 and is obtained by adding the components in quadrature. The systematic uncertainties will be evaluated during further studies using e.g. [82, 83].

Uncertainties in the intermediate BRs
The branching ratios of the decay channels that we use to reconstruct D^0, ϕ, ω, and π^0 are discussed in Section 4.2. See an overview in Table 5.4. We assume that these uncertainties are independent and add them in quadrature. This means:

$$\sqrt{0.04^2 + 0.5^2} = \mathbf{0.5}\% \quad \text{for} \quad J/\psi \to D^0\phi \tag{5.12}$$

$$\sqrt{0.04^2 + 0.6^2 + 0.034^2} = \mathbf{0.6}\% \quad \text{for} \quad J/\psi \to D^0\omega \tag{5.13}$$

Decay	BR (%)	Uncertainty (%)
$D^0 \to K^-\pi^+$	3.89	0.04
$\phi \to K^-K^+$	49.2	0.5
$\omega \to \pi^0\pi^-\pi^+$	89.3	0.6
$\pi \to \gamma\gamma$	98.823	0.034
$\mathcal{B}_{\text{inter}}$ for $J\psi \to D^0\phi$	1.91	0.5
$\mathcal{B}_{\text{inter}}$ for $J\psi \to D^0\omega$	3.43	0.6

Table 5.4: Overview of the intermediate branching ratios $\mathcal{B}_{\text{inter}}$. The total $\mathcal{B}_{\text{inter}}$ is computed as the product of the intermediate BRs, the total systematic uncertainty is obtained by adding in quadrature.

Uncertainties in mass window cuts
The systematic uncertainties on the mass window cuts originate from the difference in mass resolution between MC simulations and actual measured data. The systematic uncertainty on mass window cuts is therefore usually determined as:

$$\sigma = 1 - \epsilon_{\text{MC}}/\epsilon_{\text{data}} \tag{5.14}$$

where ϵ_{MC} is the selection efficiency of the inclusive MC and ϵ_{data} the selection efficiency of measured data.

For this study, we rely on systematic uncertainties determined by other studies. For ϕ, we follow [64], which studied a sample of $J/\psi \to \gamma\phi\phi, \phi \to K^+K^-$ and determined the systematic uncertainty to be 1.0%. In the same study, the systematic uncertainty on the $\gamma\gamma$ mass window cut was determined to be 0.2% by studying $J/\psi \to \rho^+\pi^-, \rho^+ \to \pi^0\pi^+, \pi^0 \to \gamma\gamma$ without kinematic fit. Procedures to study these channels were comparable to this study, however, the data sets used were only those of 2009 (see Table 4.6), which means that the systematic uncertainties in this study can probably be pushed down further. The systematic uncertainty on the mass window cut of ω has not yet been computed.

Uncertainties in MDC tracking efficiency
The MDC tracking efficiency has been studied for many BESIII studies. This is usually done by investigating a clean channel like $J/\psi \to \rho\pi \to \pi^0\pi^-\pi^+$, see for instance [84]. The systematic uncertainty is 1.0% for each charged track. In our case, this means **4.0%** for both investigated decay channels.

Uncertainties in Particle Identification
Systematic uncertainties in PID have also been studied extensively in BESIII. For pions by studing $J/\psi \to p\bar{p}\pi^+\pi^-$ events and for kaons with the use of $J/\psi \to K^0_S K^+\pi^-$ events. The PID efficiencies for measured data agree with inclusive MC simulations within 1.0% for each charged particle type, so the systematic uncertainty on PID is taken to be **4.0%** for both $J/\psi \to D^0\phi$ and $J/\psi \to D^0\omega$.

Uncertainties in photon detection
This type of systematic uncertainty has also been studied extensively in other BESIII studies, usually from photon conversion via $e^+e^- \to \gamma\gamma$, see e.g. [85]. It is determined as 1.0% per photon, which in our case means **2.0%** for $J/\psi \to D^0\omega$.

Uncertainty from 1C fit (π^0 resonance)
The additional constraint applied to the kinematic Kalman fit for the $J/\psi \to D^0\omega$ channel also results in an uncertainty for the π^0 resonance. This uncertainty has not been fully studied yet, but it can be done by comparing $J/\psi \to \rho^+\pi^-, \rho^+ \to \pi^0\pi^+, \pi^0 \to \gamma\gamma$, first with a 4C fit only, then with 5C fit using Equation (5.14).

Uncertainty	Channel $D^0\phi$ (%)	Channel $D^0\omega$ (%)
Intermediate BRs	0.5	0.6
ϕ/ω mass window	1.0	
MDC tracking	4.0	4.0
Particle ID	4.0	4.0
Number of J/ψ events	0.53	0.53
4C kinematic fit		
MC statistics		
Photon detection		2.0
π^0 mass window		0.2
π^0 kinematic fit (1C)		
K^+, K^0_S, ρ^+ windows		
Total σ_{sys}	5.8	6.1

Table 5.5: Summary table of systematic errors for $J/\psi \to D^0\phi, D^0\omega$. Highlighted in yellow are uncertainties that are still to be computed.

Uncertainty in total number of J/ψ events
The total number of J/ψ events from the 2018 data sets has not yet been fully evaluated. Therefore, we make use of the uncertainty that has been computed for the 2009 and 2012 data set. The number of J/ψ events was established to be $N_{J/\psi} = (1310.6 \pm 7.0) \times 10^6$ [70], which is $7.0/1310.6 = \mathbf{0.53}\%$. The systematic uncertainty for the 2018 data sets will probably be lower due to larger statistics (see trend in Table 4.6), so we take this value as a conservative estimate for the full data set.

Fit-related uncertainties
In Section 5.5, we will see that the determination of N_{UL} relies on maximum likelihood fits of invariant mass distributions with a PDF. This introduces additional uncertainties, but these have not yet been evaluated. The procedure would be to use different fit range with the same model and different background models (e.g. different orders of the Chebychev polynomial). This may also result in higher values of N_{UL}, in which case the highest value of N_{UL} should be used.

5.5 Determination of upper limit

Finally, we are in a position to compute the upper limit. This computation consists of two parts: (1) compute the upper limit N_{UL} on the number of candidate $J/\psi \to D^0\phi, D^0\omega$ events and (2) use this number, the selection efficiency, and the number of J/ψ events to establish an upper limit on the branching ratio. The latter is easy to compute using:

$$\mathcal{B} < \frac{N_{\text{UL}}}{\epsilon N_{J/\psi} \mathcal{B}_{\text{inter}} (1 - \sigma_{\text{sys}})} \tag{5.15}$$

where $N_{J/\psi}$ is the number of J/ψ events, $\mathcal{B}_{\text{inter}}$ is the product of the branching ratios of the intermediate decay channels (see Table 5.4) and σ_{sys} is the total systematic uncertainty. The result is discussed in Section 6.

The computation of N_{UL} is far more complicated. In fact, there isn't complete consensus about the right approach, as it depends on whether you prefer a *Bayesian* or *frequentist* approach, particularly when working with small statistics [86]. In an attempt to bridge both philosophical views, physicists at LEP developed the Confidence Level (CL_s) technique, where s stands for signal [87]. In this study, we chose to follow the CL_s method.

To compute N_{UL}, we use a series of binned extended minimum likelihood fits [81]. In Figure 5.8, we can see the mass distributions of the events that are left after all initial and final event selection cuts. The distribution in the complete available space is given on the left for reference; the right figures magnifies the region in which we are interested. Indicated in red are the mass window cuts that we determined in Table 5.1. For comparison, the distributions for the exclusive MC are given in Figures 5.8e and 5.8f.

The number of signal events N_s is determined from the 1-dimensional projection of the distributions in Figure 5.8 on their $M(K^-\pi^+)$ (D^0) axis, with the determined mass window cut applied to the mass window of the tag meson ($1.00 < M(K^-K^+) < 1.04$ GeV/c^2 for ϕ, $0.74 < M(\pi^0\pi^-\pi^+) < 0.82$ GeV/c^2 for ω). The same procedure can also be applied to the $M(K^-K^+)$ resp. $M(\pi^0\pi^-\pi^+)$ distributions with a cut on $M(K^-\pi^+)$ of the D meson.

The upper limit N_{UL} is determined from these 1-dimensional distributions. We apply a fit to this distribution (see Figures 5.9a and 5.10a on pp. 42–43). All fit parameters are then set to constant but for N_{B}. The N_{S} is then varied over a certain range of interest and for each value of N_{S}, we compute the likelihood L of the new fit. The resulting L versus N_{S} distribution is called a *likelihood scan*.

The likelihood scan distribution has a Gaussian-like shape and can be integrated. We now define upper limit $N_{\text{UL}}(\text{CL})$ for some Confidence Level (CL) as:

$$\frac{\int_0^{N_{\text{UL}}(\text{CL})} L(N)dN}{\int_0^{\infty} L(N)dN} = \text{CL} \tag{5.16}$$

Since L is usually so large that it cannot be evaluated with floating point values, we work with $\log(L)$, shift the resulting distribution of $\log(L)$ versus N_{S} so that $\log(L) = 0$ when $N_{\text{S}} = 0$, and take the exponential of the shifted $\log(L)$ values. Because Equation (5.16) uses a normalisation factor, this procedure does not affect N_{UL}.

It should be noted that N_{S} is allowed to be negative. This is counter-intuitive, but the framework used to fit the PDFs is `MINUIT`, which does not work well at boundaries of a fit parameter range, i.e. around 0 if we restrict N_{S} to be positive. The upper limit determination takes care of apparent anomaly, because Equation (5.16) only integrates over $N > 0$.

In this study, we use a 90% Confidence Level. The resulting values of $N_{\text{UL}}(\text{CL} = 90\%)$ — namely, $N_{\text{UL}} = 5.2$ for $J/\psi \to D^0\phi$ and $N_{\text{UL}} = 50$ for $J/\psi \to D^0\omega$ — are given in Table 5.6 along with the chose PDFs for the background components.[2] We decided to use the value of $N_{\text{UL}}(\text{CL} = 90\%)$ coming from the projection on the $M(K^-\pi^+)$ axis, because the D^0 is highly suppressed in J/ψ decays, while the tag mesons ϕ and ω exist in many J/ψ decays and, as we saw in Table 5.3, do result in noise within their respective signal regions. Table 5.6 does, however, list their $N_{\text{UL}}(\text{CL} = 90\%)$ as well for comparison. The table also shows $N_{\text{UL}}(\text{CL} = 90\%)$ determined from inclusive MC, to show that a distribution of which we know that it does not have any signal does result in comparable upper limits.

	Distribution	**Data**	**Background PDF**	N_{S}	N_{UL}
$D^0\phi$	$M(K^-\pi^+)$	data	1st ord. Chebychev	0.96	**5.2**
	$M(K^-K^+)$	data	Special Argus	7.3	13
	$M(K^-\pi^+)$	incl MC	1st ord. Chebychev	2.3	6.2
	$M(K^-K^+)$	incl MC	Special Argus	5.0	9.4
$D^0\omega$	$M(K^-\pi^+)$	data	2st ord. Chebychev	33	**50**
	$M(\pi^0\pi^-\pi^+)$	data	2st ord. Chebychev + Voigtian	9.4	36
	$M(K^-\pi^+)$	incl MC	2st ord. Chebychev	3.4	12
	$M(\pi^0\pi^-\pi^+)$	incl MC	2st ord. Chebychev + Voigtian	−4.7	11

Table 5.6: Results of the likelihood scan. The two values red values are used in the determination of the upper limit on the branching ratios. For comparison, N_{UL} of the inclusive MC and for the tag mesons are also given.

[2] For $M(\pi^0\pi^-\pi^+)$ (ω), there is still a contribution from the 'shifted ω peak', see Section 5.2.2. This is characterised with a Voigtian added to the background.

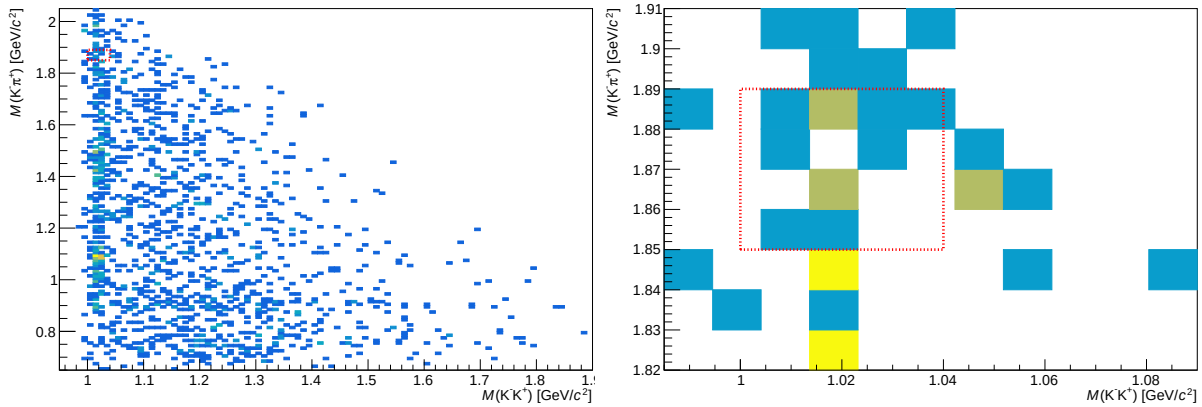

(a) Complete space $J/\psi \to D^0\phi$

(b) Signal region $J/\psi \to D^0\phi$

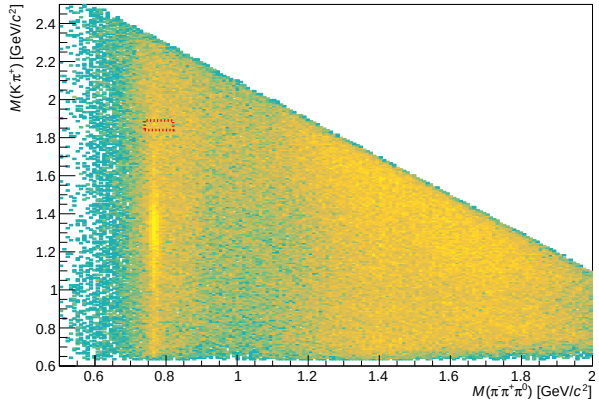

(c) Complete space $J/\psi \to D^0\omega$

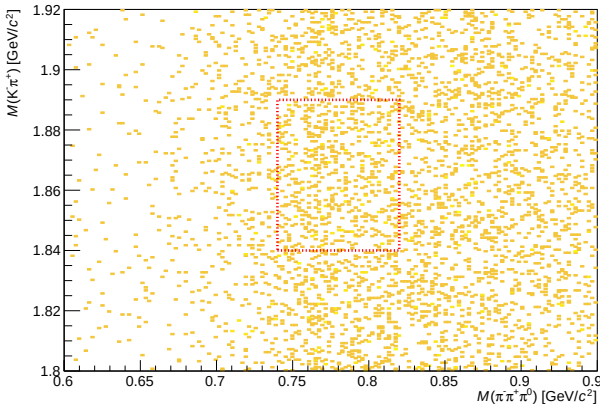

(d) Signal region $J/\psi \to D^0\omega$

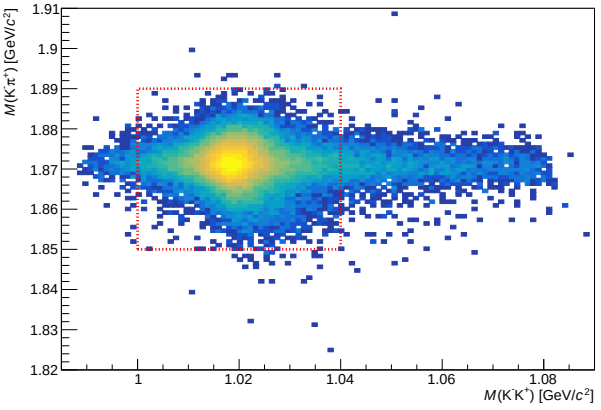

(e) $J/\psi \to D^0\phi$

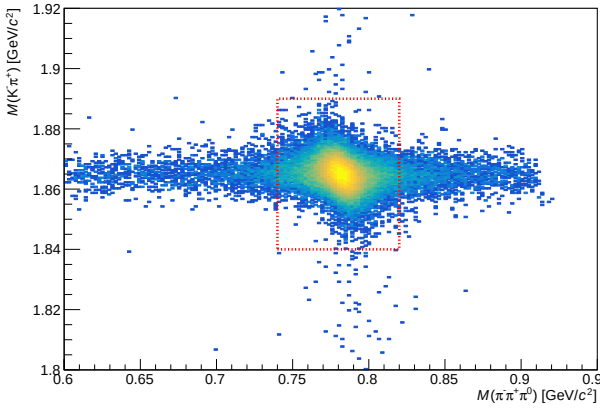

(f) $J/\psi \to D^0\omega$

Figure 5.8: Final invariant mass distributions for measured data. The signal region is indicated in red.

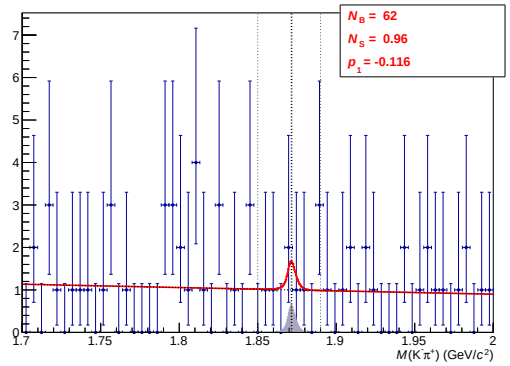

(a) Data fit for D^0; bin width: 10 MeV/c^2.

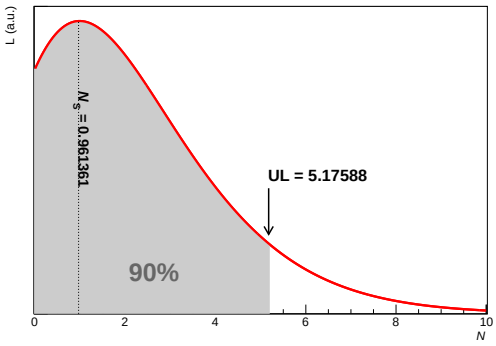

(b) Data likelihood scan for D^0.

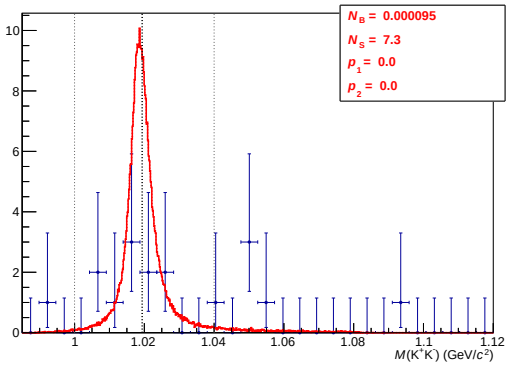

(c) Data fit for ϕ; bin width: 5 MeV/c^2.

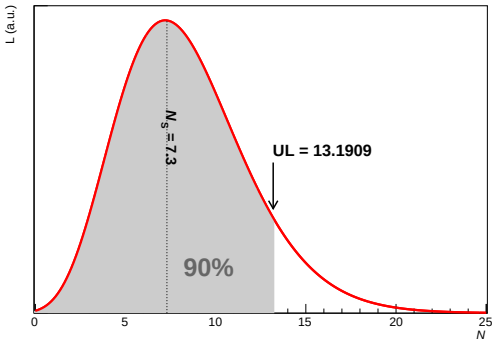

(d) Data likelihood scan for ϕ.

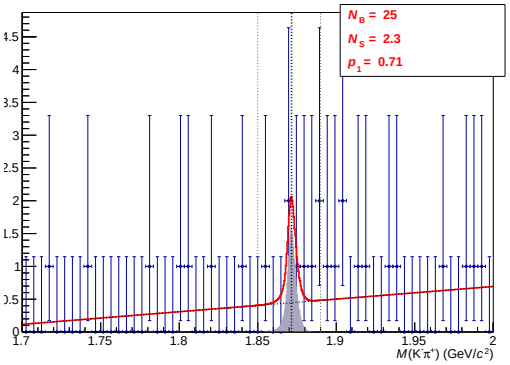

(e) Incl. MC fit for D^0; bin width: 10 MeV/c^2.

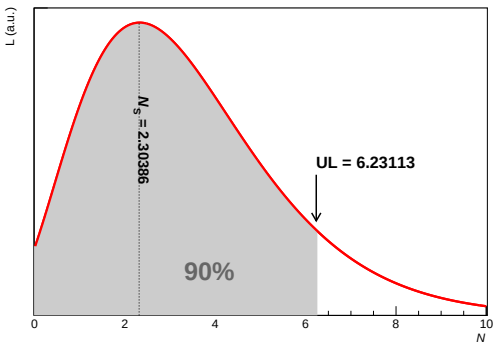

(f) Incl. MC likelihood scan for D^0.

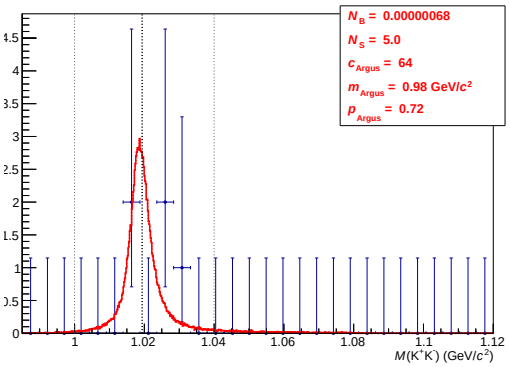

(g) Incl. MC fit for ϕ; bin width: 5 MeV/c^2.

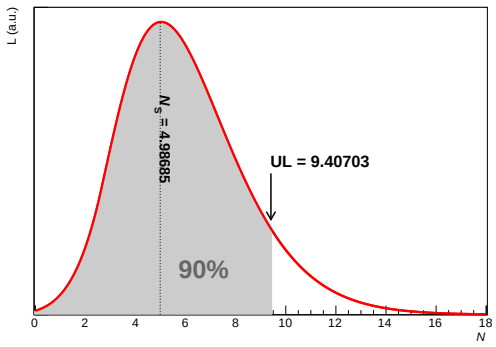

(h) Incl. MC likelihood scan for ϕ.

Figure 5.9: Final fit and likelihood scan of $J/\psi \to D^0\phi$. The upper limit of D^0 in 5.9b will be used, the others are given for comparison only.

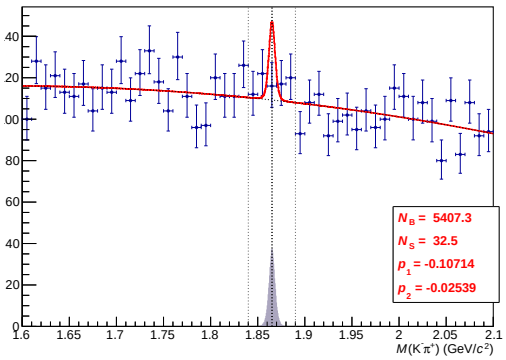

(a) Data fit for D^0; bin width: 10 MeV/c^2.

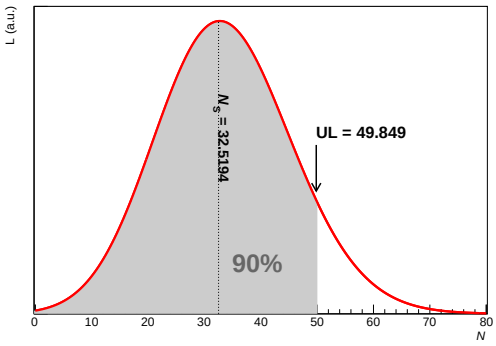

(b) Data likelihood scan for D^0.

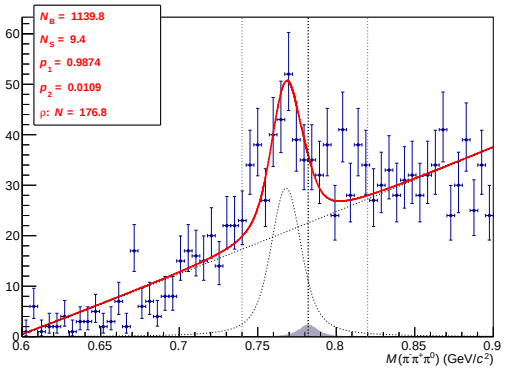

(c) Data fit for ω; bin width: 5 MeV/c^2.

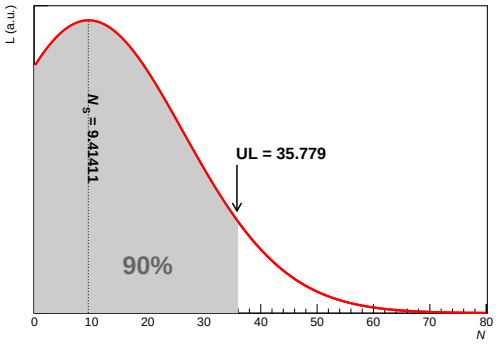

(d) Data likelihood scan for ω.

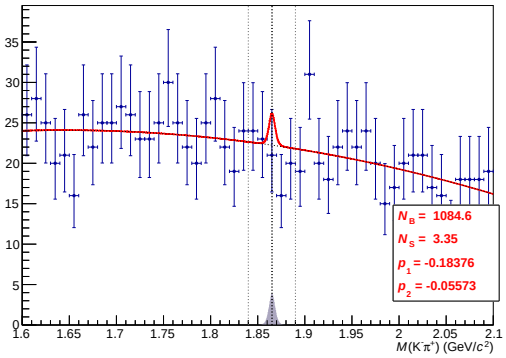

(e) Incl. MC fit for D^0; bin width: 10 MeV/c^2.

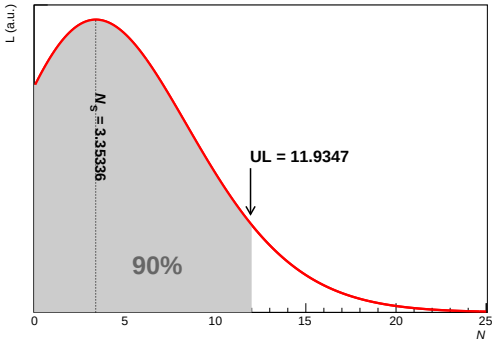

(f) Incl. MC likelihood scan for D^0.

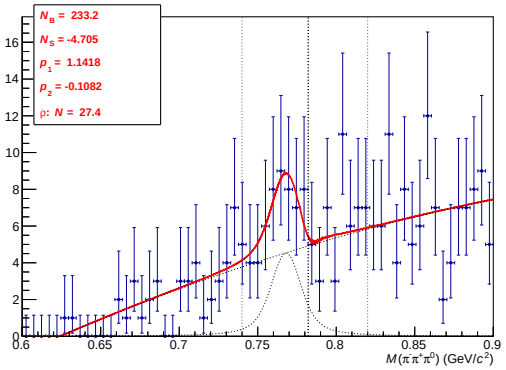

(g) Incl. MC fit for ω; bin width: 5 MeV/c^2.

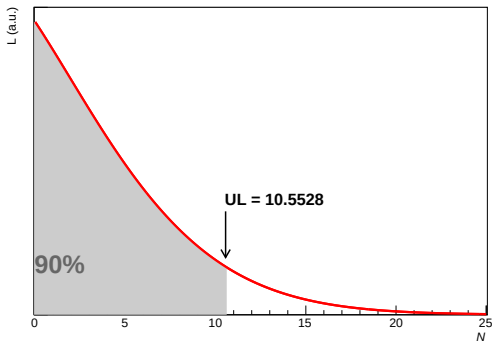

(h) Incl. MC likelihood scan for ω.

Figure 5.10: Final fit and likelihood scan of $J/\psi \to D^0\omega$. The upper limit of D^0 in 5.10b will be used, the others are given for comparison only

Chapter 6

Conclusion & Discussion

No excess of $J/\psi \to D^0\phi$ or $J/\psi \to D^0\phi$ has been observed in the 10×10^9 J/ψ events collected by BESIII. At the 90% Confidence Level we have determined the upper limit of the branching ratios of these two decay channels to be $\mathcal{B}(J/\psi \to D^0\phi) < 3.4 \times 10^{-7}$ with at least 5.8% systematic uncertainty and $\mathcal{B}(J/\psi \to D^0\omega) < 2.1 \times 10^{-6}$ with at least 6.1% systematic uncertainty.[1] An overview is given in Table 6.1.

As discussed in Section 4.1, the computed branching ratios are still consistent with the predictions of the SM (around 10^{-10}). The new upper limit excludes NP models that predict branching ratios of around 10^{-6}. Theoretical papers that investigated these new models do not, however, result in rough BR estimates only and have become outdated: the only computation using NP models performed for $J/\psi \to DP, DV$ decays specifically is [48].[2] This suggests that new theoretical computations need to be done in order to make conclusions about specific NP models.

Decay channel	$J/\psi \to D^0\phi$	$J/\psi \to D^0\omega$
Efficiency ϵ	8.35%	7.48%
$\mathcal{B}_{\text{inter}}$	1.91%	3.43%
N_{UL} 90% C.L. (count)	5.2 (10)	40 (587)
Total σ_{sys}	$> 5.8\%$	$> 6.1\%$
Upper limit $\mathcal{B}$	$\mathbf{> 3.4 \times 10^{-7}}$	$\mathbf{> 2.1 \times 10^{-6}}$

Table 6.1: Determination of upper limit of the branching ratios.

As can be seen from Equation (5.15), the largest factor to the upper limit of the branching fraction is the number of $N_{J/\psi}$. For this study, a data set of 10^{10} events was used, around 50 times more J/ψ events than used in the latest two $J/\psi \to DP, DV$ studies. However, comparing with the upper limits found in previous studies, summarised in Table 4.1, we can see that this is not the case. This suggests that the branching ratio can be further pushed down, perhaps even below the estimated sensitivity of around 10^{-7}. Some suggestions:

- Use other decay channels to reconstruct D^0. Here, we have to balance larger hadronic backgrounds versus higher intermediate BRs, see Table 4.2. The semileptonic decay channel $D^0 \to K^- e^+ \nu_e$ has a intermediate BR similar to the one used for this study ($D^0 \to K^-\pi^+$), but will result in a smaller hadronic combinatorial background, which particularly affects the $J/\psi \to D^0\omega$ analysis. Another option would be to look into $D^0 \to K^-\pi^+\pi^0$ with BR $= (14.2 \pm 0.5)\%$ and $D^0 \to K^-\pi^+\pi^+\pi^-$ with BR $= (8.11 \pm 0.15)\%$, although the double π^0 in the case of $D^0\omega$ may make matters worse. Still, ignoring background for now, this may result in an improvement of a factor 4, see Equation (5.15) as it affects both ϵ and $\mathcal{B}_{\text{inter}}$.
- It would be ideal to combine different reconstruction methods to approach an *inclusive reconstruction*. New techniques will have to be developed for this as it has not been attempted in previous

[1] These figures can *not* be quoted yet.
[2] Worse, this study investigates $c \to u l^+ l^-$ (semileptonic) and $c \to u$ transitions only.

studies. Computation of systematic uncertainties will be particularly complicated due to the varying widths of the D^0 decay channels.

Another great improvement in the determination of N_{UL} would be to use a 2-dimensional fit. At the moment, the projection on the axis of the invariant mass distribution of either the D meson or the tag meson results in additional systematic uncertainties from the mass cut applied to the other axis. In addition, other resonances or background structures nearby, such as the 'shifted ω peak' could result in a higher upper limit. This could be improved by using for instance the distribution of Figure 5.8f as a signal PDF to fit to the distribution in Figure 5.8d.

Finally, the framework developed for this study has been written in a user-friendly way and can be easily modified for other decay channels and reconstruction methods. In this way, decay channels with higher sensitivity and higher predicted branching ratios listed in Table 4.1 can be revisited with the newest BESIII data sets at hand (see Section A).

This study was performed within the time available for a master's research (one year), most of which required getting to know techniques and analysis code used in the BESIII Collaboration. The upper limits presented here therefore need further investigation, still have to go through the BESIII review process, and can therefore not yet be cited.

This study has not been performed in a blind-analysis set-up. The reason is that the fit model is simple: the signal model is that of the exclusive MC, while the background PDF is either the Argus shape or a Chebychev polynomial. This means that there is only one parameter that influences N_{UL} (the scaling of the signal MC) so there is little room for introducing bias.

The simplicity of the model would, however, allow for a blind analysis, starting by applying it to a smaller inclusive MC sample, then applying for access to the real data set. Within a larger time frame, this approach can therefore easily be adopted when (re-)studying the other branching ratios.

Appendix A

Analysis code

As is apparent from Section 4.1, the decays $J/\psi \to D^0\phi, D^0\omega$ fall in the category of rare, weak $J/\psi \to DM$ decays. These decays are comparable in form and therefore lend themselves to standardised code. The code of previous studies, however, has not been written in such a way that it can be easily applied to other decay channels.

Much time of this research project was therefore spend on designing user-friendly code that is easily adopted for another $J/\psi \to DM$ decay study. This led to several spin-off projects (see Section B) that have a wider application, but also two frameworks that can be used in future studies: one for initial event selection, one for final event selection and analysis. Initially, the analysis code was published on GitHub (github.com). In September 2019, IHEP created its own GitLab (code.ihep.ac.cn) to which the code is currently being migrated. See Table A.1 for an overview (note: IHEP's GitLab is behind a login).

Initial event selection takes place on the server using BOSS. Since BOSS is built on outdated libraries and old code management principles (see Section 3.5), it turned out to be difficult to design a package that allows for a general approach to event selection. An attempt was made in the form of `BOSS_IniSelect`. This framework first makes a selection of neutral and charged tracks and identified particles with its `TrackSelector` package. The user can then use these selections in a specialised event selection that inherits from the `TrackSelector` algorithm. The aim is to standardise and to simplify initial event selection code. Documentation is provided with the repository.

It turned out that the `BOSS_IniSelect` was overly ambitious for a one year's project. As a final resort, the analysis was therefore migrated to a less general framework that was nonetheless highly modulated. This is the `BOSS_JpsiToDPV` framework. Here, the idea is to have one major algorithm run over the data, with sub-algorithms (specified by the user) identifying specific $J/\psi \to DM$ channels. Most computation time in initial event selection is lost in looping over the reconstructed data set, not in computing for instance a kinematic fit. $J/\psi \to DM$ decays are rare, which means that a lot of time is lost on processing uninteresting events (here, it could also be interesting to look into BOSS's *tag based analysis* tools). A major advantage of `BOSS_JpsiToDPV` set-up is therefore that many channels are analysed at the same time, eliminating the need to run several jobs over the same data set. Another advantage is standardisation of the code: if changes are made to the overarching algorithm (such as implementing new `NTuples`), these changes apply to all decay channels.

Finally, the `BOSS_Afterburner` takes care of the final event selection and, more importantly, computing aspects like cut flow, PDF fits and likelihood scans. The `BOSS_Afterburner` follows the structure of the `CppStarterKit` (see Section B) in that it is a formal object-oriented framework containing scripts/executables (standardised analysis procedures) that process YAML configuration files (containing analysis-specific parameters). Tools that are commonly used by several scripts are bundled as classes. Extensive documentation is contained within the repository.

Local physics analysis if often written in long C scripts with hard-coded parameters, such as fit ranges. The consequence is that much time is lost in re-compiling every time a parameter is modified, let alone that code becomes unreadable to outsiders.[1] The `BOSS_Afterburner` overcomes this with the use of configuration files that are loaded at run-time. In addition, the fact that the code is modulated through different classes reduces compilation time whenever the code itself is changed, but it still retains

[1] A recent trend is to overcome this with uncompiled (but less efficient) programming languages such as Python.

the efficiency of C++.

A major example is the `RooFitBuilder`. This is a `RooFit` wrapper that builds RooFit objects from YAML files as input. It allows a user to quickly build a PDF from `RooFit`'s stock functions by summing or convoluting them. Fit parameters and ranges can also be continuously optimised without having to recompile the framework, reducing the total analysis time to a few seconds. The plan is to develop more tools and to combine the scripts into a single executable that can do a complete final event selection plus analysis in one go. This would be a great improvement to making analyses reproducible and will in general speed up high-energy physics analysis.

Name	**IHEP GitLab**	**GitHub**
BOSS_IniSelect	redeboer/IniSelect	redeboer/BOSS_IniSelect
BOSS_JpsiToDPV	redeboer/BOSS_JpsiToDPV	
(config files)	redeboer/JpsiToDPV_config	
BOSS_Afterburner	redeboer/BOSS_Afterburner	redeboer/BOSS_Afterburner

Table A.1: Overview of code repositories specific to $J/\psi \to DM$ decays. The full URL can be obtained from the right two columns by adding `http://code.ihep.ac.cn/` and `https://github.com/`, respectively. Note that IHEP's GitLab is behind an SSO login.

Appendix B

Spin-off projects

During this research project, it was found that many pf the code development practices in BESIII have become rather outdated. The main software framework, BOSS, is for instance still maintained through Concurrent Versions System (CVS), while much of its documentation has not been updated for over a decade. This led to several spin-off projects that can be divided into three categories: (1) suggestions for policy changes, (2) development of new documentation platforms, and (3) Git repositories for general use in the BESIII Collaboration.

B.1 Documentation and Policy

Most BOSS documentation is hosted through WikiMedia on [68] (behind SSO login). However, since many of the pages there are outdated, instructions are usually passed in person-to-person conversations.

Initially started as a collection of notes gathered from such conversations, the BOSS GitBook (besiii.gitbook.io/boss) was therefore set up for this research project to provide an overview of analysis tools and guidelines for BESIII. The pages currently focus mainly on light hadron analyses, but it is the aim to expand these pages to other groups as well through contributions in the underlying Git repository.

The attempt at improving documentation led to a larger report written in collaboration with the Software Performance Group. This "Roadmap for better documentation and code collaboration in BESIII" [88] was inspired by recent debates in the HEP community [89, 90, 91, 92, 93, 94, 95] and has been presented during the BESIII summer collaboration meeting at Fudan University. Since September 2019, IHEP now hosts a GitLab and BESIII is considering to migrate BOSS to from CVS to Git.

Name	IHEP GitLab	GitHub
CppStarterKit	bes3/StarterKit	redeboer/StarterKit
BOSS_StarterKit	bes3/BOSS_StarterKit	redeboer/BOSS_StarterKit
BOSS_Tutorials	bes3/BOSS_Tutorials	redeboer/BOSS_Tutorials
BOSS_JobSubmitter	bes3/BOSS_JobSubmitter	redeboer/BOSS_JobSubmitter
BOSS_ExternalLibs	bes3/BOSS_ExternalLibs	redeboer/BOSS_ExternalLibs
BOSS	bes3/BOSS	

Table B.1: Overview of code repositories designed for general use. The full URL can be obtained from the right two columns by adding `http://code.ihep.ac.cn/` and *https://github.com/*, respectively. Note that IHEP's GitLab is behind an SSO login, but the `CppStarterKit` has been made public. All repositories come with documentation.

B.2 Git repositories for BESIII

Several repositories were developed for this $J/\psi \to DM$ study (see Appendix A). Components that are useful to other BESIII as well have been extracted and made available as Git repositories. Again, there is a distinction between initial event selection (which relies on BOSS) and final event selection (which is usually performed locally). An overview of these repositories is given in Table B.1.

B.2.1 For the BESIII Offline Software System

To use BOSS, users have to set up a certain environment on IHEP's `lxslc` farm. This is a process that is particularly painful for beginners, even though it can easily be automatised. This process has been automatised within the `BOSS_StarterKit`.

The `BOSS_StarterKit` also contained several other tools, most of which come as Git submodules. An example is the `BOSS_JobSubmitter`, a framework that attempts to simplify the procedure for writing job files that are required when submitting an initial event selection algorithm to the computation queue of `lxslc` (`hep_sub`).

The `BOSS_StarterKit` is to be expanded with further BOSS packages in the form of submodules. An example is the `BOSS_Tutorials`, which attempts to split up commonly used example code such as `RhopiAlg` into shorter procedures. The problems with the original example packages is that they are several hundred lines of code without much explanation, making it difficult to distinguish the several procedures that they perform. The packages contained in `BOSS_Tutorials` also can serve as unit tests in case BOSS updates come out.

Users can develop their own initial event selections and embed them within the `BOSS_StarterKit` to make use of the functionality of all its submodules.

Since IHEP created a GitLab, attempts have also been made to build BOSS outside the SLC environment. While BOSS's reliance on older compilers and external libraries has made this process difficult so far, it resulted in a repository that contains the entire source code of each version of BOSS (code.ihep.ac.cn/bes3/BOSS). In addition, to facilitate autocomplete in code editors such as Visual Studio Code, all headers for BOSS version 7.0.4 and all its external libraries have been collected in the `BOSS_ExternalLibs` repository. One of the aims is to facilitate in an eventual BOSS migration to Git.

B.2.2 For local analysis

As discussed in Appendix A, the `BOSS_Afterburner` was developed to standardise final event selection and improve the speed of for instance PDF fitting. Compilation is done through of a `Makefile` framework that was written in a very general style, enabling users to implement a completely different file organisation (sub-folders are for instance also compiled).

This `Makefile` framework, along with components necessary for processing YAML configuration files, have been extracted to a template repository: the C++ Starter Kit (`CppStarterKit`). The aim of this starter kit is to help users set up a `make` framework that compiles classes ('`include`') and `scripts` and to facilitate extracting parameters to YAML configuration files ('`config`'), so that they can be loaded at runtime and modified any time without affecting the framework.

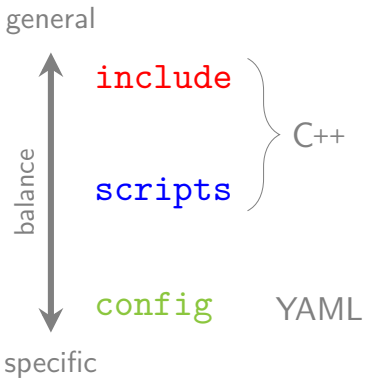

Figure B.1: Balance between the three main ingredients of the `CppStarterKit`.

In HEP analyses, C++ is often merely used in the form of a long script without much modulation (functions and classes), other than making use of CERN's ROOT libraries. The `CppStarterKit` helps users get beyond that level. Users can initially start writing a traditional script under `script`, but can then extract more general classes and functions and move them to `include`. Parameters that are specific to the analysis can be extracted to `config` files that are loaded at runtime. In this way the user can decide on her/his own balance between more general objects, standardised scripts, and specifics in configuration files (see Figure B.1).

The entire set-up is not revolutionary, but encapsulates standard practices in software development. The aim of the framework is merely to encourage these practices to more programmers of the HEP community.

Appendix C

Common abbreviations

2HDM	Two-Higgs-Doublet Model
ALICE	A Large Ion Collider Experiment [link]
ARGUS	A Russian-German-United States-Swedish Collaboration
BEMS	Beam Energy Measurement System of the BEPC
BEPC	Beijing Electron–Positron Collider [link]
BES	Beijing Electron Spectrometer [link]
BNL	Brookhaven National Laboratory [link]
BOOST	BESIII Object Oriented Simulation Tool
BOSS	BESIII Offline Software System [link]
BR	Branching Ratio, also denoted $\mathcal{B}$(<decay channel>)
BSC	Barrel Shower Counter, a substystem of BESI and BESII
BSM	Beyond the Standard Model, a collective term for New Physics theories
BW	Breit-Wigner PDF
CAS	Chinese Academy of Sciences [link]
CDC	Central Drift Chamber, a substystem of BESI and BESII
CEPC	Circular Electron-Positron Collider [link]
CERN	Conseil Européen pour la Recherche Nucléaire, or "European Organization for Nuclear Research" in Geneva, Switzerland [link]
CGEM-IT	Cylindrical Gas Electron-Multiplier Inner Tracker
CKM-matrix	Cabibbo-Kobayashi-Maskawa quark mixing matrix
CLT	Central Limit Theorem
CL	Confidence Level, a statistical term
CL$_s$	Confidence Level technique, see Section 5.5
CMT	Configuration Management Tool [link]
CM	Centre-of-Mass

CQM	Constituent Quark Model
CSNS	China Spallation Neutron Source [link]
CVS	Concurrent Versions System [link], a predecessor or SVN and Git
DAQ	Data Acquisition
DESY	Deutsches Elektronen-Synchrotron, or "German Electron Synchrotron" [link]
DORIS	Doppel-Ring-Speicher, or "Double-Ring Storage", at DESY with its ARGUS detector
EMC	Electromagnetic Calorimeter
ESC	End cap Shower Counter, a substystem of BESI and BESII
FCC	CERN's Future Circular Collider [link]
FOM	Figure-Of-Merit, a measure used to optimise cuts
GDML	Geometry Design Mark-up Language
GEANT	GEometry ANd Tracking, a toolkit for simulating the passage of particles through matter, developed by CERN
HEPS	High Energy Photon Source [link]
HEP	High Energy Physics
IHEP	Institute of High Energy Physics [link]
IP	Interaction Point, see also IR
IR	Interaction Region, see also IP
ISR	Initial State Radiation
JCCHEP	Joint Committee on Cooperation in High Energy Physics
JUNO	Jiangmen Underground Neutrino Observatory [link]
L1	Level 1 trigger, the BESIII *hardware* trigger
L3	Level 3 trigger, the BESIII *software* trigger
LEP	Large Electron–Positron Collider
LHAASO	Large High Altitude Air Shower Observatory [link]
LHC	CERN's Large Hadron Collider [link]
LQCD	Lattice Quantum Chromo-Dynamics
MC	Monte Carlo, referring to simulation of collisions
MDC	Multilayer Drift Chamber
MSSM	Minimal Super-symmetric Standard Model
MUC	Muon Chamber System
NP	New Physics, any theory or research that attempts to extend the SM
DCA	Distance of Closest Approach to the IP
PDF	Probability Density Function

PDG	Particle Data Group [link], commonly used as a shorthand for [11]
PID	Particle Identification
PMT	Photo-Multiplier Tube
PWA	Partial Wave Analysis
QCD	Quantum Chromo-Dynamics
QED	Quantum Electrodynamics
QFT	Quantum Field Theory
QGP	Quark-Gluon Plasma
RF	Radio Frequency
RPC	Resistive Plate Chamber
SAP	Institute for Subatomic Physics [link] of Utrecht University
SCQ	Solenoid Coil Quadrupole
SC	Solenoid Coil
SLAC	Stanford Linear Accelerator Center [link]
SLC	Scientific Linux CERN [link]
SM	Standard Model
SPEAR	Stanford Positron Electron Asymmetric Rings with its MARK detectors [link]
SPS	Super Proton Synchrotron
SSM	Superconducting Solenoid Magnet
SSO	Single Sign-On environment
SVN	Apache Subversion [link], a version control system
TDC	Time-to-Digital Converter, used in the EMC
TOF	Time-Of-Flight system
`lxslc`	'Linux Scientific Linux CERN', a jargon term for the IHEP farm on which analysis jobs are run

Bibliography

[1] G. Aad *et al.*, "Observation of a new particle in the search for the Standard Model Higgs boson with the ATLAS detector at the LHC," *Physics Letters B*, vol. 716, no. 1, pp. 1–29, Sep. 2012. https://linkinghub.elsevier.com/retrieve/pii/S037026931200857X

[2] S. Chatrchyan *et al.*, "Observation of a new boson at a mass of 125 GeV with the CMS experiment at the LHC," *Physics Letters B*, vol. 716, no. 1, pp. 30–61, Sep. 2012. https://linkinghub.elsevier.com/retrieve/pii/S0370269312008581

[3] M. Ablikim *et al.*, "Observation of a Charged Charmoniumlike Structure in $e^+e^- \to \pi^+\pi^- J/\psi$ at $\sqrt{s}$=4.26 GeV," *Physical Review Letters*, vol. 110, no. 25, Jun. 2013. https://link.aps.org/doi/10.1103/PhysRevLett.110.252001

[4] ——, "Observation of a Charged Charmoniumlike Structure $Z_c(4020)$ and Search for the $Z_c(3900)$ in $e^+e^- \to \pi^+\pi^- h_c$," *Physical Review Letters*, vol. 111, no. 24, Dec. 2013. https://link.aps.org/doi/10.1103/PhysRevLett.111.242001

[5] ——, "Observation of a Charged Charmoniumlike Structure in $e^+e^- \to (D*\bar{D}*)^{\pm}\pi^{\mp}$ at $\sqrt{s} = 4.26$ GeV," *Physical Review Letters*, vol. 112, no. 13, Apr. 2014. https://link.aps.org/doi/10.1103/PhysRevLett.112.132001

[6] ——, "Observation of a Charged $(D*\bar{D}*)^{\pm}$ Mass Peak in $e^+e^- \to \pi D\bar{D}$ at $\sqrt{s} = 4.26$ GeV," *Physical Review Letters*, vol. 112, no. 2, Jan. 2014. https://link.aps.org/doi/10.1103/PhysRevLett.112.022001

[7] Wikimedia Commons, "Standard Model of Elementary Particles," Sep. 2019. https://commons.wikimedia.org/w/index.php?title=File:Standard_Model_of_Elementary_Particles.svg&oldid=369294672

[8] ——, "Elementary particle interactions in the Standard Model," May 2014. https://commons.wikimedia.org/wiki/File:Elementary_particle_interactions_in_the_Standard_Model.png

[9] H. Yukawa, "On the interaction of elementary particles. I," *Nippon Sugaku-Buturigakkwai Kizi Dai 3 Ki*, vol. 17, pp. 48–57, 1935.

[10] G. D. Rochester and C. C. Butler, "Evidence for the Existence of New Unstable Elementary Particles," *Nature*, vol. 160, no. 4077, pp. 855–857, Dec. 1947. http://www.nature.com/articles/160855a0

[11] M. Tanabashi *et al.*, "Review of Particle Physics," *Physical Review D*, vol. 98, no. 3, Aug. 2018. https://link.aps.org/doi/10.1103/PhysRevD.98.030001

[12] S. Capstick *et al.*, "Key Issues in Hadronic Physics," *arXiv:hep-ph/0012238*, Dec. 2000. http://arxiv.org/abs/hep-ph/0012238

[13] J. J. Aubert *et al.*, "Experimental Observation of a Heavy Particle J," *Physical Review Letters*, vol. 33, no. 23, pp. 1404–1406, Dec. 1974. https://link.aps.org/doi/10.1103/PhysRevLett.33.1404

[14] J. E. Augustin *et al.*, "Discovery of a Narrow Resonance in e^+e^- Annihilation," *Physical Review Letters*, vol. 33, no. 23, pp. 1406–1408, Dec. 1974. https://link.aps.org/doi/10.1103/PhysRevLett.33.1406

[15] R. A. Briere *et al.*, "Physics Accomplishments and Future Prospects of the BES Experiments at the BEPC Collider," *Annual Review of Nuclear and Particle Science*, vol. 66, no. 1, pp. 143–170, Oct. 2016. http://arxiv.org/abs/1603.09431

[16] M. Tanabashi *et al.*, "91. Charmonium System," in *Review of Particle Physics: Volume II Particle Listings*, ser. Physical Review, 2012, vol. 98, no. D, pp. 1250–1281. http://pdg.lbl.gov/2019/reviews/rpp2018-rev-charmonium.pdf

[17] IHEP, "History of the Institute of High Energy Physics," 2016. http://english.ihep.cas.cn/doc/216.html

[18] M. Ye and Z. Zheng, "BEPC, The Beijing Electron–Positron Collider," *International Journal of Modern Physics A*, vol. 02, no. 06, pp. 1707–1725, Dec. 1987. https://www.worldscientific.com/doi/abs/10.1142/S0217751X87000880

[19] W. K. H. Panofsky and J. M. Deken, *Panofsky on Physics, Politics, and Peace: Pief Remembers*. New York: Springer, 2007.

[20] K. Tuttle, "Chasing charm in China," *Symmetry Magazine*, Jan. 2009. https://www.symmetrymagazine.org/article/may-2009/chasing-charm-in-china

[21] W. Gradl, "BESIII future plans," Torino, Italy, May 2019. https://agenda.infn.it/event/15632/contributions/89351/

[22] IHEP, "Facilities of the Institute of High Energy Physics," 2016. http://english.ihep.cas.cn/chnl/18/index.html

[23] T. C. S. Group, "CEPC Conceptual Design Report: Volume 1 — Accelerator," *arXiv:1809.00285 [hep-ex, physics:physics]*, Sep. 2018. http://arxiv.org/abs/1809.00285

[24] ——, "CEPC Conceptual Design Report: Volume 2 — Physics & Detector," *arXiv:1811.10545 [hep-ex, physics:hep-ph]*, Nov. 2018. http://arxiv.org/abs/1811.10545

[25] CERN Courier, "China's bid for a circular electron–positron collider," *CERN Courier*, Jun. 2018. https://cerncourier.com/chinas-bid-for-a-circular-electron-positron-collider/

[26] M. Ablikim *et al.*, "Design and construction of the BESIII detector," *Nuclear Instruments and Methods in Physics Research Section A: Accelerators, Spectrometers, Detectors and Associated Equipment*, vol. 614, no. 3, pp. 345–399, Mar. 2010. https://linkinghub.elsevier.com/retrieve/pii/S0168900209023870

[27] M. Davier and A. Höcker, "Improved determination of $\alpha(MZ^2)$ and the anomalous magnetic moment of the muon," *Physics Letters B*, vol. 419, no. 1-4, pp. 419–431, Feb. 1998. https://linkinghub.elsevier.com/retrieve/pii/S0370269397015128

[28] J. Bai *et al.*, "The BES detector," *Nuclear Instruments and Methods in Physics Research Section A: Accelerators, Spectrometers, Detectors and Associated Equipment*, vol. 344, no. 2, pp. 319–334, May 1994. https://linkinghub.elsevier.com/retrieve/pii/0168900294900817

[29] ——, "The BES upgrade," *Nuclear Instruments and Methods in Physics Research Section A: Accelerators, Spectrometers, Detectors and Associated Equipment*, vol. 458, no. 3, pp. 627–637, Feb. 2001. https://linkinghub.elsevier.com/retrieve/pii/S0168900200009347

[30] D. Peterson, "Construction of the CLEOIII tracking system: Silicon vertex detector and drift chamber," *Nuclear Instruments and Methods in Physics Research Section A: Accelerators, Spectrometers, Detectors and Associated Equipment*, vol. 409, no. 1-3, pp. 204–209, May 1998. https://linkinghub.elsevier.com/retrieve/pii/S0168900298000783

[31] L. Lavezzi *et al.*, "The Cylindrical GEM Inner Tracker of the BESIII experiment: Prototype test beam results," *Journal of Instrumentation*, vol. 12, no. 07, pp. C07 038–C07 038, Jul. 2017. http://stacks.iop.org/1748-0221/12/i=07/a=C07038?key=crossref.8bc0a76c77daaa031eb0be7671006aff

[32] S. Marcello *et al.*, "A new inner tracker based on GEM detectors for the BES III experiment," *International Journal of Modern Physics: Conference Series*, vol. 48, p. 1860119, Jan. 2018. https://www.worldscientific.com/doi/abs/10.1142/S2010194518601199

[33] E. Abakumova *et al.*, "The Beam Energy Measurement System for the Beijing Electron–Positron Collider," *Nuclear Instruments and Methods in Physics Research Section A: Accelerators, Spectrometers, Detectors and Associated Equipment*, vol. 659, no. 1, pp. 21–29, Dec. 2011. https://linkinghub.elsevier.com/retrieve/pii/S0168900211017104

[34] N. Brambilla *et al.*, "Heavy quarkonium: Progress, puzzles, and opportunities," *The European Physical Journal C*, vol. 71, no. 2, Feb. 2011. http://link.springer.com/10.1140/epjc/s10052-010-1534-9

[35] J. Z. Bai *et al.*, "Measurement of the Branching Fraction of $J/\psi \to \pi^+\pi^-\pi^0$," *Physical Review D*, vol. 70, no. 1, Jul. 2004. https://link.aps.org/doi/10.1103/PhysRevD.70.012005

[36] M. Ablikim *et al.*, "Partial wave analysis of $\psi' \to \pi^+\pi^-\pi^0$ at BESII," *Physics Letters B*, vol. 619, no. 3-4, pp. 247–254, Jul. 2005. https://linkinghub.elsevier.com/retrieve/pii/S0370269305006775

[37] A. J. Bevan *et al.*, "The Physics of the B Factories," *The European Physical Journal C*, vol. 74, no. 11, Nov. 2014. http://link.springer.com/10.1140/epjc/s10052-014-3026-9

[38] M. Ablikim *et al.*, "Measurement of y_{CP} in D^0–$\bar{D}^0$ oscillation using quantum correlations in $e^+e^- \to D^0\bar{D}^0$ at $\sqrt{s} = 3.773$ GeV," *Physics Letters B*, vol. 744, pp. 339–346, May 2015. http://linkinghub.elsevier.com/retrieve/pii/S0370269315002518

[39] D. M. Asner *et al.*, "Physics at BES-III," *Int. J. Mod. Phys.*, vol. A24, pp. S1–794, 2009.

[40] X.-R. Lü and H.-B. Li, "White paper on the BESIII experiment [to be published]," Jul. 2019. https://docbes3.ihep.ac.cn/cgi-bin/DocDB/ShowDocument?docid=759

[41] J. Hu and BESIII Collaboration, "Light Hadron Spectroscopy at BESIII," *Journal of Physics: Conference Series*, vol. 599, p. 012003, Apr. 2015. http://stacks.iop.org/1742-6596/599/i=1/a=012003?key=crossref.54e90e314a7b10d79bc7c0d52961c96f

[42] V. Crede and C. Meyer, "The experimental status of glueballs," *Progress in Particle and Nuclear Physics*, vol. 63, no. 1, pp. 74–116, Jul. 2009. https://linkinghub.elsevier.com/retrieve/pii/S0146641009000052

[43] M. Ablikim *et al.*, "Polarization and Entanglement in Baryon-Antibaryon Pair Production in Electron–Positron Annihilation," *arXiv:1808.08917 [hep-ex, physics:nucl-ex]*, Aug. 2018. http://arxiv.org/abs/1808.08917

[44] W.-D. Li *et al.*, "Chapter 2: The BES-III Detector and Offline Software," *International Journal of Modern Physics A*, vol. 24, no. supp01, pp. 9–21, May 2009. https://www.worldscientific.com/doi/abs/10.1142/S0217751X09046424

[45] W. Li *et al.*, "The Offline Software for the BESIII Experiment," in *The BESIII Offline Software*, Mumbai, India, Feb. 2006. https://indico.cern.ch/event/408139/contributions/979815/

[46] Z. Deng, "Status of Offline Software [internal document]," Wuhan University, Wuhan, Hubei, Nov. 2018. https://indico.ihep.ac.cn/event/8569/session/1/contribution/90

[47] M. A. Sanchis-Lozano, "On the search for weak decays of heavy quarkonium in dedicated heavy-quark factories," *Zeitschrift für Physik C Particles and Fields*, vol. 62, no. 2, pp. 271–279, Jun. 1994. http://link.springer.com/10.1007/BF01560243

[48] A. Datta *et al.*, "Flavor changing processes in quarkonium decays," *Physical Review D*, vol. 60, no. 1, Jun. 1999. https://link.aps.org/doi/10.1103/PhysRevD.60.014011

[49] X. Zhang, "Probing for New Physics in J/ψ Decays," *High Energy Physics and Nuclear Physics*, vol. 25, no. 5, pp. 461–464, May 2001. http://caod.oriprobe.com/articles/3821750/Probing_for_New_Physics_in_J_%CF%88_Decays.htm

[50] C. T. Hill, "Topcolor assisted technicolor," *Physics Letters B*, vol. 345, no. 4, pp. 483–489, Feb. 1995. https://linkinghub.elsevier.com/retrieve/pii/0370269394016605

[51] D. Kominis, "Flavor-changing neutral current constraints in topcolor-assisted technicolor," *Physics Letters B*, vol. 358, no. 3, pp. 312–317, Sep. 1995. http://www.sciencedirect.com/science/article/pii/037026939501047T

[52] C. S. Aulakh and R. N. Mohapatra, "The neutrino as the supersymmetric partner of the majoron," *Physics Letters B*, vol. 119, no. 1, pp. 136–140, Dec. 1982. http://www.sciencedirect.com/science/article/pii/0370269382902623

[53] S. L. Glashow and S. Weinberg, "Natural conservation laws for neutral currents," *Physical Review D*, vol. 15, no. 7, pp. 1958–1965, Apr. 1977. https://link.aps.org/doi/10.1103/PhysRevD.15.1958

[54] J. Sun *et al.*, "$J/\psi \to DP, DV$ decays in the QCD Factorization Approach," *International Journal of Modern Physics A*, vol. 30, no. 16, p. 1550094, Jun. 2015. https://www.worldscientific.com/doi/abs/10.1142/S0217751X15500943

[55] R. C. Verma *et al.*, "Hadronic weak decays of ψ," *Physics Letters B*, vol. 252, no. 4, pp. 690–694, Dec. 1990. http://www.sciencedirect.com/science/article/pii/0370269390905073

[56] R. Aaij *et al.*, "Observation of CP Violation in Charm Decays," *Physical Review Letters*, vol. 122, no. 21, May 2019. https://link.aps.org/doi/10.1103/PhysRevLett.122.211803

[57] ——, "Evidence for CP Violation in Time-Integrated $D^0 \to h^+h^-$ + Decay Rates," *Physical Review Letters*, vol. 108, no. 11, Mar. 2012. https://link.aps.org/doi/10.1103/PhysRevLett.108.111602

[58] H.-B. Li and S.-H. Zhu, "Mini-review of rare charmonium decays at BESIII," *Chinese Physics C*, vol. 36, no. 10, p. 932, 2012. http://stacks.iop.org/1674-1137/36/i=10/a=003

[59] M. Ablikim *et al.*, "Search for the rare decays $J/\psi \to D_s^-\pi^+$, $J/\psi \to D^-\pi^+$, and $J/\psi \to D^0K^0$," *Physics Letters B*, vol. 663, no. 4, pp. 297–301, May 2008. https://linkinghub.elsevier.com/retrieve/pii/S0370269308004681

[60] Y.-M. Wang *et al.*, "Weak decays of J/ψ: The non-leptonic case," *The European Physical Journal C*, vol. 55, no. 4, pp. 607–613, Jun. 2008. http://www.springerlink.com/index/10.1140/epjc/s10052-008-0619-1

[61] Y.-L. Shen and Y.-M. Wang, "J/ψ weak decays in the covariant light-front quark model," *Physical Review D*, vol. 78, no. 7, p. 074012, Oct. 2008. https://link.aps.org/doi/10.1103/PhysRevD.78.074012

[62] R. Dhir *et al.*, "Effects of Flavor Dependence on Weak Decays of J/ψ and Υ," *Advances in High Energy Physics*, vol. 2013, pp. 1–12, 2013. http://www.hindawi.com/journals/ahep/2013/706543/

[63] K. K. Sharma and R. C. Verma, "Rare decays of ψ and Υ," *International Journal of Modern Physics A*, vol. 14, no. 06, pp. 937–945, Mar. 1999. http://www.worldscientific.com/doi/abs/10.1142/S0217751X99000464

[64] M. Ablikim *et al.*, "Search for the rare decays $J/\psi \to D_s^-\pi^+$ and $J/\psi \to D^0K^0$*," *Physical Review D*, vol. 89, no. 7, p. 071101, Apr. 2014. https://link.aps.org/doi/10.1103/PhysRevD.89.071101

[65] C. Wang *et al.*, "Search for J/ψ weak decays," Jun. 2019. https://docbes3.ihep.ac.cn/cgi-bin/DocDB/ShowDocument?docid=802

[66] M. Ablikim *et al.*, "Search for the rare decays $J/\psi \to D_s^-e^+\nu_e$, $J/\psi \to D^-e^+\nu_e$, and $J/\psi \to D^0e^+e^-$," *Physics Letters B*, vol. 639, no. 5, pp. 418–423, Aug. 2006. http://www.sciencedirect.com/science/article/pii/S0370269306007751

[67] ——, "Search for the weak decays $J/\psi \to D_s^{-(*)}e^+\nu_e$ + c.c.," *Physical Review D*, vol. 90, no. 11, p. 112014, Dec. 2014. https://link.aps.org/doi/10.1103/PhysRevD.90.112014

[68] BESIII Offline Software Group, "Software Guide – Analysis, Vertex Fit," Apr. 2014. https://docbes3.ihep.ac.cn/~offlinesoftware/index.php/Vertex_Fit

[69] A. Gilman, "K/π PID Performance using BOSS v7.0.3 in Open Charm Events at 4.178 GeV," Jun. 2018. https://docbes3.ihep.ac.cn/cgi-bin/DocDB/ShowDocument?docid=729

[70] M. Ablikim *et al.*, "Determination of the number of J/ψ events with inclusive J/ψ decays," *Chinese Physics C*, vol. 41, no. 1, p. 013001, Jan. 2017. https://doi.org/10.1088%2F1674-1137%2F41%2F1%2F013001

[71] G. Xu *et al.*, "Trigger Efficiencies for 2018 J/ψ data & Total J/ψ events collected at BESIII," Changsha, China, Mar. 2019. https://indico.ihep.ac.cn/event/8795/session/3/contribution/9

[72] S. Agostinelli *et al.*, "Geant4—a simulation toolkit," *Nuclear Instruments and Methods in Physics Research Section A: Accelerators, Spectrometers, Detectors and Associated Equipment*, vol. 506, no. 3, pp. 250–303, Jul. 2003. https://linkinghub.elsevier.com/retrieve/pii/S0168900203013688

[73] J. Allison *et al.*, "Geant4 developments and applications," *IEEE Transactions on Nuclear Science*, vol. 53, no. 1, pp. 270–278, Feb. 2006. http://ieeexplore.ieee.org/document/1610988/

[74] ——, "Recent developments in Geant4," *Nuclear Instruments and Methods in Physics Research Section A: Accelerators, Spectrometers, Detectors and Associated Equipment*, vol. 835, pp. 186–225, Nov. 2016. https://linkinghub.elsevier.com/retrieve/pii/S0168900216306957

[75] D. J. Lange, "The `EvtGen` particle decay simulation package," *Nuclear Instruments and Methods in Physics Research Section A: Accelerators, Spectrometers, Detectors and Associated Equipment*, vol. 462, no. 1-2, pp. 152–155, Apr. 2001. https://linkinghub.elsevier.com/retrieve/pii/S0168900201000894

[76] R.-G. Ping, "Event generators at BESIII," *Chinese Physics C*, vol. 32, no. 8, pp. 599–602, Aug. 2008. https://iopscience.iop.org/article/10.1088/1674-1137/32/8/001

[77] R.-G. Ping and C.-Y. Pang, "Monte Carlo Generators for Tau-Charm-Physics at BESIII," Dec. 2006.

[78] M. Tanabashi *et al.*, "48. Resonances," in *Review of Particle Physics: Volume II Particle Listings*, ser. Physical Review, Aug. 2018, vol. 98, no. D, pp. 1250–1281. http://pdg.lbl.gov/2019/reviews/rpp2018-rev-resonances.pdf

[79] M. Ablikim *et al.*, "Observation of pseudoscalar and tensor resonances in $J/\psi \to \gamma\phi\phi$," *Physical Review D*, vol. 93, no. 11, p. 112011, Jun. 2016. https://link.aps.org/doi/10.1103/PhysRevD.93.112011

[80] T. J. Rivlin, *The Chebyshev Polynomials*, ser. Pure and Applied Mathematics. New York: Wiley, 1974.

[81] W. Verkerke and D. Kirkby, *RooFit Users Manual Version 2.91-33*, Oct. 2008, vol. v2.91.

[82] R. Barlow, "Systematic Errors: Facts and fictions," *arXiv:hep-ex/0207026*, Jul. 2002. http://arxiv.org/abs/hep-ex/0207026

[83] K. Schoening and P. Adlarson, "Checklist for evaluation of systematic uncertainties [internal memo]," Jun. 2019. https://docbes3.ihep.ac.cn/cgi-bin/DocDB/ShowDocument?docid=807

[84] M. Ablikim *et al.*, "Study of χ_{cJ} radiative decays into a vector meson," *Physical Review D*, vol. 83, no. 11, Jun. 2011. https://link.aps.org/doi/10.1103/PhysRevD.83.112005

[85] ——, "Branching fraction measurements of χ_{c0} and χ_{c2} to $\pi^0\pi^0$ and $\eta\eta$," *Physical Review D*, vol. 81, no. 5, p. 052005, Mar. 2010. https://link.aps.org/doi/10.1103/PhysRevD.81.052005

[86] E. Gross, "LHC statistics for pedestrians," in *PHYSTAT-LHC Workshop on Statistical Issues for LHC Physics*. CERN, 2008. https://inspirehep.net/record/776351/

[87] A. L. Read, "Presentation of search results: The CL_s technique," *Journal of Physics G: Nuclear and Particle Physics*, vol. 28, no. 10, pp. 2693–2704, Oct. 2002. http://stacks.iop.org/0954-3899/28/i=10/a=313?key=crossref.e0956de886e3eaacac3a701fa4c097b8

[88] R. de Boer *et al.*, "A roadmap for better documentation and code collaboration in BESIII [internal document]," Jul. 2019. https://docbes3.ihep.ac.cn/cgi-bin/DocDB/ShowDocument?docid=808

[89] K. Cranmer and I. Yavin, "RECAST: Extending the Impact of Existing Analyses," *Journal of High Energy Physics*, vol. 2011, no. 4, Apr. 2011. http://arxiv.org/abs/1010.2506

[90] V. Stodden and S. Miguez, "Best Practices for Computational Science: Software Infrastructure and Environments for Reproducible and Extensible Research," *Journal of Open Research Software*, vol. 2, no. 1, Jul. 2014. http://openresearchsoftware.metajnl.com/article/view/jors.ay/

[91] M. Baker, "1,500 scientists lift the lid on reproducibility," *Nature*, vol. 533, no. 7604, pp. 452–454, May 2016. http://www.nature.com/doifinder/10.1038/533452a

[92] S. Neubert *et al.*, "LHCb Analysis Preservation Roadmap," 2017. https://www.authorea.com/users/42472/articles/140021-lhcb-analysis-preservation-roadmap/_show_article

[93] S. Dallmeier-Tiessen and T. Šimko, "Open science: A vision for collaborative, reproducible and reusable research," *CERN Courier*, Mar. 2019. https://cerncourier.com/open-science-a-vision-for-collaborative-reproducible-and-reusable-research/

[94] X. Chen *et al.*, "Open is not enough," *Nature Physics*, vol. 15, no. 2, pp. 113–119, Nov. 2018. http://www.nature.com/articles/s41567-018-0342-2

[95] J. Albrecht *et al.*, "A Roadmap for HEP Software and Computing R&D for the 2020s," *Computing and Software for Big Science*, vol. 3, no. 1, p. 7, Mar. 2019. https://doi.org/10.1007/s41781-018-0018-8